15:14:07 OCA PAD AMENDMENT - PROJECT HEADER INFORMATION 07/15/93

Active

Project #: G-35-503 Cost share #: Rev #: 4
Center # : 10/11-6-P5090-0A0 Center shr #: OCA file #:
Work type : INST
Contract#: NGT-50765 Mod #: SUPPL. 2 Document : GRANT
Prime #: Contract entity: GTRC

Subprojects ? : N CFDA: 43.002
Main project #: PE #: N/A

Project unit: E & A SCI Unit code: 02.010.140
Project director(s):
CHAMEIDES W L E & A SCI (404)894-3883

Sponsor/division names: NASA / HEADQUARTERS/WASHINGTON, DC
Sponsor/division codes: 105 / 002

Award period: 910701 to 940630 (performance) 940630 (reports)

Sponsor amount	New this change	Total to date
Contract value	(1,048.00)	60,448.00
Funded	20,952.00	60,448.00
Cost sharing amount		0.00

Does subcontracting plan apply ?: N

Title: MODELING THE TEMPORAL & SPATIAL VARIATIONS OF TITAN'S STRATOSPHERIC HAZE

PROJECT ADMINISTRATION DATA

OCA contact: Anita D. Rowland 894-4820

Sponsor technical contact

J LYNCH, GSRP MANAGER, CODE FEH
(202)358-1531

NASA HEADQUARTERS
OFFICE OF EXTERNAL RELATIONS
EDUCATIONAL AFFAIRS DIVISIONS
UNIVERSITY PROGRAMS BRANCH
WASHINGTON, DC 20546

Sponsor issuing office

ADRIENE WOODIN, CODE HWB-2
(202)708-8970

NASA HEADQUARTERS
HEADQUARTERS ACQUISITION DIVISION
WASHINGTON, DC 20546

Security class (U,C,S,TS) : U ONR resident rep. is ACO (Y/N): N
Defense priority rating : N/A N/A supplemental sheet
Equipment title vests with: Sponsor GIT
"USE OF T/GRANT FUNDS FOR PURCHASE OF EQUIPMENT WILL NOT BE PERMITTED."
Administrative comments -
PROCESSED SUPPLEMENT 2 WHICH PROVIDES FUNDING FOR THIRD YEAR OF GRANT.
REPRESENTS A REDUCTION IN YEAR 3 (-$1048).

GEORGIA INSTITUTE OF TECHNOLOGY
OFFICE OF CONTRACT ADMINISTRATION

NOTICE OF PROJECT CLOSEOUT

Closeout Notice Date 09/27/94

Project No. G-35-503 Center No. 10/11-6-P5090-0A0

Project Director CHAMEIDES W L School/Lab E & A SCI

Sponsor NASA/HEADQUARTERS/WASHINGTON, DC

Contract/Grant No. NGT-50765 Contract Entity GTRC

Prime Contract No. _____

Title MODELING THE TEMPORAL & SPATIAL VARIATIONS OF TITAN'S STRATOSPHERIC HAZE

Effective Completion Date 940630 (Performance) 940630 (Reports)

Closeout Actions Required:	Y/N	Date Submitted
Final Invoice or Copy of Final Invoice	N	
Final Report of Inventions and/or Subcontracts	Y	
Government Property Inventory & Related Certificate	N	
Classified Material Certificate	N	
Release and Assignment	N	
Other _____	N	

Comments
LETTER OF CREDIT APPLIES.

Subproject Under Main Project No. _____

Continues Project No. _____

Distribution Required:

Project Director	Y
Administrative Network Representative	Y
GTRI Accounting/Grants and Contracts	Y
Procurement/Supply Services	Y
Research Property Managment	Y
Research Security Services	N
Reports Coordinator (OCA)	Y
GTRC	Y
Project File	Y
Other _____	N
_____	N

NOTE: Final Patent Questionnaire sent to PDPI.

FINAL REPORT

Contract # NGT-50765

As Prepared By:

William L. Chameides
School of Earth and Atmospheric Sciences
Georgia Institute of Technology
Atlanta, GA 30332-0340

MODELING THE TEMPORAL & SPATIAL VARIATIONS OF TITAN'S STRATOSPHERIC HAZE

Under a grant from the NASA Graduate Researcher's Program, William T. Hutzell conducted the research for his Ph.D. thesis. His thesis explored causes for the temporal variations in the geometric albedo and atmospheric brightness of Titan. The observed variations are postulated to be caused by inducting variations in the haze layer in Titan's stratosphere. The production of the haze layer, and the stratospheric circulation were tested to explain the observations by simulating their effects on the haze layer with aerosol models. The circulation was identified to be the more likely source of the observed variations.

To facilitate the conduct of Mr. Hutzell's research, he re-located to California and worked at the NASA Ames Research Center under the day-to-day direction NASA scientists, Drs. Chris McKay and Owen B. Toon. Mr. Hutzell completed his research and defended his thesis in May of 1994. Mr. Hutzell was awarded the Ph.D. at the 1994 Summer Commecement of the Georgia Instiute of Technology.

Thus far, Mr. Hutzell's result has resulted in one publication:

> Hutzell, W.T., C.P. McKay, and O.B. Toon, Effects of time-varying haze production on Titan's geometric albedo, *Icarus*, **105**, 162-174, 1993.

A reprint of the paper and copy of Mr. Hutzell's thesis are included as Appendices to this final report.

Vita

William T. Hutzell was born in Cheberly, Maryland on July 6, 1964. He recieve a Bachelor's of Science in Astronomy and Physics from the Univarsity of Maryland. In 1989, he completed a Master's Degree in Physic from the University of Wyoming. His master's thesis was on time scales of Titan's atmosphere. Up to the time of his Ph. D. thesis, his research interests were mainly on planetary atmospheres.

The Variations in the Geometric Albedo of Titan

A THESIS Presented to

The Academic Faculty

by

William T. Hutzell

In Partial Fulfillment

of The Requirements for the Degree

Doctor of Philosophy in Earth and Atmospheric Sciences

Georgia Institute of Technology

June 14, 1994

Contents

List of Figures

List of Tables

Table of Symbols

Table of Symbols

Chapter 1	
g	Gravitational Acceleration
H	Scale Height of Pressure
R_T	Radius of Titan
P	Pressure
T	Temperature
T_B	Brightness Temperature
T_e	Radiative Equilibrium Temperature
u	Zonal Wind Speed
v	Meridional Wind Speed
z	Altitude
φ	Latitude
Γ	Lapse Rate
λ	Wavelength
Ω_R	Angular Frequency of Rotation
τ_r	Radiative Time Constant
τ_d	Dynamical Time Constant

Chapter 2	
$P(t)$	Geometric Albedo at t
P_l	Average of the Geometric Albedo
a_l	Amplitude of the Variation in the Geometric Albedo
ω_p	Angualar Frequency of the Variation in the Geometric Albedo
$n(v)$	Particle Number Density at v
t	Time
v	Volume
v_s	Particle Sedimnetation Velocity
$K(\nu, v)$	Brown Coagulation Coefficient
$q(v)$	Particle Production Rate at v
R_r	Rainout Rate
$m(z)$	Column Density of Haze Material at z
$\rho_h(z)$	Mass Holding of Haze Material at z
z	Altitude
γ	Ratio between Maximum and Minimum Rates of Haze Production
τ	Optical Depth at 0.55 μm

Chapter 3	
B	Static Stability Parameter of Atmosphere
c_p	Specific Heat at Constant Pressure
f	Coriolis Parameter
g	Gravitational Acceleration
H	Scale Height of Pressure
K_H	Horizontal Eddy Diffusion Coefficient
L	Length of Circulation Cell
T	Temperature
T_s	Temperature in the Stratosphere
T_e	Radiative Equilibrium Temperature
P	Pressure
P_s	Pressure in the Stratosphere
Q	Fractional Rate of Change of Temperature
$\dot{q}$	Heating Rate Per Unit Mass
R	Ideal Gas Constant
r	Reciprocal of the Time Constant for Frictional Dissipation
S_o	Solar Flux onto Titan
t	Time
u	Zonal Wind Speed
v	Meridional Wind Speed
W	Height of Circulation Cell
w	Vertical Wind Speed
y	Distance from Northern Pole
z	Altitude
α	Reciprocal of The Radiative Time Constant
γ	Ratio of Specific Heats
η	Average of Q over Space
μ	Gram Molecular Weight
ω_s	Angular Frequency of Seasonal Cycle
φ	Initial Phase of the Seasonal Variation in the Wind Field
ψ	Streamfunction of Wind Field
ρ	Atmospheric Density
θ	Potential Temperature
ξ	$\frac{r}{\alpha(r^2+f^2)}$

Chapter 4	
$n(v)$	Number Density of Haze Particles at v
v	Volume
t	Time
v_y	Speed of Meridional Wind
w	Speed of Vertical Wind
v_s	Sedimentation Speed of a Haze Particle
K_z	Vertical Eddy Diffusion Coefficient
K_y	Meridional Eddy Diffusion Coefficient
n_a	Number Density of the Atmosphere
K	Brownian Coagulation Coefficient
$q(v)$	Production Rate of Haze Particles at v
R_r	Rainout Rate
P_λ	Monchromatic Geometric Albedo
F_λ	Monochromatic Solar Flux
B_λ	Monochromatic Atmospheric Brightness
R_λ	Monochromatic Relative Normal Albedo
F_λ°	Monochromatic Flux from Titan
F_λ^L	Monochromatic Flux from a Lambert Surface
R	Radius of Titan
Δ	Distance between Earth and Titan
μ	Cosine of the Solar Zenith Angle or the Observer's Angle
ϕ	Azimuthal Angle of the Observer
I_λ	Monochromatic Irradiance
φ'	Latitude
v_y^{max}	Maximum of Meridional Wind at $\sim$ 110 km
R_{sfc}	Surface Albedo
g	Column Forward Scattering Coefficient
ϖ	Column Single Scattering Albedo
τ	Optical Depth

Summary

Titan is a satellite of Saturn and its geometric albedo has been observed to vary at 0.47 μm and 0.55μm over the past two decades (Lockwood 1977 and Lockwood *et al.* 1986). These observations are explained by variations in atmospheric reflectance over time and latitude (Sromovsky *et al.* 1981 and Caldwell *et al.* 1992). In the visible spectrum, the atmospheric reflectance is determined by a haze layer in the stratosphere of Titan, because this haze layer has a global extent and is optically thick in the visible spectrum (Pollack *et al.* 1980). Therefore, variations in the haze layer are believed to cause the observed variations in the geometric albedo, but the source for the haze variations are unknown.

Two controls on the haze layer are examined for the source of the observed variations in the geometric albedo of Titan. Each examination consists of two parts: time simulations of the haze layer, and comparisons between the predicted reflectances and the the observations. The first part simulates the haze layer by using an aerosol model. The comparison test is accomplished by radiative transfer calculations of the results from the haze simulations (Toon *et al.* 1989). Production of the haze layer is the first control on the haze layer which is examined in our study. Its examination is conducted with an aerosol model which has been previously applied to Titan (Toon *et al.* 1992). The

circulation of the atmosphere is the second control which may produce the variations in the haze layer. This control from the circulation is examined with an aerosol model which is two dimensional, because the existing model is inadequate. A wind field is derived for the two dimensional model and is used to represent the atmospheric circulation which induces variations in the simulations of the haze layer.

Both controls on the haze layer were able to produce some of the observations of the geometric albedo and atmospheric reflectance. The atmospheric circulation is concluded to be the better source for the observations for two reasons. The variations in the production rate produced only the size of the observed variations. The variations in the circulation matched the size and the temporal behavior in the observations. The control from the circulation was also considered the better source of the observed variations, because the observations were simulated without using model parameters which may be physically implausible. In the simulations for the production control, the size of the observed variations was produced only when particles of the haze were removed by the strong rainout in the stratosphere of Titan. This is not considered possible for the stratosphere of Titan (Toon *et al.* 1988b).

The conclusion on the source for the observations does have some reservations. Problems were indicated, because our simulations of the hemispheric brightness contrast (Sromovsky *et al.* 1981) were poor. The representation of the circulation is the most likely the cause of the failure. Our representation of the circulation was an extreme simplification of the actual circulation of Titan, because the wind field of the model was one cell for entire stratosphere, and did not include smaller scale winds. The derivation of the wind field also contained several assumptions which are incorrect for Titan. These assumptions included quasigeostropic balance, and the neglect of spherical effects

on circulation. The former assumption is incorrect for Titan, because the circulation of Titan is in the cyclostrophic approximation (Flasar *et al.* 1981, and Flasar and Conrath 1990). The latter assumption may be faulty, because the radius of Titan is relatively small ($\sim$ 0.4 of earth's radius), so spherical effects on the circulation can be very large for Titan (Hourdin *et al.* 1991).

Chapter 1

Introduction

Titan is the largest satellite of Saturn, but it is second largest in the solar system behind Gandeymede. The general statistics for Titan are given Table 1.1. The orbit of Titan about Saturn takes 16 days, and has an inclination of 27° with respect to the plane of the solar system. Titan is in a synchronously locked orbit, so the spin axis is also inclined to the ecliptic by 27° . One year for Titan, one cycle of the solar inclination at noon, is 29.5 years which is the Saturn's orbital period. The tilt of Titan's spin axis has consequences which are relevant to the topic of the observations of Titan.

The atmosphere is a distinguishing feature of Titan. The surface pressure is 1.5 bar so the atmosphere is substantial. N_2 accounts for more than 90% of atmospheric composition. The atmospheres of Titan and the earth are the only two atmospheres in the solar system with large amounts of N_2. Most of the remaining atmosphere is CH_4, but Ar may be present (Gautier 1985). Trace gasses include H_2, CO, nitriles, and other hydrocarbons. The atmospheric composition is highly reducing with respect to chemistry (Strobel 1985). This characteristic is similar to the atmosphere which has been

Table 1.1: Properties of Titan

Solid Body Radius, R_T	2575 km
Mass, M_T	1.35×10^{26} gm ($0.22M_{Earth}$)
Gravitational Acceleration at surface, g_s	135 cm sec^{-2}
Mean Density	1.88 gm cm^{-3} (5.3 gm cm^{-3} for Earth)
Distance from Saturn	1.23×10^{6} km
Orbital Period around Saturn	$\sim$ 16 day
Distance from Sun	9.55 AU
Tilt of Spin Axis to Ecliptic	$\sim 27°$
Duration of Seasonal Cycle	29.5 year
	($\equiv$ Orbital Period for Saturn)
Atmospheric Temperatures	
• Surface	94 K
• Tropopause (Altitude $\approx$ 42 km)	71.4 K
• Stratopuase (Altitude $\approx$ 200 km)	170 K
• Exobase (Altitude $\approx$ 1600 km)	186±20 K
Surface Pressure	1500±20 mbar
Mean Molecular Weight	28.8±1.0
Atmospheric Composition, Main Components	Molar Fraction
• Nitrogen, N_2	0.73-0.99
• Argon, Ar (uncertain)	0-0.28
• Methane, CH_4	0.01-0.12
• Hydrogen, H_2	2×10^{-3}
• Ethane, C_2H_6	2×10^{-5}

Adapted from Hunten (1985) and Gautier (1985)

postulated for the ancient earth. Atmospheric temperatures are much colder than the ancient earth and range from 70 to 170 K. Liquid water can not exist at such temperatures, so a biological analogy to the ancient earth is limited. Titan is still used for comparison studies of atmospheric dynamics, and chemistry with respect to the earth and other planets.

The photochemistry of Titan is started by the dissociations of N_2 and CH_4. N_2 molecules are broken by energetic electrons from the magnetosphere and by the EUV from the solar flux. CH_4 is directly or indirectly broken apart by solar radiation in the UV. Both dissociations lead to more complex compounds such as nitriles and other hydrocarbons. Some products from the atmospheric chemistry condense or sublime and produce an aerosol or haze layer (Yung *et al.* 1984). The haze particles are considered dry, so they are considered chemically inert. Haze particles do undergo microphysical processes. For example, particles grow by Brownian coagulation while sedimenting. Haze particles probably serve as condensation or ice nuclei for atmospheric gasses (Toon *et al.* 1988). Haze particles could also serve as catalytic surfaces for reactions between gasses of the atmosphere (Chassefiere *et al.* 1991). Haze particles are eventually removed from the atmosphere by sedimentation or by rainout (Hunten 1985).

The haze layer of Titan is easily observed. Haze production is global in extent, so it shrouds the satellite. The opacity of the haze layer is high in the visible and the UV, because of its absorption coefficients. Consequently, the surface of Titan has never been observed in the visible. In the IR, the surface may be seen (Griffith *et al.* 1992), because the extinction coefficient of the haze layer sharply decreases around 1 μm in wavelength (Khare *et al.* 1984). In the visible, the high amount of haze opacity implies that the distribution of the haze layer completely determines the brightness observations of Titan

in the visible.

The Titan's brightness at two visible wavelengths, 0.47 and 0.55 μm, has varied over the previous two decades (Figure 1.1). The observed variation is approximately 10% and 5% respectively for 0.47 and 0.55 μm (Lockwood 1977, Lockwood and Thompson 1979, Lockwood *et al.* 1986). These variations were not produced by the observational geometry, because the observations were normalized to a specific configuration of observational geometry. The geometric configuration is given in the definition of the geometric albedo (Dlugach and Yanovitskij 1974). Therefore, Titan, itself, has varied over the period of the observations. The haze layer is the best candidate for the observed variations, because of the wavelengths of the observations (Pollack *et al.* 1980). It was uncertain how the haze layer caused the observed variation in the geometric albedo until 1981.

In 1981, the Voyager probes provided an important clue to the source of the haze variations. Brightness or reflectivity was observed to vary over latitude. The wavelengths of the variation were similar to the wavelengths of geometric albedo observations. The brightness variation was approximately 20% over latitude and slightly varied over wavelength (Smith *et al.* 1981, Sromovsky *et al.* 1981). The variations of brightness were a little larger in the blue than in the red. The latitudinal distribution was the most important property of the brightness (Figure 1.2). The northern hemisphere was the darker than the southern hemisphere so a contrast in hemispheric brightness was observed during the Voyager fly-by. The hemispheric brightness contrast had a distinct boundary near the equator. Variations of brightness also were observed within a hemisphere and had a zonal structure (Sromovsky *et al.* 1981).

The structure of the hemispheric brightness contrast implies that the

source of the contrast was linked to the tilt of the spin axis. Therefore. the source of the hemispheric brightness contrast could be the variation of the solar forcing, which varies over latitude but also time (i. e. a seasonal variation). If the source of the contrast varies over time, the brightness contrast should vary over time (Figure 1.3). The seasonal variations in the brightness contrast can explain the observations of geometric albedo, if the brightness of a hemisphere lags one season (90° from 360° of phase) behind the seasonal solar forcing (Smith *et al.* 1981, and Sromovsky *et al.* 1981). Observations have confirmed the variation of brightness which were proposed (Lockwood 1986). Hence, it is known how the reflectivity varies over latitude and time, and how the variations of the visible geometric albedo are produced. It is uncertain what causes the variations of reflectivity. The haze layer is still the best candidate for producing the variation of the reflectivity because of the wavelengths for the hemispheric brightness contrast. The question is now what causes the haze layer to vary over season and latitude. The cause of the haze variations has to vary over season, because the variations of the haze must be periodic to account for the observations. The cause of haze variations must also produce haze distributions which produce the correct phase of the reflectivity variations. The induced variations of reflectivity ought to lag behind the solar forcing by 90° of phase (Sromovsky *et al.* 1981). Initial work has been done to identify the source of the haze variations (or the source for the variations of hemispheric brightness and for the variations in the geometric albedo), but the answer is still uncertain (Toon *et al.* 1992. and Flasar and Conrath 1990).

In this paper, we will examine two possible sources of haze variation which could produce the variations of the geometric albedo and hemispheric brightness. The first source is the seasonal variations in the production of the haze layer which is partially produced by the photochemistry. The potential

of this source will be evaluated by an aerosol model which has already been constructed and applied to Titan (Toon *et al.* 1980 and Toon *et al.* 1992). The second source of the haze variations is from atmospheric circulation, and is examined because the distribution of the haze layer is influenced by advection from atmospheric winds. The examination of the circulation source will be by a two dimensional model. Such models have not been constructed for Titan. The existing model of the haze layer (Toon *et al.* 1992) will be expanded from one to two dimensions (Toon *et al.* 1988). To drive the haze transport in the two dimensional model, a representation of the atmospheric circulation will have to be derived, and will be a simple representation. Both one and two dimensional models produce simulations over time, because the observations are explained by variations over season.

Our study is conducted in the following format. The remainder of this chapter builds a basis of information on Titan. The review of information covers temperature, composition, chemistry, dynamic, and haze structure. The second chapter determines the potential of haze production for the source of the observed variations (Hutzell *et al.* 1993). The next two chapters explore the potential of atmospheric dynamics. The first of these two chapters derives a wind field which represents the circulation in the two dimensional model. The following chapter determines the effects from this wind field. The final chapter is a summary and gives conclusion from the two investigations. Among the conclusions, recommendations are made for future modeling studies. The three chapters for the modeling studies are presented in a self contained format so each of these chapters could be a paper for publication.

THERMAL STRUCTURE

The Vertical Thermal Structure. The vertical distribution of the temperature was determined from the Voyager fly-by. The vertical thermal structure was obtained by a radio occultation experiment, and the soundings were obtained at two locations. The egress and ingress soundings were located near the equator, so the observations could represent an average of the vertical thermal structure (Conrath 1985). The occultation experiment actually measured the temperature divided by the mean molecular mass. Hence, a value of the mean molecular weight must assumed to determine the vertical thermal structure. The assumed value of the mean molecular weight introduces an uncertainty into the final result, because the trace gases in the atmosphere are not well defined (Conrath 1985).

If a pure nitrogen atmosphere is assumed, the vertical thermal structure of the atmosphere is given in Figure 1.4 for the egress and ingress soundings. The two profiles have small differences and imply zonal symmetry in the thermal structure, because the longitudes of the soundings were separated by 180° . Zonal symmetry in the thermal structure agrees with other observations from Voyagers. For example, the brightness had small variations in a band of constant latitude (Sromovsky *et al.* 1981). Small differences exist between the egress and ingress soundings and were small oscillations in high altitudes. These oscillations were possibly produced by atmospheric waves (Hunten 1985).

Two regions can be seen in the temperature profiles. These regions are similar to the earth. A troposphere exists and spans from 0 to 50 km in altitude. Temperatures of the troposphere are from 95 to 70 K. The lapse rate is determined by the pseudo-adiabatic conditions. These conditions are a combination of saturation and nonsaturation with respect to methane. because methane can condense at the temperatures in the troposphere. Liq-

uid methane may exist at the surface (Lunine *et al.* 1983), and would be a continuous source of atmospheric methane. In the upper troposphere, the decreases in temperature may produce methane condensation. Clouds of liquid methane may exist in the upper troposphere, but their existence is uncertain. The cold tropopause limits the methane transport into the stratosphere. This limiting effect on upward transport is commonly called the methane cold trap (Hunten 1985). Temperatures quickly increase above the troposphere to 170 K and then remains constant above 110 km in altitude. This region of the atmosphere is the stratosphere and spans from 50 to 300 km in altitude. The stratosphere is produced by the haze layer, because the material of the haze layer is postulated absorb solar radiation in the UV and visible. The particles of the haze layer reradiate the absorbed energy in the the IR and heat the stratosphere, because they are inefficient radiators in the UV and visible (Samuelson 1983).

The vertical distribution of temperature can be explained to a high degree of accuracy by radiative equilibrium. Two components comprise radiative equilibrium; the greenhouse effect and the antigreenhouse effect (McKay *et al.* 1991). The haze layer produces the antigreenhouse effect. The absorption in the haze layer heats the stratosphere and lowers the temperatures of the troposphere. Some radiation reaches the surface and heats the troposphere. The radiative comes in two forms: unattenuated radiation from the solar flux and thermal radiation from the haze particles. The troposphere is slightly warmer than expected, because thermal radiation is trapped by tropospheric gasses. The radiative cooling of the troposphere is then reduced. This is the greenhouse effect. The radiation trapping in the troposphere is from absorption which is collisionally induced. Trace gasses in the troposphere also produce band absorption in the thermal spectrum, but this source of absorption is only a small part of the greenhouse effect (McKay *et*

al. 1989).

Detailed models have studied the thermal structure at radiative equilibrium (Samuelson 1983 and McKay *et al.* 1989). The models determine a solution for the thermal structure which satisfies two constraints: convective stability, and the balance of radiative fluxes. Aspects of the vertical thermal structure are determined by these model and their solutions. The abundance of trace gasses can be estimated, because their abundances may be needed for balance of radiative fluxes. For example, the H_2 has a higher abundance than originally thought, because collision induced absorption from H_2 closes a window between 2.6 and 4.0 μm. Detailed models also yield information on the radiative controls which produce the thermal structure. For example, the surface temperature of Titan is limited, because a window is open at $\sim$ 15 μm. The open window cools the troposphere, if surface temperature rises above a critical value. For Titan, the models of radiative equilibrium fail to a small degree in the upper stratosphere. Two factors could produce the failure. A source of opacity is not accounted. Several hydrocarbons are possible candidates for the opacity. The radiative equilibrium model can also fail, because thermal advection was not in the detailed models. Atmospheric circulation may then significantly affect the temperatures in the upper atmosphere (McKay *et al.* 1989).

The Thermal Structure over Latitude. The meridional variations of temperature were determined by the infrared spectrometry experiment (IRIS) on the Voyager probes (Figure 1.5). A meridional cross-section of temperature was not thoroughly determined from the observations. The temperatures were taken at several points between -60° to 60° and at three levels in the atmosphere, because of the techniques for the data analysis. Later analysis determined the temperatures at higher latitudes. Later analysis also deter-

mined the temperatures at another level in the atmosphere. The brightness temperature, T_B, was actually measured by the IRIS experiment and was not exactly the temperature at a given point in the atmosphere. The value of T_B was the temperature of a black body which radiates at the same intensity as the observations. The source of the radiation was located near unity optical depth and was not a point source but was distributed over a scale height. The latitudinal variation of T_B was not along a constant altitude but along an isobar, because the radiation for T_B is from unity optical depth. The latitudinal variation of T_B was derived on assumption that the vertical structure of opacity was constant over latitude (Flasar *et al.* 1981).

The four wavenumbers were used for the observations; 530, 200, 1260-1290, and 1304 cm^{-1}. A different layer in the atmosphere is sampled by each wavenumber, because the atmosphere of Titan is not gray. At 530 cm^{-1}, the level is near the surface, because the atmosphere is semitransparent at this wavenumber. The surface temperatures were slightly higher in the equatorial region. The surface temperatures also appear to be asymmetric about the equator. The latitudinal variations of the surface temperature are uncertain especially the asymmetry about the equator, because the T_B at 530 cm^{-1} is not totally determined by radiation from the surface. Radiation from higher altitudes could have produced the asymmetry of T_B at 530 cm^{-1}. The stratosphere could be a source of this radiation, because its emissivities at 530 cm^{-1} are expected to vary over latitude. At 200 cm^{-1}, the temperatures were sampled near the tropopause. The tropopause was slightly warmer in the northern hemisphere. There is some uncertainty in this observation, because opacity at 200 cm^{-1} may not have been uniform over latitude. At 200 cm^{-1}, the opacity is from the haze layer and condensates. Both sources of opacity probably varied over latitude. In the wavenumber region of 1260-1290 cm^{-1}, the sampled level was at 1 mbar. This level in the atmosphere is where the

geometric albedo in the visible is determined. Consequently, the level has a special importance to our thesis. The opacity for these wavenumbers is from the P branch of methane. At 1304 cm^{-1}, the variation of T_B is given at 0.4 mbar level and was in the upper stratosphere. Opacity at 1304 cm^{-1} was from the Q branch of methane. At the 0.4 and 1 mbar levels, there was a 12 K variation from the equator to the poles. The northern hemisphere was colder than the southern hemisphere. There is strong confidence in the observations at the 1 and 0.4 mbar levels, because abundances of methane should be uniform over latitude (Flasar *et al.* 1991).

The radiative equilibrium can partially explain the observations of T_B. The solar radiation varies over time as well as latitude, so the radiative time constant, τ_r , is needed to explain the observation of T_B over altitude. At the surface, the τ_r is relatively easy to determine, because it depends on the bulk mass of the atmosphere. At higher levels, τ_r depends on the sources of emission. The emissitivities are fairly well constrainted in the upper stratosphere, so the τ_r can be determined for this region. The τ_r of the intermediate region are determined by extrapolation. This was how the vertical variation of the τ_r were first estimated after the Voyager fly-by (Figure 1.6) (Flasar *et al.* 1981). Since the initial evaluation, estimates of the τ_r have been performed by detailed models of radiative equilibrium (McKay *et al.* 1989). The values of τ_r are roughly consistent between the orginal and later estimations.

The vertical variation of τ_r yields some insight into the observations of T_B. We first must consider the effects from the variations in solar flux over latitude and time. To zeroth order, the solar flux depends on the cosine of latitude which implies an a temperature variation of 16 K between the equator and $\pm$ 60° . Two variations in the solar flux occur over time: the daily, and the seasonal. The daily variation in the solar flux should

produce an insignificant effect on T_B, because the values of τ_r are greater than one rotation at all the levels. Hence, seasonal variations of solar flux is the main concern in the temporal variation of temperature. At the surface, the value of τ_r is large with respect to one year for Titan, so the surface temperature should be symmetric about the equator. The observations are consistent this conclusion on the seasonal variations of surface temperatures, because it is uncertain whether tropospheric temperatures are asymmetric about the equator (Flasar *et al.* 1981). The surface temperature also had a smaller variation over latitude than predicted by radiative equilibrium. At the tropopause, the same variation of T_B were observed (Figure 1.5), so we make similar conclusions. At 0.4 mbar, variation of temperature should be larger over latitude, because the values of τ_r are much shorter than a season in the upper stratosphere. The latitudinal distribution of temperature did not agree with the predictions which are from the seasonal variation of solar flux. At 0.4 mbar, latitudinal variation of temperature should have been symmetric about the equator, because the solar flux was symmetric about the equator. The observed variation over latitude was also smaller than predicted by several degrees. The same conclusion are made for the 1 mbar, because the 1 and 0.4 mbar levels had a similar variation of temperature ovPer latitude, and because the value of τ_r is less than one season at 1 mbar (Flasar and Conrath 1990) Circulation could have produced these discrepancies with respect to radiative equilibrium.

DYNAMICS

The circulation in the troposphere is postulated from the latitudinal variation of T_B at 530 and 200 cm^{-1} which were smaller than expected from radiative equilibrium. A weak circulation is predicted, because the tropo-

sphere has a high thermal inertia, and because the gradient of surface temperature is postulated to be small over latitude. A further criteria for the tropospheric circulation is axial symmetry, because baroclinical waves should not occur in the troposphere (Leovy and Pollack 1973 and Golitsyn 1975). Hadley circulation can be used to describe the tropospheric circulation under these conditions, and a Hadley cell is predicted in each hemisphere (Flasar et 1991). The tropospheric circulation should not have large seasonal variations, because the τ_r of the troposphere is much larger than a season. The circulation of the stratosphere is more difficult to determine because the τ_r of the stratosphere are much smaller than the troposphere.

The zonal winds in the stratosphere are used to postulate the circulation of the stratosphere. The zonal wind are expected to be strong from the observations (Hunten 1985) because the temperature and the reflectivity were observed to be zonally symmetric (Flasar *et al.* 1981 and Sromovsky *et al.* 1981). High advection from zonal winds are used to explain the zonal symmetry in these observations. The size of the zonal winds can be estimated by the gradient wind equation.

$$2\Omega_R u \sin\phi + \frac{u^2 \tan\phi}{R_T} = \frac{-1}{\rho R_T}\frac{\partial P}{\partial \phi} \tag{1.1}$$

where Ω_R is the angular frequency for the rotation, ϕ is latitude, R_T is the radius of Titan, ρ is the atmospheric density, and P is the pressure. A simplification to the gradient wind equation is that the circulation of Titan is in the cyclostrophic approximation (i. e. The centripetal force, $\frac{u^2 \tan\phi}{R_T}$, must balance the meridional gradient of pressure, $\frac{-1}{\rho R_T}\frac{\partial P}{\partial \phi}$.), because the rotation rate of Titan is slow. The thermal wind equation can then be used of estimate the speed of the zonal winds,

$$\frac{\partial u^2 \tan\phi}{\partial z} \simeq g\frac{\partial \ln T}{\partial \phi}. \tag{1.2}$$

where g is the gravitational acceleration and T is the temperature. The zonal winds in the stratosphere are determined to be $\sim$ 75 cm sec^{-1}, so the atmosphere of Titan is super-rotating (i. e. $u \gg \Omega R_T$). Despite the super-rotation of the atmosphere, the zonal winds in the stratospheres should vary over season, because the average τ_r of the stratosphere is smaller than the length of a season, so the source of high zonal winds is forced to vary by the seasonal variation in the solar flux.

The meridional circulation of the stratosphere is postulated to be controled by the season variation of the zonal wind. The seasonal variation in the zonal winds can be estimated by the observations of T_B between the northern and southern hemisphere (Figure 1.5). In the stratosphere, the seasonal variation of the zonal wind is large enough to require a large change of angular momentum and can be accomplished by transferring momentum between the northern and southern hemispheres. This mechanism of momentum transport suggests that the meridional circulation of the stratosphere is from pole to pole. A pole to pole circulation is additionally favored, because it is axially symmetric. An axially symmetric circulation is theoretically implied in the stratosphere, because baroclinical waves can not exist in the stratosphere (Hunten 1985). The observations of T_B also imply that the stratospheric circulation is thermally indirect, because the northern region of the stratosphere was observed colder than in the southern region. This observation is not expected from radiative equilibrium, because Titan was near equinox during the observations. The radiative equilibrium should be true for the mid to upper stratosphere, because the τ_r is relatively small in these regions of the stratosphere.

It can be estimated how the stratospheric circulation responds to seasonal variations in the solar flux. A time scale for a dynamical process is

needed to estimate the seasonal variation in the stratospheric circulation, and is determined by the interhemispheric transfer of zonal momentum, because this process controls the seasonal variation of the meridional circulation. Our estimation of the dynamical time scale, τ_d, is the amount of time for an air parcel to move between hemispheres, because the movement of the parcel represents the momentum transfer between hemispheres. The expression of τ_d requires information on the vertical gradient of temperature and the values of τ_r ,

$$\tau_d = [\frac{H(\frac{\partial T}{\partial z} + \Gamma)}{\frac{\partial T_e}{\partial z}}]\tau_r \tag{1.3}$$

where H is the pressure scale height, Γ is adiabatic lapse rate, and T_e is the radiative equilibrium temperature (Flasar and Conrath 1990) The 1 mbar level is used for the evaluation of τ_d in the stratosphere. The τ_d of the stratosphere is then 5 τ_r . The seasonal response of the stratosphere circulation is expressed as a phase delay with respect to the seasonal solar forcing. This phase delay is $\approx 90°$ and implies that the seasonal variations of the circulation are one season behind solar forcing. We then predict that the northern hemisphere should have been upwelling during the Voyager fly-by (Figure 1.7). This prediction is consistent with the observations of temperatures and the distribution of the haze layer. The value of τ_d can also be used to predict

$$v_y^{1mbar} \sim \frac{R_T}{\tau_d} \tag{1.4}$$

and is $\sim$ 2 cm sec^{-1} (Flasar and Conrath 1990).

COMPOSITION AND CHEMISTRY

N_2 and CH_4 characterize the atmosphere of Titan. N_2 accounts for $\simeq$ 99% by molar fraction, but the abundance of N_2 is not certain. The noble gas, Ar, may be present in the atmosphere and introduces an uncertainty to

the abundance of N_2, because Ar is difficult to detect observationally. The origin of atmospheric N_2 may be revealed by the detection of atmospheric Ar. The N_2 is postulated to originate from surface ices if Ar exists in the atmosphere, because N_2 and Ar may have been present in the ices which accreted to form Titan. Otherwise, N_2 is the end result from the photodestruction of NH_3 (Gautier 1985). The occurance of CH_4 is easier to explain, because CH_4 is commonly found in the planetary atmospheres of the outer system. The surface is presumed to be the source of atmospheric CH_4 by degassing from ices or liquids. In the upper atmosphere, N_2 and CH_4 are dissociated. The atmosphere chemistry is initiated by the destruction of these two molecules. The products of the chemistry are generally simple hydrocarbons and nitrile compounds. Organic polymers are also produced in small amounts and condense out to produce haze material (Hunten 1985).

Hydrocarbons. The photodissociation of CH_4 leads to the production of other hydrocarbons. CH_4 is broken apart in two ways. The molecules can be destroyed by the UV from the solar flux,

$$CH_4 + h\nu \rightarrow {}^1CH_2 + H_2 \tag{1.5}$$

$$CH_4 + h\nu \rightarrow {}^3CH_2 + 2H \tag{1.6}$$

$$CH_4 + h\nu \rightarrow CH_3 + H \tag{1.7}$$

$$\tag{1.8}$$

for $\lambda \leq 0.145$ μm (Mordaunt *et al.* 1993). The direct dissociation leads to the production of C_2H_2, C_3H_4, and C_2H_4. The production of C_2H_2 is important, because it leads to another method of CH_4 dissociation. The catalytic destruction CH_4 is an indirect photodissociation and it starts by

$$C_{2n}H_2 + h\nu \rightarrow C_{2n} + H \quad n = 1, 2, 3 \tag{1.9}$$

which is followed by

$$C_{2n}H + CH_4 \rightarrow C_{2n}H_2 + CH_3. \tag{1.10}$$

The photodissociation of $C_{2n}H_2$ occurs for $\lambda \leq 0.3$ μm. Consequently, the catalytic destruction of CH_4 is the dominant method for dissociation, because the solar flux is greater in the wavelengths for the catalytic destruction of CH_4, and because the opacity of the atmosphere is less between 0.15 and 0.3 μm (Yung *et al.* 1984).

The production of the methyl radical, CH_3, leads to the formation of other hydrocarbons. Methyl radicals generally react to produce ethane, C_2H_6. Ethane can easily condense for the temperatures in the stratosphere, and is the dominate product of CH_4 dissociation, so the removal of ethane plays an important role in the evolution of atmospheric composition. If ethane does not condense out of the atmosphere, it can be photodissociated,

$$C_2H_6 + h\nu \rightarrow C_2H_5 + H \tag{1.11}$$

and the production of the radical, C_2H_5, leads to the higher alkenes (Hunten 1985). The higher hydrocarbons can also condense out of atmosphere, but they could react to form more complex organic compounds. Organic polymers are possibly produced and lead to the formation of the haze layer. The formation of the polymers strongly involves the chemistry of N_2.

N_2. The chemistry of N_2 is started by the dissociation of N_2. The two methods of N_2 are dominant in the atmosphere of Titan: by energetic electrons

$$^*e^- + N_2 \rightarrow N(^2D) + N(^4S) + e^-. \tag{1.12}$$

(Yung *et al.* al 1984), and by solar EUV

$$h\nu + N_2 \rightarrow 2N(^2D) \tag{1.13}$$

for $\lambda < 0.08$ μm (Strobel *et al.* 1992). Solar EUV or energetic electrons are needed to dissociate N_2 because its molecular bond is very strong. The largest source of energetic electrons is from the magnetosphere. Although small amounts are produced by cosmic rays. The production HCN is the main result of N_2 destruction.

$$N(^4S) + {}^3CH_2 \rightarrow HCN + H \tag{1.14}$$

$$N(^4S) + CH_3 \rightarrow HCN + 2H \tag{1.15}$$

$$N(^4S) + CH_3 \rightarrow H_2CN + H \tag{1.16}$$

$$H_2CN + H \rightarrow HCN + H_2. \tag{1.17}$$

The formation of HCN links the chemistry of N_2 and CH_4 (Strobel *et al.* 1985). The stoichemetric equation

$$N_2 + 2CH_4 \rightarrow 2HCN + 3H_2 \tag{1.18}$$

can be used to represent this linkage.

HCN affects the composition and optical properties of the atmosphere. The production of nitriles is one consequence from HCN and is started by the photodissociation of HCN

$$HCN + h\nu \rightarrow CN + H. \tag{1.19}$$

Nitriles can be produced by reactions between CN and hydrocarbons.

$$CN + C_{2n}H_2 \rightarrow HC_3N + H \tag{1.20}$$

$$CN + C_2H_4 \rightarrow C_2N_3CN + H \tag{1.21}$$

$$CN + HCN \rightarrow (CN)_2 + H. \tag{1.22}$$

The production of nitriles provides another link between N_2 and hydrocarbons. The linkage is repeated many times, because more CN radicals can

be added to carbon chains. The addition of CN affects the optical properties of the atmosphere, because the alteration of the carbon chain increases its absorption coefficient in the UV and visible (Hunten 1985). The carbon chains eventually condense into haze particles. High values of extinction characterized the haze layer in the UV and the visible (Khare *et al.* 1984).

Haze. The production of polyacetylenes are associated with the formation of haze material. Polyacetylenes can be produced by hydrogen atom cracking,

$$H + C_{2n}H_2 + M \rightarrow M + C_{2n}H_3 \quad n \geq 2 \tag{1.23}$$

$$H + C_{2n}H_3 \rightarrow C_2H_2 + C_{2n-2}H_2. \tag{1.24}$$

The production rate of polyacetylenes is influenced by the atmospheric loss of H_2 and H which occur by thermal escape. If loss rates are high, the products of CH_4 dissociation will be unsaturated with respect to condensation and the sources of polyacetylenes will have higher concentration, so the production of polyacetylene will be greater. High loss rates of H_2 and H also enhance the production of polyacetylene, because the reaction,

$$H + C_{2n}H_3 \rightarrow C_{2n}H_2 + H_2, \tag{1.25}$$

is fast when the concentrations of H are high. The production of polyacetylenes would be lowered in this case (Strobel *et al.* 1985). Once polyacetylenes are produced, they can serve as carbon chains for polymerization (Hunten 1985).

Haze material is produced by building upon the carbon chains. The building process is partially a competition for sites between two radicals, CN and CH_3. The result from this competition influences the production of the haze layer. If CH_3 take a site on the carbon chain, the saturation point of

the polymer will be lowered. Therefore, the addition of CH_3 directly affects the production rate of the haze material. If CN is added to a carbon chain, its absorption coefficient in the UV and IR will be increased (Hunten 1985). These are the optical properties which are characteristic of the haze layer (Khare *et al.* 1984). The ratio of CN to CH_3 which is added to a chain is then a tradeoff in the haze production. The tradeoff is between the mass production rate and the absorption coefficient. Both are important when evaluating the radiative properties of the haze layer. It is then difficult to forecast optical effects by varying the C to N ratio in the haze material. It also difficult, because the building of haze polymers is a more detailed process than outlined (Courtin *et al.* 1991 and McKay *et al.* 1991).

The production of the haze material is constrainted by photochemical models and laboratory simulations. Photochemical models weakly constrain the production rate of the haze material, because they can not simulate the formation of haze polymers. The models can set an upper limit for the production rate and estimate the upper limits from the reactions which eventually lead to haze polymers. These reactions include the dissociation of CH_4, the production of HCN, and the formation of acetylene (Table 1.2). Laboratory simulations of haze production define the properties of the haze material. These simulations used mixtures of N_2 and CH_4, and started chemical reactions by UV irradiation and electron bombardment. A brownish solid was eventually produced and was called tholin (Khare *et al.* 1984). Tholin has been produced for different mixtures of N_2 and CH_4 and its composition has been analyzed (Thompson *et al.* 1991). An elemental formula for the tholin is $C_{7.7}H_{58}N_{35}$ (McKay *et al.* 1991). The tholin is mainly used to estimate the absorption coefficient of the haze material (McKay *et al.* 1989 and Toon *et al.* 1992). Laboratory simulations of haze production may also be used for the production rate in Titan's atmosphere. This production rate has many

uncertainties, because of the differences between laboratory simulations and the atmospheric production of the haze material.

The production of the haze layer has been also studied by aerosol models (Toon *et al.* 1980, McKay *et al.* 1989, and Toon *et al.* 1992). In the models, the haze layer is simulated by microphysical and transport processes. The simulations of the haze layer are then tested by comparison to the observations of the geometric albedo. Two pieces of information are required to conduct and then test these simulations. First, a value of the haze production rate is needed and is implied by the photochemical models. Second, the radiative transfer calculations require a value for the haze absorption coefficient. The tholin is generally used. The geometric albedo from the aerosol models generally fit the observations without much manipulation. Consequently, the tholins have been to be proven a good analog of the haze material. Additionally, the pathways to haze production are shown to be basically understood. The simulations of the haze layer are used for the vertical distributions of haze density and average radii. The simulations of the haze layer were one dimensional and were for steady state conditions, so they did not evaluate variations over latitude and season.

Table 1.2: Reaction Rates for Pathways to Haze Material Production

Process	Column Rate†, gm cm^{-2} sec^{-1}
CH_4 Dissociation	$1.46x10^{-13}$
HCN Production	$1.63x10^{-14}$
C_2H_2 Production	$6.91x10^{-14}$
Haze Production *Inferred*	$\sim 10^{-14}$

†Based on the photochemical model in Toublanc *et al.* (1994).

Chapter 2

Effects of Time Varying Haze Production on Titan's Geometric Albedo

INTRODUCTION

Variations in the haze production were suggested to cause the variations in the geometric albedo (Lockwood 1977, Lockwood and Thompson 1979. Lockwood *et al.* 1986) before the Voyager fly-bys (Sromovsky *et al.* 1981). Pollack *et al.* 1980 proposed that the production variations were induced by the cycle of the solar UV flux This cycle of the solar UV flux is caused by the periodic variations in the solar magnetic field, and was proposed to be the cause of the variations in the haze layer, because this cycle of the UV variations has approximately the same period of the observed variations in the geometric albedo (13 years). The proposal for production variations was tested by using a one dimensional and steady state model of the haze

layer. Variations in the haze production were found to explain the observed variations in the geometric albedo, when the production rate changed by a factor of two. In the simulations by Pollack *et al.* (1980), the changes in the geometric albedo were produced by changing the altitude of optical depth unity. The increase in the haze production rate raised this altitude and put particles of smaller sizes at optical depth unity. The smaller particles decreased the geometric albedo, because of their decreased backscattering. Decreases in the haze production rate produced the reverse effect. (It is important to note that these changes were from changes of optical depth profile and not from changes in particle size at a given altitude.)

It is still valid to spectulate that variations in haze production cause the observed variations in the geometric albedo, but the basis for the speculation needs to be updated. It is a minor contention that the variations in the haze production are now postulated to be induced by the tilt of spin axis (27°). The induced variations in the haze production just have a different period of 29.5 years and are now asymmetric about the equator. The basis mainly needs to be updated for this speculation on production variations, because the conclusions in Pollack *et al.* (1980) were based on simulations of the haze layer which used pre-Voyager atmospheric composition, temperature, and pressure profiles (Toon *et al.* 1980). Additionally, the calculations of Pollack *et al.* (1980) were based on a steady state model and did not take into consideration time dependent effects. An accurate version of this Titan haze model was used in Toon *et al.* (1992), but the new model has not been previously used to re-evaluate the Pollack *et al.* (1980) conclusions.

The purpose of the following calculations is to determine whether a seasonally varying haze production rate can reproduce Titan's geometric albedo variations. Our approach was to use a time varying production rate in the

Toon *et al.* (1992) haze model and determine the resultant time dependent geometric albedo. The description of our research is based on a study in Hutzell *et al.* (1993) which was conducted by the main author as a part of his Ph. D. thesis.

DESCRIPTION OF THE TITAN HAZE MODEL

The Toon *et al.* (1992) Titan haze model is one dimensional in space and polydispersive in haze particle size distribution. The haze size distribution is described by 35 volume bins which span from 0.0013 to 3.0 μm in radius. The size bins are evenly spaced by a factor of two in volume. The number density of each size bin at a given altitude and time is evaluated by numerically solving its number continuity equation,

$$\begin{aligned}\frac{\partial n(v)}{\partial t} &= \frac{\partial}{\partial z}(n(v)v_s - K_E n_a \frac{\partial (n(v)/n_a)}{\partial z}) \\ &+ 0.5\int_0^v K(\nu, v-\nu)n(v-\nu)n(\nu)\,d\nu - \int_0^\infty K(\nu, v)n(v)n(\nu)\,d\nu \\ &+ q(v) - R_r n(v),\end{aligned}$$

where $n(v)$ is the number density of volume v particles, v_s is the particle sedimentation velocity. K_E is the vertical eddy diffusion coefficient, n_a is the atmospheric number density, K is the Brownian coagulation coefficient, $q(v)$ is the mass production rate, and R_r is the rainout constant. There are 35 coupled equations, which determine the haze structure.

The haze model attempts to simulate an aerosol layer which is produced at high altitudes from photochemistry. For the steady state calculations, the haze production profile and column production rate are constant with respect to time. Haze material is generated only in the smallest size bin and then coagulates into larger particles and sediments. For the microphysical

processes, the haze particles are assumed to be spherical. The Brownian coagulation coefficient includes an electrostatic repulsion from particle charging (Borucki *et al.* 1987). Haze transport also includes eddy diffusion. The haze particles can be removed by rainout which simulates the condensation at the tropopause of methane and photochemical products onto the haze particles. Two versions of the haze model are used and are referred to as the conventional and the revised models in Toon *et al.* (1992). The conventional model simulates Titan's haze by using model parameters which were determined by previous simulations of Titan's atmosphere. The revised model adjusted the model parameters to better fit observations which are related to Titan's haze such as the geometric albedo observations (Fink and Larson 1979, Neff *et al.* 1984, Courtin *et al.* 1991) and the Voyager observations of a detached haze layer (Rages and Pollack 1983).

The model parameters for the two versions are listed in Table 2.1. The most significant consequence of the differing model parameters is that the revised version had greater mass holding and effective radius values at higher altitudes. This resulted from the aerosol charging scheme and upwelling winds of the revised version. In the following calculations, both model versions were used to explore the range of albedo variation with respect to model parameters. For a more thorough description of the model versions and the numerical methods, Toon *et al.* (1988) and Toon *et al.* (1992) should be consulted.

Before proceeding with the time dependent calculations we first considered the mass production rate changes required to reproduce the range of the observed geometric albedo variations in a steady state calculation. Figure 2.1. shows the change in geometric albedo as a function of the change in mass production rate for steady state versions of the Toon *et al.* (1992) haze

models. The geometric albedo values are normalized to the values reported by Neff *et al.* (1984). One and two times the observed albedo variations from Lockwood *et al.* (1986) are also shown. These variations are not centered about unity because the Neff *et al.* (1984) data were taken at ≈1981.38 and are not the average values of the time varying albedo. We considered effects twice that reported by Lockwood *et al.* (1986) because the model calculations refer to observing the northern or southern hemisphere separately. The ratio of maximum to minimum production rates, γ, required to explain the observations was found to be approximately 2 to 4. The upper limit of γ was less well defined, because of the differing albedo curves at high production rates. For this range of γ values, the spectral dependence of the computed albedo variation approximately agreed with the observations(Table 2.2).

Haze production variations cannot be directly evaluated by present photochemical models (Yung *et al.* 1984, Yung 1987), because the heavier organics were not included. A possible guide to haze production variations is the seasonal variation of solar flux. From geometric considerations, the ratio of the hemispheric average daily solar flux between summer and winter hemispheres is approximately four. Allen *et al.* (1980) predicted a haze production variation of a factor of four with a factor of four variation in the UV photon flux from sunspot activity. However, their model did not include nitrogen compounds and they were modeling production changes from globally averaged solar UV flux, while the seasonal changes of solar flux are over all wavelengths and depends on latitude. Nevertheless, a factor of 2 to 4 seems to be within the range of attainable seasonal haze production variations.

It is not possible to infer the phase behavior of a time dependent model from the steady state results. In the steady state calculations, an inverse relationship exists between the albedo and a constant production rate, but a

Table 2.2: Maximum to Minimum Variation in the Geometric Albedo. $\Delta\%$.

Color	Lockwood *et al.* (1986) Observation	γ	Steady State Prediction	Time Dependent Result
Conventional Model				
Blue	10±1.3%	2.0	10.7%	1.80%
		4.0	20.2%	3.84%
Yellow	7±1.3%	2.0	4.65%	2.03%
		4.0	9.99%	4.13%
Revised Model				
Blue	10±1.3%	2.0	11.5%	0.577%
		4.0	30.9%	1.30%
Yellow	7±1.3%	2.0	7.74%	0.133%
		4.0	17.3%	0.350%

time dependent model can skew the above relationship due to slow response time(Sromovsky *et al.* 1981, Hutzell *et al.* 1991).

TIME VARYING CALCULATIONS

Method. To perform a time dependent calculations we have imposed a time varying production rate in the model. The functional form of the time varying production rate was arbitrary. Our only constraints were the phase and period of production. The production was chosen to instantaneously follow the seasonal solar forcing which varies at the angular frequency of Saturn's orbit ($2\pi/29.5$ years^{-1}). An amplitude given by an exponential of a sine function (see Figure 2.2) was selected for two reasons; production smoothly varies over time, and the selected value of γ can be greater than one.

The time dependent haze structure was computed until cyclic over a 29.5 year period, $\simeq$ 750 years of time integration. To better determine the resultant haze structure variations the model was changed in two ways from Toon *et al.* (1992). First, the time step of the numerical solution was decreased from 1.0 year to 0.5 years. Second, the vertical grid spacing was decreased below 120 km altitude from 10 km to 5 km. The resulting time variations in the blue and yellow geometric albedo are shown in Figure 2.3 for γ set to two and four.

In our calculations, the computed geometric albedo varied at the angular frequency of Saturn which was analogous to observing the variations of a single hemisphere. The observed geometric albedo actually varies at approximately twice the angular frequency of Saturn. because it is produced by viewing a combination of both hemispheres which are 180° out of phase. To

compare the model results to the observations (Figure 1.1 and Figure 1.3) it is necessary to fold in this geometrical effect of $\simeq 2$.

The Amplitude of the Albedo Variation. Table 2.2 gives the computed albedo variation (as percent difference between the maximum and minimum) for the time dependent model for γ values of 2 and 4, as well as the results from the steady state calculations.

There are significant differences between these two results. The obvious change is the large reduction of the albedo variation in time dependent modeling with respect to the steady state prediction. The amplitude of the albedo variation with respect to the two versions of the models also disagrees. In steady state calculations, the revised model predicted larger albedo variation than the conventional model for a given γ value, but in the time dependent modeling, the revised model actually gave smaller albedo variations than the conventional model. There are also differences in the relative results of the conventional and revised models. In addition, the spectral dependence. which in the steady state case agreed with the observations, is different when time dependence is included (see Table 2.2).

Changing the time dependent production rate was unsuccessful at increasing the size of the albedo variation. We considered a range of γ values from 2 to 1000 (see Table 2.1) as well as alternate forms for the time dependence of the production variation. The alternative form was a step function with a variable step size, and allowed production to vary discontinuously over time. Neither of these changes produced large enough albedo variations or time-averaged geometric albedos which were consistent with the observations.

We also attempted to increase the albedo variations by changing the parameters of haze model. The range of model parameters explored are shown

in Table 2.1. The changing of no single model parameter was able to increase the size of the albedo variation and also to produce the observed time averaged albedo, but a combination of production and transport parameters was able to accomplish this. The transport parameter which was the most successful at increasing the size of the albedo variations was raising the upper boundary where rainout occurs. The haze column production rate and the value of γ had to be simultaneously increased to agree with the observations. The revised model was the most successful for a 90 km upper rainout boundary, a haze column production rate of 2.2×10^{-14} g cm^{-2} s^{-1}, and a γ value of 16. The physical reality of these parameter values is uncertain primarily because it would imply tropospheric-like rain processes high in the stratosphere (Toon *et al.* 1988b).

Time Dependence of the Albedo Variation. Another important aspect of the simulations is the time behavior of the geometric albedo. The seasonal model of the hemispheric brightness contrast requires that a +90° phase delay exist between the albedo and seasonal solar forcing, because we have assumed production to be in phase with the solar forcing. The conventional model's albedo variations did exhibit a +90° phase delay, in agreement with the seasonal model. In the revised model, the albedo variation had a -60° phase delay (or 300° behind) with respect to seasonal solar forcing in conflict with the seasonal model.

Attempts to improve the phase behavior and simultaneously the size of the computed albedo variation were unsuccessful. For the model parameter settings which produced the observed size of the albedo variation (raising the upper rainout boundary), neither model was able to produce the correct phase delay. For the revised model, there was no change in the phase delay. For the conventional model, the parameter settings changed the phase delay

to a value near –60° . Attempts to maintain the original phase delay of the conventional model and to obtain the correct size of the computed albedo variation were unsuccessful. Therefore, a time varying production does not seem to be able to adequately explain Titan's observed albedo variation.

DISCUSSION

The Reduced Albedo Variation. To determine why the visible albedo variation from a time dependent production was much smaller than expected from steady state results and why a phase delay existed between the albedo and production rate, we have plotted the time behavior of the 0.55 μm optical depth at various altitudes for both versions of the haze model (Figure 2.3). The error bars show the change in optical depths between the maximum and minimum haze production rate predicted for steady state conditions. Comparison of these to the curves from the time dependent models illustrates the most probable reason for the reduced albedo variation. In the steady state case the variations of the optical depths with respect to production variations were much greater than in the time dependent calculations at the optical depths which primarily determine the albedo.

Figure 2.3 can be used to explain another discrepancy between the steady state and time varying calculations. In Table 2.2, the steady state and time varing calculations showed a greater difference in the revised model than in the conventional model. The cause can be seen in Figure 2.3, because the temporal variations in optical depths were smaller in the revised model than in the conventional model. Consequently, the seasonal variations in geometric albedo were smaller in the revised model than in the conventional model (as seen in Table 2.2).

Analytical Model. A simple analytical model illustrates why the optical depth at those altitudes behaves in this manner. To construct the analytical model, we assumed that the optical depth at an altitude, z, is dependent on the haze mass column density at z, $m(z)$,

$$m(z) = \int_z^\infty \rho_h(z)\, dz \tag{2.1}$$

where $\rho_h(z)$ is the haze mass holding at z. Therefore, the optical depth changes with time in proportion to the column density. In this simple model, the haze column density at a given altitude is governed by the differential equation

$$\frac{dm(z)}{dt} = -\frac{m(z)}{\phi} + A(1 + a\sin(\omega t)) \tag{2.2}$$

where ϕ is the haze material residence time above z. The value of ϕ is approximately the time averaged haze column density at z divided by the sedimentation flux at z. The second term on the right hand side is the time varying haze column production rate with an amplitude, A, and an amplitude of variation, a. The above equation's particular solution is

$$m(z) = A\phi + \frac{Aa\sin(\omega t - \delta)}{\sqrt{\omega^2 + (1/\phi)^2}} \tag{2.3}$$

where δ is the phase delay,

$$\delta = \arctan(\omega\phi). \tag{2.4}$$

Because the residence time for a majority of Titan's haze material is greater than several decades and ω is the angular frequency of Saturn, the $m(z)$ and optical depth values, which mostly determine the geometric albedo, reduce to the limit of $\omega \gg 1/\phi$. Hence, $m(z)$ and optical depth converge to the expression

$$m(z) = A(\phi - \frac{a\cos(\omega t)}{\omega}). \tag{2.5}$$

There are two consequences at these limits: 1) the phase of $m(z)$ (and optical depth) is 90° behind the forcing column production rate, and 2) the amplitude of variation is inversely related to forcing frequency. Most significant optical depths in both time dependent haze models approximately behaved in this manner (i.e. $\omega \gg 1/\phi$ for $\tau \gtrsim 1$). Therefore, long residence times prevented the predicted albedo changes, because the predicted optical depth changes implied by the steady state calculations cannot occur with a realistic time varying production rate.

If the above analytical models and numerical haze models are consistent with the predictions for the steady state case, the time variation of the optical depth profile and the geometric albedo will go to the time independent modeling predictions in the limit of $\omega \ll 1/\phi$. The actual cause of the haze production time variations can not have such long periods, because the only possible forcing periods are 29.5 years or less which correspond to the seasonal or solar cycles. In the limit $\omega \ll 1/\phi$, the analytical model is approximated by

$$m(z) = Ao(1 + a\sin(\omega t)). \tag{2.6}$$

Equation (2.7) converges to the steady state predictions because the time variation's amplitude is determined by ϕ and the variation is in phase with the forcing. The equivalent of Figure 2.3 with a 1000 year forcing period (Figure 2.4) shows that the time behavior of the optical depth is much closer to the steady state case which also agrees with the analytical model. The variations of the blue and yellow albedo versus forcing period (Figure 2.5) show convergence to the steady state calculations with increasing forcing period.

Phase Delay. Turning to the time dependence of the visible albedo, the revised model's visible albedo time behavior can be explained by considering

time independent modeling at different production rates which showed an inverse relationship between production and the visible albedo. (Pollack *et al.* 1980, Toon *et al.* 1980, McKay *et al.* 1989, Toon *et al.* 1992). (Higher haze production rates lowered the albedo by burying the bright Rayleigh scattering gas beneath the dark haze material and by changing the particle size at optical depth unity toward smaller radii which have lower backscattering cross sections. Both of these effects were consequences of higher haze mass column densities which were produced by higher production rates.) In the context of our simple analytic model, the visible albedo variations will then have a phase delay of $\delta - 180°$ and will be between $-180°$ and $-90°$. Large haze time scales will cause a phase delay between the albedo and production variations near $-90°$. A larger delay than predicted by the simple analytic model can arise for two reasons; 1) nonuniform responses to production though the haze, and 2) the time variation of other albedo-determining quantities such as the effective particle radius. For the time dependent revised model, the visible albedo delay was $-60°$ (close to the predicted range) but the time dependent conventional model had a visible albedo phase delay near $+90°$ which is not close to $\delta - 180°$. Clearly, the phase delay of the conventional model is not in line with the analytical model.

The difference of the phase response between the revised and conventional models can be understood in terms of the size variations of the haze particle which were close to optical depth unity. In the conventional model, the haze particles near this region were relatively small and had short formation time scales relative to the period of production variations. While for the revised model, the particle sizes near this region were large and had long formation time scales relative to the period of production variations. Consequently for the conventional model, the particle size variations near optical depth unity were larger and more rapidly responded to production

changes, in contrast to the revised model (Figure 2.6). These particle variations turned out to have a significant effect on the opacity structure and the geometric albedo. (The significant particle size variations also caused the different spectral dependence of the albedo between the time dependent and steady state conventional model (see Table 2.2).) Hence, the analytical model is too simple to properly represent the conventional model's phase delay, because two of the assumptions of the analytical model break down: 1) $\omega \gg 1/\phi$ at all significant optical depths, and 2) the particle size variations were negligible.

For the time dependent conventional model, the phase relationship between albedo and production variations was in agreement with observations (Sromovsky *et al.* 1981), if production is in phase with seasonal solar forcing. The spring hemispheric albedo (haze production is increasing from the average value) was lower than the fall hemispheric albedo. Unfortunately, the albedo variation was smaller than observed, because the seasonal changes of the model's optical depth profile and haze particle sizes were smaller than found in the steady state calculations.

As with the amplitude of the albedo response, the phase response for both models went to the values determined in the steady state case at long forcing periods (–180°).

Effects of Changing Model Parameters. The change of model parameters which increased the size of the albedo variation can be roughly understood in terms of our simple analytical model. The amplitude of the albedo variation can be increased by decreasing the haze material residence time scales. Increasing haze material removal processes is a method of accomplishing this. The three removal processes of our haze model are sedimentation, rainout, and diffusion. To remain consistent with the observations, sedimentation

and rainout are the best potential candidates, because diffusion tends to uniformly mix haze material over the entire spatial extent of the haze layer. Sedimentation can also be eliminated, because the sedimentation parameter, the particle density, is required to be at physically unrealistic values ($\gg 4$ g cm^{-3}). Rainout is therefore the only plausible candidate. Raising the rainout boundary increased the size of the computed albedo variation and reduced the spatial extent of the haze material. The net haze material residence time was thereby reduced by concentrating a majority of the haze material to an atmospheric region with a higher sedimentation velocity. To maintain the same average visible albedo it was necessary to increase the production rate ($4\times$). To match the albedo near 1 μm the surface albedo had to be increased to 0.2 from its nominal value of 0.1.

The haze still sluggishly responded to the production variations, because a large phase delay continued to exist ($-60°$) and a higher amplitude of production variation with respect to the steady state calculations was needed ($\gamma = 16$). The continued sluggishness was a result from increasing the column production rate to compensate for the higher rainout boundary.

With the raised rainout boundary and increased production rate the conventional model exhibited a phase delay more consistent with the revised model ($-60°$). This was a result of the reduction of the spatial extent of the haze and a decrease in the ability of haze material near optical depth unity to significantly vary over time, because the residence time of this section of the haze was increased.

Alternative Causes. Because of the inability of time variations in the haze production rate to account for the albedo variations, the time variations of other factors which determine the haze structure should be investigated. When attempting to use another factor, it is important to consider the time

dependence of the induced geometric albedo variations.

One group of other factors are associated with haze production. Besides the column production rate, this group includes the composition which affects the absorption coefficient of the haze (Sromovsky *et al.* 1989). The seasonal haze compositional variations are difficult to evaluate, because of the inability of photochemical models to simulate haze production. Some work on the problem has attempted to link latitudinal variations of brightness and observed gaseous species which are believed precursors of haze material (Courtin 1991). The implication is that the variations in gaseous species induce haze absorption variations. A negative correlation between the latitudinal variation of the HCN to C_2H_4 ratio on Titan and brightness is shown to exist (i.e. absorption increases with the HCN to C_2H_4 ratio). However, Courtin (1991) points out that the correlation conflicts with an earlier reported relationship between laboratory haze absorption and its N to C ratio (Scattergood *et al.* 1988). This conflict illustrates the difficulties of determining the seasonal variations of haze absorption.

Another group of factors which are involved in determining the haze structure are atmospheric properties such as circulation. Atmospheric circulation variations effect haze distribution and the optical depth profile through haze transport. Evidence for the role of circulation in producing the hemispheric brightness asymmetry and the geometric albedo variations was the sharp edge of the contrast at the equator (Smith *et al.* 1981). Although detailed modeling of the seasonal haze variations from atmospheric circulation has yet to be accomplished, there has been some work on the potential role of circulation. Flasar and Conrath (1990) suggested that seasonal variations of stratospheric circulation exhibit a phase delay of approximately +90°. if atmospheric properties are determined by a combination of radiative equilib-

rium and cyclostrophic dynamics. Their argument was based on observations of latitudinal variations of the atmospheric temperature structure (Flasar *et al.* 1981, and Flasar and Conrath 1990). The albedo effects of vertical advection from an upwelling wind were investigated in the revised model by Toon *et al.* (1992). Their results predict a decrease of the visible albedo with upwelling. Interestingly, upwelling in the darker spring hemisphere is consistent with the Voyager observations, and the +90° out of phase thermally indirect pole to pole cell in Flasar and Conrath (1990).

Time variation of the circulation can also effect the atmospheric thermal structure. Thermal structure variation might effect the haze and geometric albedo by altering haze microphysical processes and haze material composition. The former source of albedo variation is believed to be negligible. The latter is uncertain, because of the difficulties associated with determining haze composition.

Determining factors which control the geometric albedo will have to await more sophisticated modeling, laboratory research, and observations. To determine possible variation of haze composition, the construction of more complicated photochemical models is needed. The new photochemical models should include heavier organic compounds and the temporal variation of solar flux. An alternative method for exploring haze compositional variations is laboratory study. Such research has the potential to reveal aspects of haze composition which may be unattainable by photochemical models (Courtin *et al.* 1991). For evaluating the possible role of circulation, the present one-dimensional modeling is insufficient, because of the difficulties dealing with transport from atmospheric circulation (Toon *et al.* 1992). A two-dimensional haze model with dynamics is part of the solution to these difficulties which we will pursue in future work.

CONCLUSIONS

We have attempted to simulate amplitude and phase of the observed blue and yellow geometric albedo variations of Titan by using the conventional and revised versions of the Titan haze model from Toon *et al.* (1992). We draw the following conclusions from our calculations.

1. Steady state calculations suggest a variation of the haze production rate between a factor of two and four is enough to cause the observed geometric albedo variations. However, our Titan haze model with a smoothly varying haze production rate produces a much smaller magnitude of albedo variations with the same variation in production rate. This reduction in response is because the average haze time scale is much longer than the seasonal periodicity and prevents the required changes in the haze mass column density and particle sizes.

2. Alternate functional forms for the production which invoked discontinuous production changes and larger production rate variations did not improve the fit to observations. Changing model parameters did increase the size of the computed albedo variations, but the correct phase response of the albedo was not simultaneously produced. The increased albedo variation was accomplished by raising the upper rainout boundary, increasing the haze mass column production rate, and increasing the size of the production variations. These changes may be unphysical because they imply that rainout is occurring well into the stratosphere.

3. A consequence of the long haze time scales is a phase lag between the time variation of the albedo and production. The value of the produced

phase difference can agree with observations (Sromovsky *et al.* 1981), but it is sensitive to model parameters. The model parameter values that produced the best agreement with the size and spectral dependence of the geometric albedo variations did not yield the correct phase delay. Hence, models which only use variations of mass production rate to explain the albedo variations appear not to work.

Other time varying factors such as haze composition and atmospheric circulation could be used to explain the observed geometric albedo variations. The difficulty remains to evaluate the time variations of these other factors and what are the induced geometric albedo variations. The determination of a possible +90° phase delay between seasonal forcing and atmospheric circulation variations (Flasar and Conrath 1990) and the possible effect of vertical advection on the visible geometric albedo (Toon *et al.* 1992) are motivations to explore the effects of atmospheric circulation on the haze and the geometric albedo. To accomplish such a study, more sophisticated models of Titan's atmospheric circulation and haze are being constructed.

Chapter 3

The Wind Field in the Two Dimensional Model for the Haze Layer

INTRODUCTION

The circulation of the atmosphere is possible source of the variations in the observations of the geometeric albedo and hemispheric brightness, because it could vary atmospheric reflectivity by inducing variations in the distribution of the haze layer. To examination this potential of circulation, a representation of the circulation (i. e a wind field) has to be selected for the two dimensional model, so the variations in the haze layer can be simulated over time and space. Ideally, the wind field would come from a General Circulation Model. The GCM's for Titan are few and are highly

speculative, because the meteorological data for Titan is lacking. Another problem for GCM's is that the atmosphere is super-rotating, and that the zonal wind are postulated to be balance the meridional gradient of pressure (i. e. the cyclostrophic approximation); both conditions are extremely difficult to model. Therefore, the two dimensional model should use a wind field with a simple structure, so the results from our simulations are not too dependent upon the representation of the circulation. Consequently, our studies are limited to evaluate the basic effects on the reflectivity from horizontal and vertical advection of haze material.

The wind field in the two dimensional model should still approximate the actual circulation of the atmosphere, if the simulations are to reproduce the observations of the geometric albedo and the hemispheric brightness contrast. A meridional wind field can accomplish this goal, because the haze layer was observed to be zonally symmetric, and because the circulation is believed to be axially symmetric. The circulation is predicted to be axially symmetric, because baroclinic waves can not occur in the atmosphere of Titan (Leovy and Pollack 1973, and Hunten 1985). The GCM's for Titan support the prediction of axial symmetry, when the results from GCM's are averaged over season (Hourdin *et al.* 1991). A representation of the circulation can be simplified if the wind field is divided into two layers, the stratosphere and the troposphere, because the two layers have different thermal structures and time constants (Flasar *et al.* 1981 and Flasar and Conrath 1990). The wind field will then have different characteristics in the stratosphere and in the troposphere. The wind field in the stratosphere should be strong relative to the wind field in the troposphere, and it should also significantly vary over season. Conversely, the wind field for tropospheric circulation has a slow and weak variation over season. The wind field in the troposphere is then set to zero in our representation of the circulation, because its strength and

seasonal variation should not significantly alter the haze layer over season. The representation of the circulation is further simplified if the wind field in the stratosphere is one cell between the northern and southern poles. This simplification is justified by the dynamical processes which are proposed to control the meridional circulation (Flasar and Conrath 1990, and Flasar 1991). A Hadley circulation can be used to represent this cell, but a Hadley cell is thermally direct. The stratospheric circulation of Titan is predicted to be thermally indirect. The wind field for a Hadley cell can still be used to describe a thermally indirect cell, if the wind vectors of the Hadley cell are reversed.

The time variations of our wind field should be consistent with theory and observations. The temporal variations in the wind field are only seasonal, because of the goal of our simulations. The seasonal variations in the stratospheric circulation are predicted to lag behind the solar forcing by a season (90° of phase), because the time constant estimated for the stratospheric dynamics (Flasar and Conrath 1990, and Flasar 1991). In summary, our representation of the circulation is one cell which is located in the stratosphere and which is described as a reversed Hadley cell. The wind field in the two dimensional model has maximum strength or intensity at equinox.

Hadley circulations which are time dependent are described in the scientific literature (Leovy 1964, Held and Hou 1979, and Dunkerton 1988). These descriptions are not directly used for our wind field. Some descriptions are unsatisfactory, because a constant density or an incompressible atmosphere was assumed in the derivation. Other descriptions for Hadley circulation are unsatisfactory, because functions or numerical method are used in the solution, so the descriptions are relatively difficult to use. Consequently, the wind field in the two dimensional model is adapted from a simple derivation

which was previously done. Our adaptation yields an analytical solution which has a simple structure for the wind field. The solution was desired to be analytical, because it is self contained, so the wind field is easy to use in the simulations of the haze layer.

Houghton (1986) analytically derived the wind field of a Hadley cell. This derivation will be adapted for the two dimensional model. A constant density and the Boussinesq approximation were assumed in this derivation and can not be used to represent the circulation of the Titan's stratosphere, because the vertical extent of the stratospheric circulation is over several scale heights. The wind field in Houghton (1986) will be adapted by rederiving this wind field without the assumptions of a constant density and Boussinesq approximations. In our derivation, density and pressure exponentially vary over altitude by the scale height of the atmosphere

$$\rho = \rho_o \exp(\frac{-z}{H})$$
$$P = P_o \exp(\frac{-z}{H}).$$

where the scale height, H, is for an isothermal atmosphere. To simplify the governing equations of the derivation, two states, the zeroth and first order, describe the variables of the atmosphere and the circulation. The zeroth order refers to a static atmosphere. The first order refers to a dynamic atmosphere and is under steady state conditions. Consequently, our solution has to be modified so the wind field varies over season.

DERIVATION

The Governing Equations. The equations for our derivation are the thermodynamic, the momentum, and the mass continuity equations. These equations are approximated to the first order by an approach which was used

by Houghton (1986). Atmospheric variables are given as a sum of perturbed and unperturbed states which respectively represent an atmosphere with and without motion. Therefore, the total potential temperature, θ_T, density, ρ_T, and pressure, P_T, are expressed

$$\theta_T = \theta + \theta' \tag{3.1}$$

$$\rho_T = \rho + \rho' \tag{3.2}$$

$$P_T = P + P'. \tag{3.3}$$

The total wind velocity, $\vec{V}_T$, is expressed

$$\vec{V}_T = u'\,\hat{\mathbf{i}} + v'\,\hat{\mathbf{j}} + w'\,\hat{\mathbf{k}} \tag{3.4}$$

because the unperturbed state represents a static atmosphere. The unperturbed quantities, θ, ρ, and P, have a vertical variation for an isothermal atmosphere in hydrostatic equilibrium. Three approximations or assumptions further simplify the governing equations. 1) Quasi-geostrophic balance is assumed in the equations of motion. 2) The circulation is in equilibrium which is maintained by atmospheric heating and frictional dissipation. Therefore, the partial derivative with respect to time can be approximated as a frequency (i. e. $\partial/\partial t$ = constant). 3) The circulation is axially symmetric. Hence, there is no zonal variation of atmospheric quantities (i. e. $\partial/\partial x = 0$). Using these assumptions, we briefly will show how to obtain the first order governing equations.

The thermodynamical equation is exactly

$$\frac{d \ln \theta_T}{dt} = \frac{\gamma}{(\gamma - 1)} \frac{\dot{q}}{RT} \tag{3.5}$$

where γ is the ratio of the specific heats, R is the ideal gas constant, $\dot{q}$ is the heating rate per unit mass, and T is temperature. The right hand side of the thermodynamic equation is equal to the fractional rate of change of T and

is defined as Q. The left hand side of the thermodynamic equation can be expanded

$$\frac{d \ln \theta_T}{dt} = \frac{\partial}{\partial t} \ln[\theta(1 + \frac{\theta'}{\theta})] + \vec{V} \cdot \vec{\nabla} \ln[\theta(1 + \frac{\theta'}{\theta})]. \tag{3.6}$$

By neglecting the products of perturbed quantities and using the approximation (Holton 1979),

$$\ln(1 + \epsilon) \approx \epsilon \; for \; \epsilon \ll 1, \tag{3.7}$$

the advective term in equation (3.6) reduces to

$$\vec{V} \cdot \vec{\nabla} \ln[\theta(1 + \frac{\theta'}{\theta})] \approx Bw \tag{3.8}$$

where B is the stability parameter

$$B = \frac{\partial \ln \theta}{\partial z}. \tag{3.9}$$

By using the following relation

$$\ln \theta_T = \frac{1}{\gamma} \ln P_T - \ln \rho_T + constant \tag{3.10}$$

and the approximation from equation (3.7), the local time derivative in equation (3.6) reduces to

$$\frac{\partial}{\partial t} \ln[\theta(1 + \frac{\theta'}{\theta})] \approx \frac{1}{\gamma} \frac{\partial}{\partial t}(\frac{P'}{P}) - \frac{\partial}{\partial t}(\frac{\rho'}{\rho}). \tag{3.11}$$

The first order of thermodynamic equation is then

$$\frac{\partial}{\partial t}(\frac{\rho'}{\rho}) - \frac{1}{\gamma} \frac{\partial}{\partial t}(\frac{P'}{P}) - Bw = -Q \tag{3.12}$$

and is further simplified by our assumption of equilibrium. Energetically. the spatial variation of solar flux drives the circulation so atmospheric radiation maintains equilibrium in the circulation. Hence, the time derivatives of thermodynamic equation are approximated by α which is one over the radiative time constant,

$$\alpha(\frac{\rho'}{\rho}) - \frac{\alpha}{\gamma}(\frac{P'}{P}) - Bw = -Q \tag{3.13}$$

(modified equation (8.19) from Houghton 1986).

The vertical equation of motion is to the first order approximation of the hydrostatic equation,

$$\frac{1}{\rho}\frac{\partial P'}{\partial z} + (\frac{\rho'}{\rho})g = 0, \tag{3.14}$$

(equation (10.4) from Houghton 1986), because of the steady state circulation and hydrostatic equilibrium. The ideal gas law relates the ρ and P,

$$P = \frac{\rho RT}{\mu}. \tag{3.15}$$

where the mean molecular weight of the atmosphere is μ.

The horizontal equations of motion are simplified by the axial symmetry and quasi-geostrophic approximations. These two equations are to the first order

$$\frac{\partial u}{\partial t} - fv = 0 \tag{3.16}$$

$$\frac{\partial v}{\partial t} + fu = -\frac{1}{\rho}\frac{\partial P'}{\partial y} \tag{3.17}$$

where f is the coriolis parameter. The time derivative is approximated by r which is one over the time constant for frictional dissipation

$$ru - fv = 0 \tag{3.18}$$

$$rv + fu = -\frac{1}{\rho}\frac{\partial P'}{\partial y}, \tag{3.19}$$

because frictional dissipation maintains equilibrium in the horizontal winds. The horizontal equations of motion can be combined to give

$$Av = -\frac{1}{\rho}\frac{\partial P'}{\partial y} \tag{3.20}$$

where

$$A = \frac{r^2 + f^2}{r}. \tag{3.21}$$

The mass continuity equation is approximated

$$\frac{\partial \rho v}{\partial y} + \frac{\partial \rho w}{\partial z} = 0, \tag{3.22}$$

by using the assumptions of axial symmetry and equilibrium in the circulation. This equation becomes

$$\frac{\partial v}{\partial y} + \frac{\partial w}{\partial z} - \frac{w}{H} = 0. \tag{3.23}$$

when density exponentially varies over altitude by the scale height, H. The mass continuity equation is used to define a streamfunction, ψ, so the velocities, v and w, are expressed

$$v = \frac{\psi}{H} - \frac{\partial \psi}{\partial z} \tag{3.24}$$

$$w = \frac{\partial \psi}{\partial y}. \tag{3.25}$$

The Equation for the Streamfunction, ψ. The next step in the derivation is to manipulate the governing equations into an equation for ψ. We begin by evaluating the partial derivatives of the thermodynamic equation and the vertical equation of motion with respect to y,

$$\alpha \frac{\partial}{\partial y}\left(\frac{\rho'}{\rho}\right) - \frac{\alpha}{\gamma}\frac{\partial}{\partial y}\left(\frac{P'}{P}\right) - B\frac{\partial w}{\partial y} = -\frac{\partial Q}{\partial y} \tag{3.26}$$

$$\frac{1}{\rho}\frac{\partial^2 P'}{\partial y \partial z} = -g\frac{\partial}{\partial y}\left(\frac{\rho'}{\rho}\right). \tag{3.27}$$

The partial derivative of equation (3.20) with respect to z yields

$$A\frac{\partial v}{\partial z} = -\frac{1}{\rho H}\frac{\partial P'}{\partial y} - \frac{1}{\rho}\frac{\partial^2 P'}{\partial z \partial y}. \tag{3.28}$$

Equation (3.27),

$$\frac{\partial}{\partial y}\left(\frac{\rho'}{\rho}\right) = -\frac{1}{\rho g}\frac{\partial^2 P'}{\partial y \partial z}, \tag{3.29}$$

is used, and equation (3.26) becomes

$$-\frac{\alpha}{\rho g}\frac{\partial^2 P'}{\partial y \partial z} - \frac{\alpha}{\gamma}\frac{\partial}{\partial y}\left(\frac{P'}{P}\right) - B\frac{\partial w}{\partial y} = -\frac{\partial Q}{\partial y}. \tag{3.30}$$

The relation from equation (3.28),

$$-\frac{\alpha}{\rho g}\frac{\partial^2 P'}{\partial y \partial z} = \frac{\alpha A}{g}\frac{\partial v}{\partial z} + \frac{\alpha}{\rho g H}\frac{\partial P'}{\partial y}, \tag{3.31}$$

is used, and equation (3.30) can be rewritten

$$\frac{\alpha A}{g}\frac{\partial v}{\partial z} + \frac{\alpha}{\rho g H}\frac{\partial P'}{\partial y} - \frac{\alpha}{\gamma}\frac{\partial}{\partial y}(\frac{P'}{P}) - B\frac{\partial w}{\partial y} = -\frac{\partial Q}{\partial y}. \tag{3.32}$$

The ideal gas law can be used for the relation,

$$\frac{\partial}{\partial y}(\frac{P'}{P}) = \frac{\mu}{\rho R T}\frac{\partial P'}{\partial y} \tag{3.33}$$

if P is independent of y. This relation is used in equation (eq3.32)

$$\frac{\alpha A}{g}\frac{\partial v}{\partial z} + (\frac{\alpha}{\rho g H} - \frac{\alpha \mu}{\gamma R T})\frac{\partial P'}{\partial y} - B\frac{\partial w}{\partial y} = -\frac{\partial Q}{\partial y}. \tag{3.34}$$

Equation (3.20) is used along with the definition of the scale height,

$$H = \frac{RT}{\mu g}. \tag{3.35}$$

Hence, equation (3.34) can be rewritten

$$\frac{\alpha A}{g}\frac{\partial v}{\partial z} - \frac{\alpha A}{g H}(1 - \frac{1}{\gamma})v - B\frac{\partial w}{\partial y} = -\frac{\partial Q}{\partial y}. \tag{3.36}$$

The streamfunction, ψ, is substituted into equation (3.36)

$$-\frac{\alpha A}{g}\frac{\partial^2 \psi}{\partial^2 z} - \frac{\alpha A}{g H}(\frac{1}{\gamma} - 2)\frac{\partial \psi}{\partial z} - \frac{\alpha A}{g H^2}(1 - \frac{1}{\gamma})\psi - B\frac{\partial^2 \psi}{\partial^2 y} = -\frac{\partial Q}{\partial y}. \tag{3.37}$$

We will rewrite the equation (3.37) into the form

$$\frac{\partial^2 \psi}{\partial^2 z} + D\frac{\partial \psi}{\partial z} + E\psi + C\frac{\partial^2 \psi}{\partial^2 y} = F\frac{\partial Q}{\partial y} \tag{3.38}$$

and define the constants,

$$C = \frac{Bg}{A\alpha} \tag{3.39}$$

$$D = \frac{1}{H}(\frac{1}{\gamma} - 2) \equiv -\frac{\kappa}{H} \tag{3.40}$$

$$E = \frac{1}{H^2}(1 - \frac{1}{\gamma}) \equiv \frac{(\kappa - 1)}{H^2} \tag{3.41}$$

$$F = \frac{g}{A\alpha}. \tag{3.42}$$

An integrating factor of, e^{Dz}, is used to rewrite the equation for ψ

$$\frac{\partial}{\partial z}(e^{Dz}\frac{\partial \psi}{\partial z}) + Ee^{Dz}\psi + Ce^{Dz}\frac{\partial^2 \psi}{\partial^2 y} = Fe^{Dz}\frac{\partial Q}{\partial y} \tag{3.43}$$

The Solution for ψ. In Houghton (1986), ψ and v were defined to be zero at the horizontal boundaries (i. e. at $y = 0$ and $y = L$). The implication is that ψ and the wind field oscillates horizontally. Hence, we will expand ψ in terms of the horizontal eigenfunctions (Haberman 1983)

$$\psi = \sum_{n=1}^{\infty} b_n(z)\sin(\frac{n\pi y}{L}). \tag{3.44}$$

This trial solution for ψ is substituted into equation (44) and gives

$$\sum_{n=1}^{\infty}\{\frac{\partial}{\partial z}(e^{Dz}\frac{\partial b_n}{\partial z}) + (E - C(\frac{n\pi}{L})^2)e^{Dz}b_n\}\sin(\frac{n\pi}{L}) = Fe^{Dz}\frac{\partial Q}{\partial y}. \tag{3.45}$$

The orthogonality of $\sin(\frac{n\pi}{L})$ decouples the equations for $b_n(z)$. The general equation for $b_n(z)$ is then

$$\frac{\partial}{\partial z}(e^{Dz}\frac{\partial b_n}{\partial z}) + (E - C(\frac{n\pi}{L})^2)e^{Dz}b_n = S_n \tag{3.46}$$

where S_n is the nth moment of the forcing term

$$S_n = \frac{L}{2}\int_0^L Fe^{Dz}\frac{\partial Q}{\partial y}\sin(\frac{n\pi y}{L})\,dy. \tag{3.47}$$

The same expression for the heating rate used as in Houghton (1986)

$$Q = Q_o\cos(\frac{\pi y}{L})\sin(\frac{\pi z}{W}) \tag{3.48}$$

where W is the height of the cell. The moments of the forcing term are

$$S_n = Fe^{Dz}Q_o(\frac{\pi}{L})\sin(\frac{\pi z}{W}) \quad n = 1 \tag{3.49}$$

$$S_n = 0 \quad n \neq 1 \tag{3.50}$$

The values of the moments imply that only $b_1(z)$ is nonzero. The equation for $b_1(z)$ is

$$\frac{\partial}{\partial z}(e^{Dz}\frac{\partial b_1}{\partial z}) + \chi^2 e^{Dz} b_1 = S_1 \tag{3.51}$$

where

$$\chi^2 = E - C(\frac{\pi}{L})^2 \tag{3.52}$$

or

$$\chi^2 = \frac{(\kappa - 1)}{H^2} - C(\frac{\pi}{L})^2. \tag{3.53}$$

The solution for $b_1(z)$ or $b(z)$ can be obtained by the method of the variation of parameters. We begin by solving the homogeneous equation (i. e. $S_1 = 0$),

$$\frac{\partial}{\partial z}(e^{Dz}\frac{\partial b}{\partial z}) + \chi^2 e^{Dz} b = 0 \tag{3.54}$$

or

$$\frac{\partial^2 b}{\partial^2 z} + D\frac{\partial b}{\partial z} + \chi^2 b = 0. \tag{3.55}$$

There are two solutions for the equation,

$$e^{\lambda_1 z} \ and \ e^{\lambda_2 z}, \tag{3.56}$$

where

$$\lambda_{1.2} = \frac{-D \pm \sqrt{D^2 - 4\chi^2}}{2}. \tag{3.57}$$

The expression for $\lambda_{1,2}$ can be rewritten to

$$\lambda_1 = \frac{1}{2\gamma H}\{(2\gamma - 1) + ((\left(2\gamma H(\frac{\pi}{L})\right)^2 C + 1)^{\frac{1}{2}}\} \tag{3.58}$$

and

$$\lambda_2 = \frac{1}{2\gamma H}\{(2\gamma - 1) - ((\left(2\gamma H(\frac{\pi}{L})\right)^2 C + 1)^{\frac{1}{2}}\}. \tag{3.59}$$

The general solution for b is given by,

$$\begin{aligned} b(z) &= -e^{\lambda_1 z}\int_0^z \frac{S_1 e^{\lambda_2 x} dx}{e^{Dx}(\lambda_2 e^{(\lambda_1+\lambda_2)x} - \lambda_1 e^{(\lambda_1+\lambda_2)x})} \\ &+ e^{\lambda_2 z}\int_0^z \frac{S_1 e^{\lambda_1 x} dx}{e^{Dx}(\lambda_2 e^{(\lambda_1+\lambda_2)x} - \lambda_1 e^{(\lambda_1+\lambda_2)x})} \\ &+ C_1 e^{\lambda_1 z} + C_2 e^{\lambda_2 z}. \end{aligned} \tag{3.60}$$

The terms in the integrand can be simplified,

$$\frac{S_1}{e^{Dz}} = \frac{FQ_o\pi}{L}\sin(\frac{\pi x}{W}), \tag{3.61}$$

$$\frac{e^{\lambda_1 x}}{(\lambda_2 e^{(\lambda_1+\lambda_2)x} - \lambda_1 e^{(\lambda_1+\lambda_2)x})} = \frac{e^{-\lambda_2 x}}{(\lambda_2 - \lambda_1)} \tag{3.62}$$

$$= -\frac{2\gamma H e^{-\lambda_2 x}}{[1+(2\gamma H(\frac{\pi}{L}))^2 C)]^{\frac{1}{2}}}, \tag{3.63}$$

and

$$\frac{e^{\lambda_2 x}}{(\lambda_2 e^{(\lambda_1+\lambda_2)x} - \lambda_1 e^{(\lambda_1+\lambda_2)x})} = \frac{e^{-\lambda_1 x}}{(\lambda_2 - \lambda_1)} \tag{3.64}$$

$$= -\frac{2\gamma H e^{-\lambda_1 x}}{[1+(2\gamma H(\frac{\pi}{L}))^2 C)]^{\frac{1}{2}}}, \tag{3.65}$$

so the solution for $b(z)$ becomes

$$\begin{aligned} b(z) &= \beta\{-e^{\lambda_1 z}\int_0^z e^{-\lambda_1 x}\sin(\frac{\pi x}{W})dx \\ &+ e^{\lambda_2 z}\int_0^z e^{-\lambda_2 x}\sin(\frac{\pi x}{W})dx\} \\ &+ C_1 e^{\lambda_1 z} + C_2 e^{\lambda_2 z} \end{aligned} \tag{3.66}$$

where

$$\beta = -\frac{g(2\gamma H(\frac{\pi}{L}))(\frac{q_o}{\alpha A})}{[1+g(2\gamma H(\frac{\pi}{L}))^2(\frac{B}{\alpha A})]^{\frac{1}{2}}}. \tag{3.67}$$

The identity

$$\int_0^x e^{au}\sin(bu)du = \frac{1}{a^2+b^2}[b - e^{-ax}(a\sin(bx) + b\cos(bx))], \tag{3.68}$$

and the redefinition of C_1 and C_2 are used to obtain the solution for $b(z)$,

$$b(z) = \sigma_1\sin(\frac{\pi z}{W}) + \sigma_2\cos(\frac{\pi z}{W}) + C_1 e^{\lambda_1 z} + C_2 e^{\lambda_2 z} \tag{3.69}$$

where

$$\sigma_1 = \beta\{\frac{\lambda_1}{\lambda_1^2 + (\frac{\pi}{W})^2} - \frac{\lambda_2}{\lambda_2^2 + (\frac{\pi}{W})^2}\} \tag{3.70}$$

and

$$\sigma_2 = \frac{\pi\beta}{W}\{\frac{1}{\lambda_1^2 + (\frac{\pi}{W})^2} - \frac{1}{\lambda_2^2 + (\frac{\pi}{W})^2}\}. \tag{3.71}$$

The constants, C_1 and C_2, can be determined if the boundary conditions are a rigid top and a rigid bottom (i. e. $b(z = 0)$ and $b(z = W)$ equal zero). The solution for $b(z)$ is then

$$b(z) = \sigma_1 \sin(\frac{\pi z}{W}) + \sigma_2(\cos(\frac{\pi z}{W}) - e^{\lambda_2 z}) + \sigma_3(e^{\lambda_1 z} - e^{\lambda_2 z}) \tag{3.72}$$

where

$$\sigma_3 = \frac{(1 + e^{\lambda_2 W})\sigma_2}{(e^{\lambda_1 W} - e^{\lambda_2 W})}. \tag{3.73}$$

We want to define parameters which control the strength of the wind field. This is accomplished by rewritting β,

$$\beta = \frac{g(2\gamma H(\frac{\pi}{L}))\eta\xi}{[1 + g(2\gamma H(\frac{\pi}{L}))^2 B\xi]^{\frac{1}{2}}} \tag{3.74}$$

where η is related the heating rate

$$\eta = Q_\circ \tag{3.75}$$

and ξ is related to the time constants of the atmosphere.

$$\xi = \frac{1}{\alpha A} = \frac{r}{\alpha(r^2 + f^2)}. \tag{3.76}$$

The terms, η and ξ, are to be the parameters of the wind field. The static stability of the atmosphere, B, is for an isothermal atmosphere,

$$B = \frac{(\gamma - 1)}{\gamma H}. \tag{3.77}$$

The eigenvalues of $b(z)$ are then rewritten to

$$\lambda_1 = \frac{1}{2\gamma H}\{(2\gamma - 1) + (g\left(2\gamma H(\frac{\pi}{L})\right)^2 B\xi + 1)^{\frac{1}{2}}\} \tag{3.78}$$

and

$$\lambda_2 = \frac{1}{2\gamma H}\{(2\gamma - 1) - (g\left(2\gamma H(\frac{\pi}{L})\right)^2 B\xi + 1)^{\frac{1}{2}}\}. \tag{3.79}$$

The definitions in equations (3.24) and (3.25) give the vertical and meridional winds, w and v,

$$v = \left(\frac{b(z)}{H} - \frac{\partial b(z)}{\partial z}\right)\sin(\frac{\pi y}{L}) \tag{3.80}$$

$$w = -\frac{\pi b(z)}{L}\cos(\frac{\pi y}{L}) \tag{3.81}$$

where

$$\frac{\partial b(z)}{\partial z} = \sigma_2(\frac{\pi}{W}\sin(\frac{\pi z}{W}) - \lambda_2 e^{\lambda_2 z}) - \frac{\pi\sigma_1}{W}\cos(\frac{\pi z}{W}) + \sigma_3(\lambda_1 e^{\lambda_1 z} - \lambda_2 e^{\lambda_2 z}). \tag{3.82}$$

To illustrate the wind field from our derivation, the streamlines and the isocontours of v and w are given (Figure 3.1 and Figure 3.2). The constant in ψ, v, and w are given in the following section.

APPLICATION TO TITAN

The wind field from our derivation has to be fitted to represent the circulation in the two dimensional model. The atmospheric variables are defined in Table 3.1 and are for the the stratosphere of Titan. The quantities in Table 3.1 contain uncertainties, because they are averaged over the stratosphere. The stratosphere spans several scale heights, so ρ and P vary order of magnitudes. The values for α and r vary. Hence, the wind field should be considered a gross average over space and time. The parameters in the derivation, η and ξ, can be use to adjust the wind field within this uncertainties in our representation of the circulation.

One parameter, η, should not be used as a free parameter of the wind field. The value of η is related to the solar flux on Titan, because it is net

Table 3.1: Physical Constant of Titan's Stratosphere

Physical Constants of Titan's Stratosphere		
Height of Cell	W	$\simeq$ 250 km
Length of Cell	L	$\simeq$ 8090 km
Scale Height	H	$\simeq$ 30 km
Specific Heat at constant pressure	c_P	$\simeq 1.04\times10^{7}$ ergs gm^{-1} K^{-1}
Ratio of Specific Heats	γ	1.4
Gram Molecular Weight	μ	$\simeq$ 28
Stratospheric Pressure	P_s	1×10^{2} to 1×10^{5} dyn cm^{-2}
Stratospheric Temperature	T_s	70 to 170 K
Gravitational Acceleration	g	$\simeq$ 120 cm sec^{-2}
Coriolis Parameter	f	$\simeq 2.3\times10^{-6}$ sec^{-1}
Radiative Time Constant	$1/\alpha$	$\approx 1\times10^{7}$ to 1×10^{8} sec
Solar Flux	S_O	$\simeq 1.5\times10^{4}$ erg sec^{-1} cm^{-2}

heating rate in the stratosphere. , its value can be estimated in several ways. The values of η can be approximated by the expression,

$$\eta = \alpha \frac{(T_e - T_s)}{T_s} \tag{3.83}$$

where T_e is the radiative equilibrium temperature and T_s is the stratospheric temperature. The above expression describes the heating rate from radiative equilibrium and can be partially derived from dimensional analysis (Houghton 1986). The values for $\frac{(T_e - T_s)}{T_s}$ range from 1×10^{-2} to 1×10^{-3} (McKay *et al.* 1989), when the values of T_s and T_e are respectively taken from the observations and from models of radiative equilibrium. The values of α range from 1×10^{-7} to 1×10^{-11} $\sec^{-1}$ (Flasar *et al.* 1981 and Flasar and Conrath 1990). Therefore, η can be from 1×10^{-9} to 1×10^{-14} $\sec^{-1}$. A values for η are also directly evaluated of $\frac{1}{T}\frac{\partial T}{\partial t}$ from detailed models of radiative transfer. The values for η is 1×10^{-8} to 1×10^{-10} $\sec^{-1}$ in these models (Del Genio *et al.* 1993). The values for η overlap between these two methods. The value of η is set at 1×10^{-10} $\sec^{-1}$ which is approximately in the middle of our estimated range of magnitudes.

The parameter, ξ, is used as a free parameter of the wind field because it is used to adjust the strength of the wind field. The strength of the wind should match theoretical estimates for the strength of the meridional winds in the stratosphere. The values of the meridional wind is estimated on the order of 1 cm $\sec^{-1}$ at unity optical depth in the visible (Flasar and Conrath 1990); $z \sim 110$ km (McKay *et al.* 1989 and Toon *et al.* 1992). Two quantities of the wind field, v_{ave}, and v_{max}, are used to match this theoretical estimate by their tabulation as a function of ξ (Figure 3.3). The average of the meridional wind, v_{ave}, was weighted about the center of the wind field (Figure 3.3a). The maximum of the meridional wind, v_{max}, was located at the top of the wind field (Figure 3.3b). The values of ξ matched the theoretical estimates when

it ranged from 1×10^{8} to 1×10^{10} sec^2. The values of ξ have a large range, because the meridional wind, v, varies orders of magnitude over altitude. Another quantity of interest is the time for a particle to travel once around the center of the wind field, τ. This time was averaged, τ_{ave}, over different altitudes which were for the initial location of the particles. The values of τ_{ave} (Figure 3.3c) varied from 1000 to 10 years for the stated range of ξ. The value of τ at $\sim$ 110 km was also computed as a function of ξ (Figure 3.3d). Both v_{ave} and τ_{ave} vary linearly with respect to ξ.

Our values for η can be tested if they are possible in the stratosphere of Titan. The definition of η contains the time constant for frictional dissipation, so r can evaluated. The value of r is approximated by

$$\frac{1}{r} = \alpha\xi \tag{3.84}$$

because the coriolis parameter, f, is small for Titan. For values of ξ and η producing the theoretical estimates of the meridional wind, r in Titan's stratosphere is $\sim 1\times10^{5}$ sec and is consistent to other estimates (Flasar and Conrath 1990 and Hourdin *et al.* 1991). Our value of r can also be used to evaluate the horizontal eddy diffusion coefficient, K_H, if the approximation

$$K_H \sim rH^2 \tag{3.85}$$

is used (Held and Hou 1980). The values of K_H are then $\sim 1\times10^{7}$ cm^2 sec^{-1} and are also close previous estimates of K_H (Del Genio *et al.* 1993).

Seasonal Variations in the Circulation. The wind field from the derivation has to be further modified for our representation of the circulation. The derivation was for equilibrium conditions, while our representation has to contain seasonal variations. The modification of the wind field is accomplished by using a multiplier which produces variations over season. The

expressions for the wind speeds, equations (81) and (82), are multiplied by

$$sin(\omega_s t + \varphi), \tag{3.86}$$

where ω_s is the angular frequency of the seasonal cycle ($\frac{2\pi}{29.5}\ year^{-1}$) and φ is the initial phase. The value of φ determines the initial strength of wind field and the hemisphere which is initially upwelling. We will also define φ as the phase lag of the circulation with respect to the seasonal variations in the solar flux. This definition is misleading, because the solar forcing in the derivation was independent with respect to time. The value of φ is used as a phase delay because it determines when the strength of the wind field is maximum with respect to solstice. Solstice and equinox determine the viewing of Titan in the computations for the geometric albedo. The value of φ then determines whether the observer is predominately seeing the haze variations from upwelling or downwelling. The strength of the wind field is predicted maximum at equinox. so $\varphi \sim 90°$ (Flasar and Conrath 1990). The temporal variations of the wind field attempt to be approximately consistent with to the seasonal variations in the stratospheric circulation which have been postulate (Flasar *et al.* 1981, Rages and Pollack 1983. Flasar and Conrath 1990).

The method of temporally variation may be justified by scale analysis. Our temporal variation of the wind field is considered to be produced if the forcing term, Q, varies as the modulator of the wind speeds, equation (87). The partial derivatives with respect to time are then corrected by an additional term, the seasonal frequency (i. e. 1/29.5 years). A large error is introduced by our modification of the wind field with respect to time, if

$$\frac{(r+\alpha)}{r\alpha} < \frac{1}{29.5}. \tag{3.87}$$

We can then justify our temporal variation of the wind field, if the wind field is in quasi-equilibrium to the temporal variations in the heating rate. The

radiative time constant, $1/\alpha$, is on the order of 10^7 sec. The time constant for frictional dissipation, $1/r$, is on the order of 10^5 sec. One year for Titan is on the order of 10^8 sec. Therefore, the additional term from seasonal variation of Q is a second order correction and is not a large violation of the assumption of equilibrium in our derivation.

Chapter 4

Time Varying Simulations of the Geometric Albedo of Titan by a Two Dimensional Haze Model

INTRODUCTION

In chapter 2, time variations of haze mass production were determined to be an unlikely source of the observed variations in the geometric albedo and in the hemispheric brightness. The seasonal cycle of the stratospheric circulation was then given as an alternative source. This claim was primarily

based on two theoretical studies. The first study deals with the atmospheric circulation at the optical depths which mostly determine the visible geometric albedos (Flasar *et al.* 1990). The circulation of the stratosphere was determined to be a pole to pole cell which is thermally indirect. The variations of this circulation should lag behind the seasonal variations of solar forcing by one season or 90° (Flasar *et al.* 1981 and Flasar and Conrath 1990). The stratospheric circulation then has maximum upwelling and downwelling at the equinoxes. The second work deals with the changes in the haze structure and consequently the geometric albedo from the circulation. Toon *et al.* (1992) placed an upwelling wind into a haze model which was one dimensional and steady state. In the visible wavelengths, the upward wind decreased the geometric albedo. Further calculations show the changes in the geometric albedo from a vertical wind (Figure 4.1). The haze model in Toon *et al.* (1992) was used for these calculations. The change of geometric albedo was computed between two haze simulations which had the same wind speed but in opposite directions. The vertical wind was a constant between 50 and 300 km in altitude and its value was used for a parameter study. Figure 4.1 shows the percentage change of the 0.55 and 0.47 μm geometric albedo versus wind speed. The observed variation in the geometric albedo is produced at speeds between 0.002 to 0.004 cm sec^{-1} which are consistent with theoretical estimates of stratospheric winds (Flasar *et al.* 1981).

The following scenario illustrates the potential of atmospheric circulation to explain the variations in the geometric albedo and the hemispheric brightness. At northern spring equinox, the northern hemisphere is upwelling so it ought to be dark or darkening (Toon *et al.* 1990). Conversely, the southern hemisphere is downwelling so it ought to be bright or brightening. The configuration of hemispheric brightness or reflectivity agrees with the observations (Sromovsky *et al.* 1981). If we extrapolate over time by one year for

Titan, the geometric albedo and the hemispheric brightness vary, because the circulation varies over seasons and induces variation of reflectivity over latitude. The seasonal variations in the geometric albedo and hemispheric brightness agree between the observations (Lockwood 1986 and Caldwell *et al.* 1992) and our scenario, because the circulation responses behind the seasonal variations in the solar forcing by 90° (Flasar *et al.* 1990), and because the circulation is assumed to instantaneously produce changes in reflectivity over latitude.

Our scenario is weakened by reliance on a haze model which is steady state and one dimensional. This model did not account for effects on the haze distribution from horizontal transport. The determination of the albedo effects was not even attempted by an one dimensional model with a time varying vertical wind because the lack of horizontal transport would produce unrealistic haze simulations. Two dimensional modeling is a better way to determine the geometric albedo effects from atmospheric circulation.

In the following study, the effects from atmospheric circulation on the Titan's haze and the geometric albedo are evaluated. Circulation is represented by a time varying and two dimensional wind field and drives haze variations. The simulations of the geometric albedo are then compared to the observations. In order to determine the effect of circulation more completely, the geometric albedo variations are computed as a function of the strength of the wind field. Further tests for our model are by comparison to the observed contrast of hemispheric brightness. This comparison tests our representation of the circulation by the induced variation in the haze layer. A future test is the wavelength dependence of the geometric albedo which is predicted by our model. Additionally, the spectral dependence of the reflectivity over latitude is a another source of predictions. These predictions

can be tested once Titan's disk is resolved and is observed over long periods of time. The latitudinal distribution of atmospheric reflectivity has been observed to be reversed between the IR and visible wavelengths (Caldwell *et al.* 1992). New observations in the IR and visible could come from with the Hubble Space Telescope (HST), other existing satellites, and the Cassini mission. UV observations may also come from these sources.

THE TWO DIMENSIONAL HAZE MODEL

The two dimensional model of the haze layer is a modified version of the model in Toon *et al.* (1992). The horizontal dimensions of the model are from the northern to southern poles and are covered by twenty equally spaced latitude points. The vertical dimensions are from the 0 to 300 km and are covered by forty equally spaced altitude points. The coordinate frame of the model is rectilinear, and does not take into account spheric effects which may be significant for Titan (Hourdin *et al.* 1991). The model's haze size distribution is described by 35 radii bins. The radius of the bin spans from 0.00013 to 3.0 μm. The size bin are evenly spaced by a factor of two in volume, v. At a given model grid point, the concentrations in the size bins, $n(v)$, are determined by numerically solving a couple series of number continuity equations,

$$\begin{aligned}\frac{\partial n(v)}{\partial t} &= \frac{\partial}{\partial z}(n(v)(w+v_s) - K_z n_a \frac{\partial (n(v)/n_a)}{\partial z}) + \frac{\partial}{\partial y}(n(v)v_y - K_y n_a \frac{\partial (n(v)/n_a)}{\partial y}) \\ &\quad + 0.5\int_0^v K(\nu, v-\nu)n(v-\nu)n(\nu)\,d\nu - \int_0^\infty K(\nu,v)n(v)n(\nu)\,d\nu \\ &\quad + q(v) - R_r n(v),\end{aligned} \tag{4.1}$$

where w is the vertical wind speed, v_s is the particle sedimentation velocity, K_z is the vertical eddy diffusion coefficient, v_y is the meridional wind speed, K_y is the vertical eddy diffusion rate, $q(v)$ is the production rate of particles,

and R_r is the rainout rate. The boundary conditions of the haze model are zero fluxes at top, and at the polar boundaries. Haze material is allowed to continuously flow out of the model at the surface. The time step of the solution depends on the maximum speed in the wind field and is determined by the Courant stability condition. For our calculations, the maximum time step was 0.1 years, and allowed a reasonable resolution of the seasonal variations. The solution method for the two dimensional continuity equation is described in Toon *et al.* (1988).

The major change between the above continuity equations and the analogous equations from the one dimensional model are the horizontal (i. e. meridional) transport terms which represent two processes; advection and eddy diffusion. The following discussion of the two dimensional model describes with the treatment of the transport processes, the haze microphysical processes, and the radiative transfer analysis.

The Haze Transport Processes. Haze transport is accomplished by the wind field which was derived in the preceding chapter and which is consistent with the present understanding of Titan's stratospheric circulation. The stratospheric circulation is represented by one cell which horizontally spans from the northern to southern poles and which vertically spans from 50 to 300 km. Atmospheric properties which are used to generate the wind field are the temperature, pressure, gravitational acceleration, and mean molecular weight. These quantities are averaged over Titan's stratosphere (see Chapter 3). The average of the atmospheric properties probably introduces errors into the wind field because vertical extent of the wind field is so large. To address the uncertainties, a parameter study is conducted by varying the strength of the wind field. The free parameter of our investigation is ξ and is the reciprocal of the product between the radiative time constant and the

frictional dissipation time constant. Instead of giving the value of ξ for each simulation, the maximum horizontal wind speed, v_y^{max}, at $\approx$ 110km will be given, because v_y^{max} has a more tangible meaning and is easier to use to test the consistency of the wind field with respect to theoretical estimates. The altitude of v_y^{max} is selected based on estimates for the altitude of unity optical depth at 0.55 μm (McKay *et al.* 1989 and Toon *et al.* 1992).

Our representation of the circulation has several simplifications which may be incorrect with respect to the actual circulation. It may be unrealistic to assume that one cell spans vertically the entire stratosphere. A better representation is possibly two cells which are vertically stacked. Additionally, the center of the wind field (i. e. the point which the circulation streamlines go around) may poorly represent the seasonal variation of the actual circulation because it is permanently fixed at the same location. In a more realistic circulation, the center of the wind field could move with the subsolar point. Another simplification in the wind field is the use of rectilinear coordinates, so spherical effects on the circulation are not considered. The wind field may be too weak at higher latitudes, because the convergence of mass flow at the poles is neglected. These and other elaborations are not done to the wind field because the representation of circulation is wished to be simple and physically plausible, so we can then easily interpert the effects of the circulation on the albedos. Despite the errors in our representation of the circulation, we have confidence that wind field is accurate enough for an initial estimate of circulation effects on Titan's geometric albedo, because the wind field matches the stratospheric circulation which is postulated (Flasar and Conrath 1990).

In the following simulations of the haze layer, eddy diffusion is small or insignificant by design. The justifications for this decision are because eddy

diffusion represents the transport by small scale motions within the atmosphere. In our model, the small scale motions are neglected, because their time scales are small compared to the other transport processes: sedimentation and large scale advection. Vertical eddy diffusion is nonzero in the troposphere of the model, because our wind field does not extend into this region. The tropospheric values of K_z are the same as the revised version of Toon *et al.* (1992) model. Above the troposphere, K_z exponentially decays by pressure scale height, for the sake of continuity. Despite the nonzero values of the eddy diffusion, haze transport in the troposphere is dominated by sedimentation. Hence, tropospheric circulation has little or no effect on the albedos in our simulations. For horizontal eddy diffusion, the values of K_y are set to zero throughout the model.

The Microphysical Processes. The haze model describes an aerosol layer which is produced at high altitudes by stratospheric photochemistry. The microphysical processes include sedimentation, coagulation, and rainout. The description and representation of these processes are the same as the one dimensional Titan haze model (Chapter 2). The parameters for the microphysical processes are set to values which were used in the revised version of the Toon *et al.* (1992) haze model. Consequently, rainout is zero and the haze layer extends to the surface. The haze production is included among the microphysical processes. Haze material is produced only in the smallest size bin as a particle of 1.3×10^{-7} cm in radius. The structure of haze production is assumed to be a gaussian with respect to altitude and is centered at 250 km. Other characteristics of production are the same as the one dimensional model. For the microphysical processes, the parameters do not vary over latitude.

The Radiative Transfer Analysis. The radiative properties of the simu-

lated haze layer are our observational tests of the model. The main tests are the simulations of the geometric albedo, P_λ, at 0.47 and 0.55 μm. Our simulations at these wavelengths attempt to reproduce the temporal variation of the observations (Lockwood 1986). The evaluation of P_λ must account for the latitudinal variation of haze opacity. In the one dimensional calculations, the irradances in P_λ were symmetric about the azimuthal angle of the observer. For a two dimensional model, azimuthal symmetry is obviously violated by any latitudinal variation in the haze layer. Accounting for latitudinal variation is complicated because the spin axis of Titan has an orientation with respect to the observer which is time dependent. We go back to the definition of the geometric albedo for a correct evaluation.

The geometric albedo is defined as the ratio of observed flux at zero phase (i. e. the sun, the observed object, and the observer are along the same line of sight) and the flux from a perfect lambert surface(Dlugach and Yanovitskij 1974),

$$P_\lambda = \frac{F_\lambda^o}{F_\lambda^L}. \tag{4.2}$$

In the case of Titan, a good approximation for the geometric albedo is that the observing angle and solar zenith angle, μ, are equal, because the Earth to Titan distance, Δ, is much larger the the radius of Titan, R. The expression for F_λ^o is

$$F_\lambda^o = \frac{R^2}{\Delta^2} \int_0^{2\pi} \int_0^1 I_\lambda(\tau = 0, \mu, \phi) \mu d\mu d\phi \tag{4.3}$$

where symmetry about the observer's azimuthal angle, ϕ, is not assumed to exist. The expression for F_λ^L is a well known result,

$$F_\lambda^L = \frac{F_\lambda R^2}{\Delta^2} \tag{4.4}$$

where F_λ is the solar constant. The definition of the geometric albedo is then

$$P_\lambda = \frac{1}{F_\lambda} \int_0^{2\pi} \int_0^1 I_\lambda(\tau = 0, \mu, \phi) \mu d\mu d\phi. \tag{4.5}$$

The integrals for P_λ are numerically evaluated. The gaussian quadrature was used to determine the μ integral

$$\frac{1}{F_\lambda}\int_0^{2\pi}\int_0^1 I_\lambda(\mu,\phi)\mu d\mu d\phi = \frac{1}{F_\lambda}\int_0^{2\pi}\sum_{i=1}^{N} w_i I_\lambda(\mu_i,\phi)d\phi \tag{4.6}$$

where w_i is the gaussian weight at the quadrature point μ_i. The ϕ integral was estimated by the trapezoidal rule

$$\frac{1}{F_\lambda}\int_0^{2\pi}\sum_{i=1}^{N} w_i I_\lambda(\mu_i,\phi)d\phi = \frac{1}{F_\lambda}\sum_{j=1}^{M}\sum_{i=1}^{N} w_i\alpha_j I_\lambda(\mu_i,\phi_j) \tag{4.7}$$

where

$$\begin{aligned}
\alpha_j &= \frac{\pi}{M} \quad for\ j = 1, M \\
\alpha_j &= \frac{2\pi}{M} \quad for\ j \neq 1, M \\
\phi_j &= \frac{2(j-1)\pi}{M-1}.
\end{aligned} \tag{4.8}$$

Monochromatic irradiances are calculated by the two stream source function method (Toon *et al.* 1989) as in the one dimensional model. These irradiances are indexed by planeocentric latitudes, ϕ', and longitudes, but the irradiance in equation 7 are indexed in the observer's frame. An operator, $\mathcal{F}$, is used to obtain the irradiances, I_λ, in equation 7

$$I_\lambda(\tau = 0, \mu, \phi) = \mathcal{F}(\mu, \phi, I'_\lambda). \tag{4.9}$$

$\mathcal{F}$ determines the the irradiance at the point (μ, ϕ) by extrapolating the planeocentric irradances, I'_λ, which have computed for the same value of μ.

The operator, $\mathcal{F}$, first determines the planeocentric location of the needed irradiance. This is accomplished by a reference transform (i. e. $(\mu,\phi) \longrightarrow (\mu',\phi')$). The transform of reference frames is two series of rotations. The initial series of rotations changes the observer's xyz axes to coordinate frame

which is centered on Titan. The first rotation of the initial series spins the yz plane of observer by 90° . The next rotation of the initial series spins the intermediate xy plane by 90° . The second series of rotations uses the frame at the end of the initial series, and it aligns the z axis to the spin axis of Titan. The first rotation of the second series spins the z axis about the y axis by the tilt of the spin axis, ϵ, ($\epsilon = 27°$ for Titan) We then rotate the intermediate z axis by the angle, Θ, which is between the spin axis and the observer's xy plane,

$$\Theta = \pi - \omega_s t \tag{4.10}$$

where ω_s is the angle frequency of Saturn, and t is time. An additional rotation could produce alignment to Titan's great meridian, This further rotation is not necessary for our calculations of P_λ , because I'_λ is zonally symmetric. The time dependence of Θ models the orientation of the spin axis and the procession of seasons on Titan. At $t = 0$, Θ corresponds to spring equinox in the northern hemisphere, so the northern hemisphere is rotating towards the observer. Once the reference frame transformation is accomplished, the planeocentric frame irradiances are extrapolated.

The temporal variation of P_λ can be explained by the latitudinal and temporal variations of atmospheric brightness, $B_\lambda(\phi', t)$,

$$B_\lambda(\phi', t) = I_\lambda(\tau = 0, \phi', \mu = 1) \tag{4.11}$$

where τ is the optical depth at wavelength λ. The normal relative albedo, $R_\lambda(\phi', t)$, can also be used to determine the sources of the P_λ variations and is defined as

$$R_\lambda(\phi', t) = \frac{B_\lambda(\phi', t)}{B_\lambda(\phi' = -40°, t)}. \tag{4.12}$$

R_λ is used instead of B_λ because it was used to display the observed hemispheric brightness contrast (Sromovsky *et al.* 1981). The R_λ versus latitude

is also used to determine if our simulation can reproduce the observed latitudinal distribution of the hemispheric brightness contrast.

The radiative properties of our simulations are also computed in the UV at 0.2225 and 0.35 μm, and in the IR at 0.888 and 1.075 μm. At the wavelengths in each spectral region, other sources of opacity combine with opacity from the haze and have significant effect on the P_λ and R_λ . In the UV, the Rayleigh scattering from atmospheric gasses is large enough to account for a few tenths of the first two optical depths. The Rayleigh scattering can then counter the albedo effect from absorption by haze particles, because Rayleigh scatterers are conservative and isotropic while haze particles are absorptive and forward scatterers at the UV wavelengths. At 0.888 μm, the roles of the haze and the other source of opacity are reversed. The scattering from haze particles offsets some absorption, because a strong absorption line from methane exists at 0.888 μm. At 1.075 μm, the surface albedo ($R_{sfc} = 0.1$) can have a significant effect on the albedo, because the haze layer is optically thin at 1.075 μm. At both IR wavelengths, the albedo effects are larger from the lower branch of the wind field (Two branches are in the wind field and have opposite directions of meridional winds, see Figure 3.1), because the unity optical depths occur deeper into the model atmosphere than in the visible and in the UV. The altitudes of the unity optical depths are lower, because the absorption by haze particles decreases for the longer wavelengths. Consequently, the temporal variations in the P_λ can change between wavelengths, because different regions of the atmosphere may determine the P_λ between wavelengths.

For all our radiative transfer calculations, the vertical distribution of atmospheric opacity is determined by the methods in the one dimensional model. The latitudinal and temporal variations of opacity are only produced

by the haze layer, because temperature, pressure, and composition are taken to be constant over latitude and time. The variation of nonhaze opacity will be discussed in a later section.

CALCULATIONS AND RESULTS

Method of the Calculations. The variations of the P_λ and R_λ were computed as a function of v_y^{max} through consecutive stages. The first stage computed the haze distributions for the smallest value of v_y^{max}. For our calculations, starting time was northern spring equinox and also corresponded to maximum upwelling in the northern hemisphere. The initial condition of the first stage was the haze distribution from the revised haze model of Toon *et al.* (1992). The haze distribution from this model was used at all latitudes. The two dimensional model was then integrated until the meridional cross-sections of the haze mass mixing ratio, the haze effective particle size, and the optical depths at 0.55 μm were over one year for Titan. The cyclicity test was a visual inspection of the isocontours for each haze quantity. For a more objective test for a cyclic solution, the values of two quantities had to be within 0.1%, when they were sampling times were separated by one year for Titan. The quantities for this test were the total mass of the haze layer, and the P_λ at 0.47 and 0.55 μm. Using the cyclic solution, v_y^{max} was increased and the model was integrated for a new solution. This process for the new solution was repeated for v_y^{max} values from 0.1 cm sec^{-1} to 1.5 cm sec^{-1}. We present the model results in the following manner. The P_λ and R_λ in the visible are displayed for the comparisons with the observations. The simulations of the UV and IR geometric albedos are shown for the v_y^{max} values which best reproduce the observations in the visible. The simulations of the UV and IR relative normal albedo are shown in later sections where the causes of the albedo variations are identified.

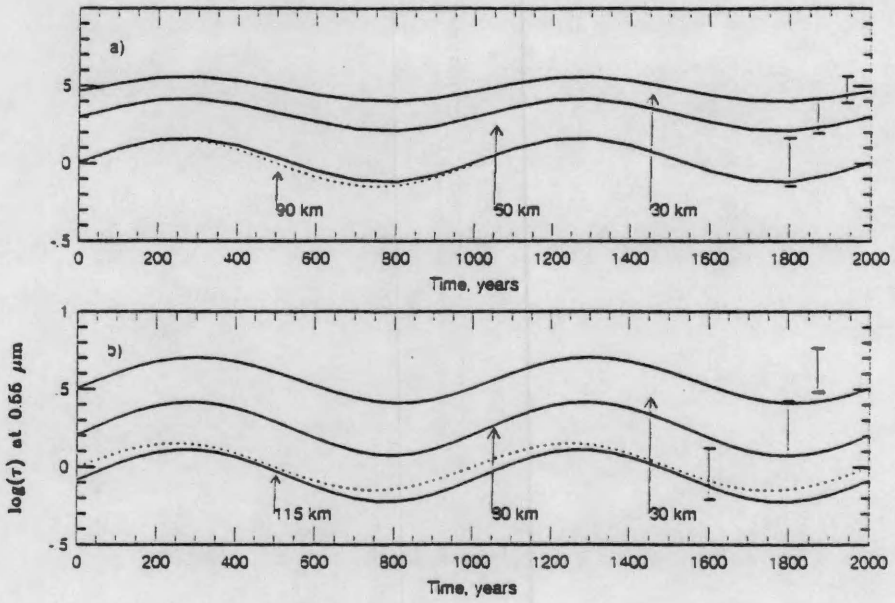
a)
5
0
-.5
90 km
50 km
30 km
0
200
400
600
800
1000
1200
1400
1600
1800
2000
Time, years
b)
1
.5
0
-.5
115 km
90 km
30 km
log(τ) at 0.55 μm
Time, years

Figure 2.4:

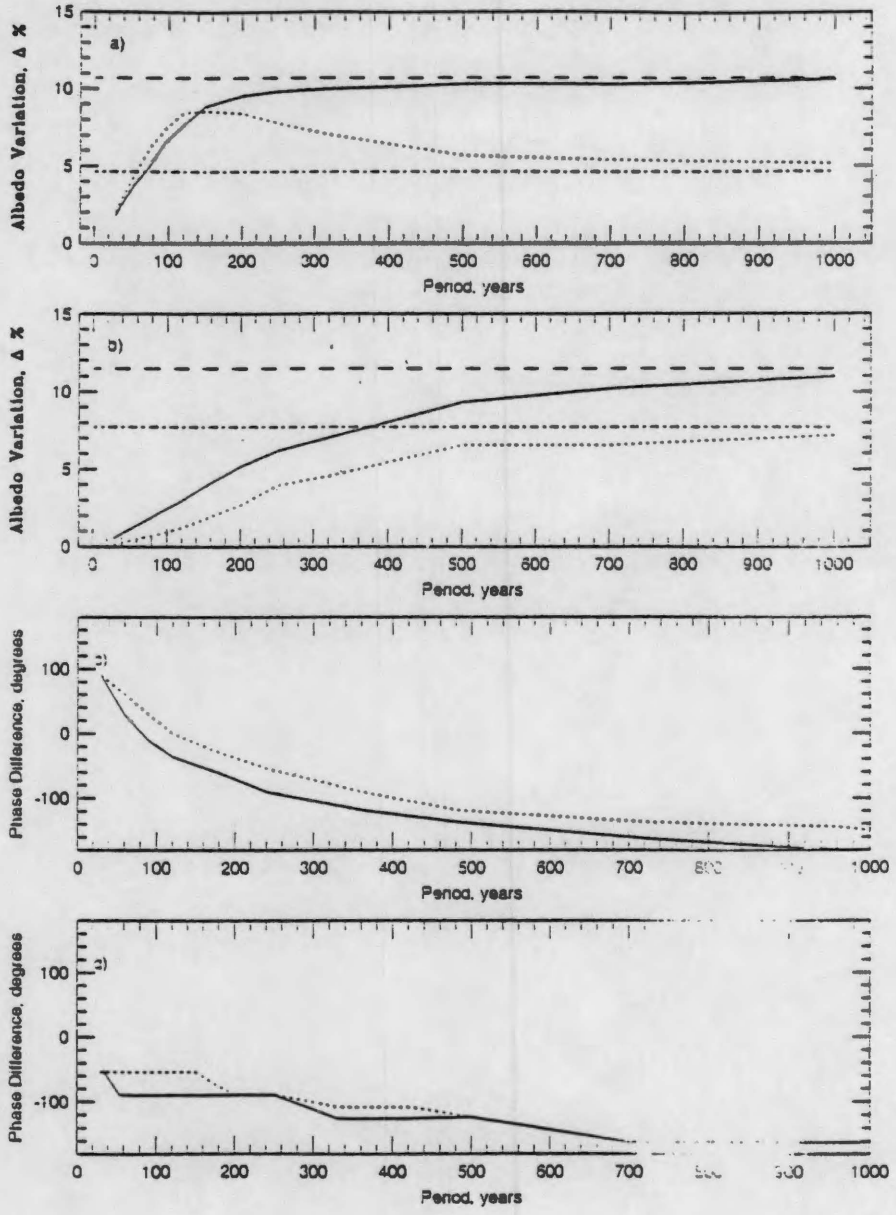
a)
Albedo Variation, Δ %
15
10
5
0
0
100
200
300
400
500
600
700
800
900
1000
Period, years
b)
Albedo Variation, Δ %
15
10
5
0
0
100
200
300
400
500
600
700
800
900
1000
Period, years
c)
Phase Difference, degrees
100
0
-100
0
100
200
300
400
500
600
700
1000
Period, years
d)
Phase Difference, degrees
100
0
-100
0
100
200
300
400
500
600
700
1000
Period, years

Figure 2.5:

Results of the Calculations. The variational amplitudes of the visible P_λ and the relative normal albedo for northern hemisphere, $\overline{R}_\lambda$.

$$\overline{R}_\lambda = \frac{2}{\pi}\int_0^{\pi/2} R_\lambda(\phi')d\phi'. \tag{4.13}$$

are presented as a function of v_y^{max} in Figure 4.2. The variational amplitude of each quantity is the fractional deviation from the annual average. Figure 4.2 shows that the variational amplitudes initially increase with respect to v_y^{max} and that the size of the observed P_λ variation is produced for $v_y^{max} \approx 1$ cm sec^{-1} (see Chapter 1). Such values of v_y^{max} are consistent to theoretical estimates of the wind speeds which v_y^{max} represents (Flasar and Conrath 1990). Our two dimensional model then appears able to produce the magnitude of the P_λ variation which was observed. Increasing of v_y^{max} does not indefinitely increase the amplitude of the P_λ variation, because the amplitudes start to decrease for v_y^{max} exceeding 1 cm sec^{-1}. The reversal of amplitude growth is discussed later.

In Figure 4.3, the temporal variations of the P_λ at 0.47 and 0.55 μm are shown for three values of v_y^{max}. The dotted curves represent the observed variation of the P_λ in the visible (Sromovsky *et al.* 1981). Our simulation of P_λ is shown to lag behind the observations by a significant phase. The phase is different between the observations and our simulations. because the seasonal variations of the circulation lag too far behind the seasonal variations of the solar forcing and because the haze layer does not instantaneously change from variation in the wind field. The following conclusion can be made, because the R_λ were observed to have a phase delay with respect to seasonal solar forcing; the delay is 90° in the observations. The 90° is then concluded to be partitioned between two response times. The first time is the period between the variation of the solar forcing and the response of the circulation. The second time is the period between the variation of the

circulation and the response of the haze layer. Each response time can be associated with a phase delay which sum to the observed 90° . To better agree with observations, our phase delay for the circulation should be decreased from 90 ° to 70° . This correction seems reasonable, because the P_λ over time, because the phase delay of our wind field has uncertainties which could be as large as 20° (Flasar and Conrath 1990).

Figure 4.4 shows the latitudinal profiles of the R_λ during Titan's seasonal cycle. The variations of R_λ are the largest in the polar regions which had the strongest lifting or sinking of haze material. Whether these R_λ variations match the observations is determined by a comparison to the hemispheric brightness contrast (Sromovsky *et al.* 1981). Figure 4.5 shows that the simulated R_λ at maximum hemispheric contrast does not match the observed R_λ when probably at maximum (Sromovsky *et al.* 1981). At maximum contrast, the observed R_λ exhibits a sharp change at the equator where the simulated R_λ is fairly constant. The observed hemispheric brightness is poorly reproduced, because the actual stratospheric circulation is not well represented by our wind field. We need to correct the representation of circulation. if we wish to prove that atmospheric circulation does produce the hemispheric brightness contrast. A more accurate circulation representation is later discussed.

The simulations of the P_λ in the UV and IR are shown in Figure 4.6 for the v_y^{max} values which best produce the observed variations of the P_λ in the visible. The temporal variations of P_λ in the IR and UV are 180° out of phase with respect to the visible. At 0.888 μm, the phase is expected because haze particles are mostly scatterers at 0.888 μm but are absorbers in the visible. The optical properties of the haze particle changes between the visible and 0.888 μm, because the absorption coefficient of the haze material decreases

with wavelength (Khare *et al.* 1984). The phase shift of P_λ at 0.888 μm also agrees with the observations. Since the Voyager fly-by, the Hubble Space Telescope has observed the R_λ at the visible and 0.888 μm. The variation of R_λ over latitude was opposite between 0.888 μm and the visible wavelengths (Caldwell *et al.* 1992). The phase shift of the P_λ in the UV is more difficult to explain, because the absorption coefficient of the haze increases from the visible to UV wavelengths. The phase reversals at UV and 1.075 μm are later discussed.

For the UV and IR, the variation in the P_λ also differs between the wavelengths within a spectral region. At 0.2225 μm, the P_λ variation is closer to a sine wave while the P_λ variation is a flatten sine wave at 0.35 μm. For the P_λ in the IR, a difference is more noticeable between the two wavelengths than for the two wavelengths of the UV. While the variation at 1.075 μm is a sine wave. the variation at 0.888 μm is irregular. For the amplitudes of the P_λ variations, the two wavelengths of the UV show a noticeable difference because the amplitude at 0.2225 μm is nearly four times larger than the amplitude at 0.35 μm. This is despite the fact that the haze absorption coefficient at 0.2225 μm is twice the haze absorption coefficient at 0.35 μm. The irregularities of the P_λ at 0.35 and 0.888 μm may be because each wavelength is in a transition zone between spectral regions. At 0.35 and 0.888 μm, the variations in the P_λ could then originate from combination of atmospheric regions which separately determine the P_λ variation at other wavelengths.

DISCUSSION

The Visible Albedo Variations. The following optical properties at 0.55 μm are examined to determine the source of R_λ variations in our simulations

and are for the first and second optical depths at 0.55 μm. We display the latitudinal distribution of each optical property. First, the altitudes are given for each optical depth along the effective radius of the haze particle at each altitude. The portion of each optical depth from the nonhaze opacity is given. We also display the single scattering albedo of the haze particles at each optical depth. We finally give the column averages of two scattering parameters between zero and one optical depths and between one and two optical depths. The column average of the asymmetry factor. g, is defined for a portion of the vertical column from a to b,

$$g(a,b) = \int_b^a \frac{\sigma_h(z)g_h(z) + \sigma_R(z)g_R}{\sigma_h(z) + \sigma_R(z)}\, dz \tag{4.14}$$

where σ_h is the scattering coefficient of the haze particles, σ_R is the Rayleigh scattering coefficient, g_h is the average asymmetry factor of the haze particles, and g_R is the Rayleigh scattering coefficient. The column average of the single scattering albedo. ϖ, which is determined for a portion of the vertical column,

$$\varpi(a,b) = \int_a^b \frac{\sigma(z)}{\sigma(z) + \kappa(z)}\, dz \tag{4.15}$$

where $\sigma(z)$ is the total scattering coefficient at z and $\kappa(z)$ is the total absorption coefficient at z.

When large differences in the R_λ were produced between the northern and southern hemisphere, the above optical properties exhibit large variations in the polar regions where R_λ has a large gradient (Figure 4.7). (In Figure 4.7, the top six panels are for the optical properties in the first optical. In the left column, the three panels are in descending order: the altitude of the optical depth, the fraction of the optical depth from atmospheric gasses, and the column average of the single scattering albedo in the optical depth. In the right column, the three panels are in descending order: the effective radius of the haze particles at the optical depth, the single scattering albedo

of the haze particles at the optical depth, and the column average of the asymmetry factor in the optical depth. The bottom six panels are for the optical properties in the second optical depth. In these six panels, the information is in the same order as the top six panels.) We conclude from the figures that the variations of single scattering albedos at the unity optical depths are the source of the variations of the R_λ and P_λ in the visible. In the visible, the single scattering albedos at the unity optical depths are solely determined by the haze layer, because the haze particles are the only significant source of extinction. Consequently, the changes of effective particle sizes explain the variations of the single scattering albedos which are located at the unity optical depths. For example, darkening of a hemisphere occurs when the single scattering albedos are lowered by an increase of particle size. The amount of absorption is then increased and the hemisphere darkens. In the brighter hemisphere, the opposite change of particle sizes takes place and less absorption occurs.

The wind field affects the distribution of the haze opacity in two ways. In both cases, the upper branch of the wind field produces the changes in the R_λ , because optical depths are too large at the lower branch for those particles to affect the R_λ . The first way in which the circulation effects the R_λ is that the horizontal winds move the upper portions of the haze layer from one hemisphere to the other hemisphere. When the upper portion of the haze layer is pushed out of a region, the unity optical depths descend into the atmosphere, and more absorption is produced, because the haze particles are larger at the lower altitudes. If horizontal winds push upper haze material over a region, the unity optical depths now take place at higher altitudes. More radiation is outwardly scattered, because smaller particles compose the upper portion of the haze layer. (Smaller particles of the haze produce more isotropic and conservative scattering than larger particles.) The upper

portion of the haze is push out of the upwelling hemisphere, while the upper portions are pushed over into the downwelling hemisphere. The second way in which circulation effects the R_λ is vertical transport of haze material. Vertical winds can alter the vertical distribution of particle sizes; this distribution is strongly influenced by the sedimentation rates of each particle size. When the vertical winds lift larger particles to the unity optical depths, the decrease of the single scattering albedo produces hemispheric darkening. Conversely, if vertical winds move smaller particles to lower altitudes, the single scattering albedos increase at unity optical depth, and hemispheric brightening is produced.

These albedo effects from the wind field are complementary, because the two mechanisms concurrently produce brightening or darkening. The relationship between the two mechanisms is symbiotic, so the regions of convergence or divergence have the largest effects on the albedo. Darkening is produced when haze material was vertically pumped up and then horizontally dispersed from a region. Brightening is produced when material is vertically pumped down and then horizontally removed from a region. For the wind field, such patterns of haze movement are strongest in the polar regions. For the polar region of a given hemisphere, the specific pattern of material movement varies over the seasons, so the polar regions periodically alter the size distribution about a state which would be produced from the sedimentation. This periodic variation significantly affects the albedo when the time scales of advection are comparable to sedimentation time scales. When the advection times become lower than the sedimentation times, albedo variations from the circulation become limited, because the wind field starts to dominate the removal of the haze from the atmosphere which was previously dominated by sedimentation.

Some inferences can be made on the actual circulation based on our simulations and the observations of the hemispheric brightness contrast (Figure 4.5). Our results imply that observed sharp gradient of R_λ is produced by convergence or divergence near the equator. Our wind field should have had vertical winds which were stronger near the equator. Our representation of the circulation could be corrected if the center of the wind is moved to the south. This correction produces further agreement with the observations because the simulations of R_λ would be uniform in the the mid latitudes of the southern hemisphere. Interestingly, the observations were taken when the circulation should be responding to summer solstice in the southern hemisphere. The subsolar point is at -27° under these conditions. Our correction places the center of the wind field at this location. Therefore, our representation of the circulation could overall improve if the center of the wind field follows the seasonal movement of the subsolar point.

In Figure 4.2, the amplitude of the P_λ variation decreases for $v_y^{max} > 1$ cm sec-1. This reversal of amplitude growth has to be from a decrease of the above variations in the haze layer. This could be because higher wind speeds more efficiently remove haze material from the model. The effect would also selectly remove larger particles, because their sedimentation rates are greater. This deduction was made by comparing the one dimensional model results for P_λ versus λ (McKay *et al.* 1989 and Toon *et al.* 1992) and the two dimensional model results for the annual average of P_λ versus λ (Figure 4.8). The one dimensional and two dimensional models show similar changes of the spectral dependence of P_λ when the one dimensional model's mass production rate decreases and when the two dimensional model's v_y^{max} increases. For the one dimensional haze model, this change of P_λ versus λ is caused by decreasing the haze column density. Hence, increasing v_y^{max} decreases the annual average of the haze column densities. This relationship

is possibly because hemispheric downwelling increases haze sedimentation from the atmosphere more than the upwelling hemisphere can compensate. The variational amplitude of the P_λ eventually reaches a maximum and then decreases because continued decreases of the haze column densities reaches a critical point where the seasonal variation of haze opacities is less than for a lower value of v_y^{max}, so the variation of P_λ decreases. This critical point is reached when the transport times for the vertical wind and particle sedimentation are equal.

The UV Albedo Variations. To identify the sources of the P_λ variations in the UV, the same technique is used as in the visible. The R_λ versus ϕ' are first examined so we can locate the regions where largest variations of R_λ occur. We then examine several optical quantities which could cause these R_λ changes. The R_λ in the UV has largest variations between -60° and 60° (Figure 4.9). These variation of R_λ cause one hemisphere to be brighter at a given time or season. For the time of the largest difference of R_λ between hemispheres, the optical quantities vary at the same latitudes (Figures 4.10 and 4.11). The single scattering albedos also vary at these latitudes but the explanation for the R_λ variations in the visible does not satisfactorily explain the R_λ variations in the UV. The temporal variations of the single scattering albedo seem to be smaller than needed, especially at 0.35 μm. At 0.35 μm, the variation of the single scattering albedos may be small because the single scattering albedos of the haze particles vary to produce produce the opposite effects on the brightness than in our simulation (Figure 4.11). At 0.2225 μm, the single scattering albedos of the haze do not have a variation which is conflicting as at 0.35 μm, The reason is possibly that the haze absorption coefficient and the Mie size parameters are higher at 0.2225 μm (Hassen and Travis 1974, and Khare *et al.* 1984).

To explain the UV R_λ variations, the column average of asymmetry factor, $g(a,b)$, is needed. The latitudinal variation of g is most noticeable between the first and second optical depths. A hemisphere is brightened by more back scattering when g decreases between 0 and $\pm$ 60° . Darkening of a hemisphere takes place when g increases. More radiation is scattered down into the atmosphere and absorbed. At 0.35 μm, the variation of g is the source of the R_λ variations.

Further calculations verify that the variations of g are the source the R_λ variations at 0.35 μm. In these calculations, g or the single scattering albedo is held constant over time. Figure 4.12 shows the recalculations of the P_λ . When the g at 0.35 μm is constant, the variation of P_λ is 180° out of phase with respect to original simulation of the P_λ at 0.35 μm. This change of phase does not occur when g varies and the single scattering albedo is constant. Hence, the variations of g are the source of the variations in the P_λ and R_λ at 0.35 μm because its variations produce the same phase of P_λ variations as in the original simulations.

For the original simulation of the P_λ at 0.35 μm, the irregular variation may be caused by the variations of the single scattering albedo. This conclusion is based on the P_λ simulation with a constant g at 0.35 μm. This P_λ simulation had an opposite phase with respect to the original simulation. The variation of the single scattering albedo could then diminish the effects on the albedo from the variation of g. Hence, the variation of the P_λ would be diminished and would not be a sine wave when both the single scattering albedo and g vary over time and space.

At 0.2225 μm, we perform similar calculations so we could determine the contribution of g in the variation of P_λ . The single scattering albedo may have a larger contribution in the P_λ variations at 0.2225 μm. because

the variational amplitude of the P_λ was slightly larger for a constant g. The confidence of this conclusion is weakened because the constant values used for g and the single scattering albedo in our additional calculations.

Rayleigh scattering has greater effects on the albedos in the UV than in the visible. This is caused by the higher optical depths from Rayleigh scattering so Rayleigh scattering counter acts the optical effects from the haze particles. In particular, the isotropic property of Rayleigh scattering is important in the variations of R_λ , because it offsets the g of the haze particles which are highly forward scattering. Rayleigh scattering is especially important at 0.35 μm, because the variation of g determines the P_λ variations at 0.35 μm. In Figures 4.10 and 4.11, further evidence can be seen that extinction from Rayleigh scattering is higher in the UV than in the visible. For example, the values of the ϖ and g exhibit the changes which caused the variations in the P_λ and R_λ , because the two quantities include both the opacity from the haze particles and from Rayleigh scattering of the atmospheric gasses. Additionally, the source of the R_λ variations is more noticeably located between the first and second optical depths, because the densities of the atmospheric gasses are higher between the first and second optical depths.

A different region in the wind field causes the R_λ variation in the UV than in the visible. These regions are where haze transport is mostly horizontal so the variations in the haze layer are important at constant altitudes. Such variations are significant because the background opacity, atmospheric density, has no latitudinal variations. The circulation then varies the ratio of absorption to scattering by changing the mixing ratio of haze mass. The upper levels in the upwelling hemisphere produce hemispheric brightening when the horizontal winds reduce haze densities which are from 0 to $\pm 60°$, so the

amount of Rayleigh scattering increases. Hemispheric darkening is produced by the addition of haze particles to the mid latitudes of a hemisphere, and occurs in the upper levels of the downwelling hemisphere.

We can estimate if our conclusion is sensitive to the assumed distribution of atmospheric density and our representation of the circulation. If the seasonal variations of density are ten percent or more, the Rayleigh optical depths have large variations over latitude, and our conclusion may be in error, but variations of density are unlikely to be this large. Our conclusions are more dependent upon our representation of the circulation. The variation of P_λ can change in our simulations. if the actual circulation has several regions where haze material divergences or convergences. Such changes in our wind field redistribute the regions where the wind vectors are mostly along the meridion. Nevertheless, we still believe that our conclusions can be used to predict the P_λ variations from an atmospheric circulation which is more sophisticated than used.

The 0.888 μm Albedo Variations. Difficulties are encountered when identifying the source of the P_λ variations at 0.888 μm. Our previous method is difficult to use for two reasons. First, it is uncertain when to look for the source of the 0.888 μm P_λ variations because the P_λ at 0.888 μm has odd intervals while at maximum (Figure 4.8). Our approach to this problem is to examine the R_λ at four times which are evenly spaced over the seasonal cycle of P_λ . Our previous method is also complicated because at any time the values of R_λ has a large range. The variations of R_λ may be large in a given area but their location and spatial extent can produce a small weighted contribution to the P_λ . Consequently, it is difficult to determine the source of the P_λ variation. We attempt to address this problem by plotting the R_λ vs $\sin(\phi')$. Figure 4.13 displays the R_λ latitudinal profiles from our modified

method.

Several regions can be seen to be the source of the P_λ variations. In the either hemisphere, the polar region ($|\sin\phi'| = 0.866$ to 1.0) and the mid latitude region ($|\sin\phi'| = 0.0$ to 0.866) are the best candidates. These regions have opposite variations of R_λ over time. For example, the R_λ in the polar region undergoes a minimum between a hemisphere's spring equinox and summer solstice while the R_λ in the mid latitude region are undergoing a maximum, The effect on P_λ from one region is dominant, because the R_λ variations in the two regions are 180° out of temporal phase. The dominant values of R_λ are selected by two constraints. At 0.888 μm, the dominant values of R_λ should have the same temporal variations as P_λ . The second constraint is that the location and spatial extent of the R_λ variations should be weighted to have a larger effect on P_λ . The weights of the R_λ values are determined by observing geometry. The mid-latitudes only satisfy both constraints on R_λ .

The cause of the R_λ variations is from the variation of the ϖ. A hemisphere is brightened by an increase of the ϖ, while darkening is produced by the opposite changes of the ϖ (Figures 4.14 and 4.15). These variations of ϖ are produced by the fraction of an optical depth from methane (Figures 4.14 and 4.15). and are related to the variations of the mixing ratio of haze mass. The variations of mixing ratio are most noticeable around the first optical depth (Figures 4.14 and f4.15). When the mixing ratio of haze material is at a annual maximum, the values of ϖ reach a seasonal high, because the haze particles produce most of the scattering at 0.888 μm while most of the absorption is from methane. The periodic variation of a mixing ratio is both the source of the P_λ variation in the UV and at 0.888 μm, but the R_λ at 0.888 μm has an opposite relation to higher haze densities than in the

UV. It is then difficult to understand how the wind field can simultaneously produce these relations to haze density.

The solution is because the unity optical depths of each wavelength occur at different altitudes (Figures 4.10, 4.11, 4.14 and 4.15). In the UV, the unity optical depths occur at higher altitudes. Meridional winds are higher at these altitudes. The greater winds can move haze material across the equator before the meridional winds seasonally reverse. The changes of the UV opacity are then produced by interhemispheric transport of the haze. At 0.888 μm, the unity optical depths occur at lower altitudes but are still in the upper branch of the wind field. The transport is slower at these altitudes The seasonal reversal of wind direction takes place before the material can be moved across the equator, so the movement of haze material is more confined within a hemisphere. The opacity changes at 0.888 μm are then produced by the haze material moving between the polar and lower latitudes of a hemisphere. Hemispheric brightening is produced when polar haze material is spread over the mid-latitudes. This movement of haze material occurs in the upwelling hemisphere. Conversely, darkening occurs in the hemisphere which is downwelling.

The altitudes of the unity optical depths at 0.888 μm can also explain the irregular variation in the P_λ . These altitudes are close to where the meridional wind reverses direction between the upper and lower branches of the wind field. Consequently, the variations in the haze mixing are not the same along a vertical column at a given time, so the haze mixing ratios oscillate over altitude as well as time. The R_λ variations are reduced with respect a variation of the mixing ratios which only increased or decreased over time, because the higher scattering at one altitude can be balanced by higher absorption at a different altitude. These opposing effects on R_λ are

also not in temporal phase, because meridional winds vary over the altitude. Consequently, the P_λ at 0.888 μm has an irregular variation over time.

Our conclusions for the R_λ at 0.888 μm could change if the methane mixing ratio varies over latitude or season. Such variation of methane are considered small for three reasons. Large variation of methane can be produced by the condensation of methane when the temperature varies over latitude. The methane variations from condensation are probably small, because the temperatures of the stratosphere should not produce large amounts of condensation. Methane abundance of the stratosphere can also vary from the variations in the tropospheric temperatures, because the troposphere is the source of the methane in the stratosphere. The variations of tropospheric temperature are also believed to be small over latitude and season. The final reason is that the photochemical lifetime of methane is long with respect to Titan's year. Hence, seasonal variations are expected to be small for methane from photochemical destruction. The destruction of methane does vary over latitude because the solar flux varies over latitude. This latitudinal variation of methane is not believed to be large.

An uncertainity in our conclusions at 0.888 μm is from the altitudes of the unity optical depths. The speeds of the wind field are relatively low at these altitudes. Eddy diffusion may compete with advection. The haze variations in our simulations could be diminished to a great extent if the coefficients eddy diffusion are much higher than 10^6 cm^2 sec^{-1}. This problem is more apparent at 1.075 μm, because the unity optical depths at 1.075 μm occur at altitudes which are lower than for 0.888 μm.

The 1.075 μm Albedo Variations. At this wavelength, the variations in the P_λ are produced by the temporal variations of R_λ in the mid latitude region, -60° to 60° (Figure 4.16). The two apparent causes of the R_λ variations

are from the variations in total optical depth and from the variations of the g in the first optical depth (Figures 4.17 and 4.18). A hemisphere brightens when total optical depths are minimum in the mid latitude region and when the values of g is a maximum in the first optical depth. Hemispheric brightening is then a product of two processes which simultaneously increase. First, the transmission of downward irradiance increases, because the absorption from the haze particles decrease, so more radiation is reflected by the surface. Second, the transmission of upward irradiance increases, because the g in the first optical depths increases, so haze particles more outwardly scatter radiation from the surface. The opposite is true for hemispheric darkening. Therefore, the bright surface is seasonally covered then uncovered by the haze layer and a transmission of the reflected radiation is seasonally increases and decreases.

Further calculations illustrate that the R_{sfc} strongly determines the P_λ variation at 1.075 μm. The P_λ at 1.075 μm was recalculated for two different values of R_{sfc}, 0.01 and 0.95 (Figure 4.19). The amplitude of P_λ is shown to be directly related to the value of the surface albedo. We conclude that the seasonal exposing of the surface causes the P_λ variations for two reasons. If the polar variations of opacity were responsible for the simulated P_λ , the value of R_{sfc} would not have any effect in simulations, because the optical depths are too large at the poles (Figure 4.17). Additionally if the P_λ was totally independent of the value of R_{sfc}, the sine oscillation of P_λ should be independent of R_{sfc}. This is not true when R_{sfc} varies from high to low values (Figure 4.19).

Variations of the total haze column density produces the P_λ variations at 1.075 μm, because the absorption coefficient of haze is very small at 1.075 μm and because there are no sources of atmospheric opacity at 1.075 μm.

Hemispheric brightening is produced by decreases of haze column densities while increases of column densities are produce hemispheric darkening. The R_λ values of the mid latitudes are then inversely related to the amount of haze material which is present. At 1.075 μm, the source of the P_λ variation seemingly conflicts with the source of the 0.888 μm P_λ variation because the R_λ variations at 0.888 μm are produced by increases of haze material from advection.

The above discrepancy is removed by considering the altitudes of the unity optical depths. The 1.075 μm optical depths are at lower altitudes than for 0.888 μm (Figures 4.14, 4.15. and 4.20). The unity optical depths at 1.075 μm are totally in the lower branch of the wind field where the advection of haze material is in the opposite direction with respect to the upper level. The unity optical depths at 0.888 μm occur in the upper levels of the wind field. Therefore, 1.075 μm hemisphere brightening is produced when haze material in the mid latitudes is swept to the pole of the same hemisphere. When haze material is swept to the mid latitudes from the pole, hemispheric darkening occurs at 1.075 μm. The brightening is a product of hemispheric upwelling, while the darkening is from hemispheric downwelling.

SUMMARY

A two dimensional model of Titan's stratospheric haze has been constructed to determine the effects on Titan's albedo from atmospheric circulation. The radiative or brightness effects are from the variations in the haze layer which are induced by the circulation. The circulation was represented by a wind field for a pole to pole cell. Our representation of the circulation also contains seasonal variations which are simulated by oscillating the

wind speeds. The period of the oscillation is one year for Titan. Our representation of the circulation is roughly consistent the present understanding of Titan's stratospheric circulation (Flasar *et al.* 1981, Flasar and Conrath 1990, and Flasar *et al.* 1991). To conduct the investigation, the brightness variations were computed for different strengths of the wind field. In the visible wavelengths, the goal of calculation is to reproduce the observations of the geometric albedo over time (Lockwood 1986) and the observations of the hemisphere brightness contrast (Sromovsky *et al.* 1981). The geometric albedos in the UV and IR are also computed for further effects on the haze layer from the circulation.

The following conclusions are made from the investigation.

- For the variation of the geometric albedo in the visible:

    1. Our simulations produce the amplitude of the observed variations. when the meridional wind speed at unity optical depth is approximately 1 cm sec^{-1}. Such wind speeds are consistent with the knowledge of Titan's stratospheric circulation.

    2. The temporal variations in our simulations match the observations of the visible geometric albedo if the season variations of the circulation is 70° behind seasonal solar forcing. This phase lag of the wind field is consistent to previous work on Titan's circulation (Flasar *et al.* 1990). In our simulations, the value of the phase delay is also consistent with the observations of hemispheric brightness over time. The phase delay of the hemispheric brightness variations is to be observed 90° (Sromovsky *et al.* 1981 and Caldwell *et al.* 1992). We conclude that this phase delay is partitioned between the response times of the circulation and the haze

layer.

3. The variations of the geometric albedo are caused by large variations of atmospheric reflectivity in the polar regions where haze material upwells or downwells. The transport of haze material seasonally varies the effective radius of haze particle at unity optical depth, so the single scattering albedo of the haze particles changes at unity optical depth and the reflectivity of the atmosphere alters as a result.

- For the hemispheric brightness contrast:

  1. When atmospheric reflectivity is averaged over a hemisphere, our simulations agree with the observations.
  2. In our simulations, the reflectivity did not vary over latitude as in the observations of the hemispheric brightness, because the observed reflectivity sharply changes in the equatorial regions. Our model instead produced large variations in the polar regions.
  3. The disagreements between the observations and our simulations is because our representation of Titan's circulation is not accurate. Our simulation suggest that the center of the wind field to follow the subsolar point. We did not incorporate this characteristic into our wind field.

- For the UV and IR albedos,

  1. At the strengths of the wind field reproducing the temporal variations of the visible geometric albedo, the geometric albedos in the UV and IR should vary approximately 180° out of temporal phase with respect to the visible.

2. In the UV and the IR, the variations of the geometric albedo are caused by the variations of atmospheric reflectivity in the mid latitudes, -60° to 60° . The variations of reflectivity are produced by strong horizontal winds, because the horizontal advection alters the haze mixing ratios at constant altitudes. Consequently, the amount of haze opacity varies in the unity optical depths.

3. In the IR and UV, our predictions for the variation in the P_λ are more tentative than in the visible, because the variations of atmospheric reflectivity are more complexly related the representation of the circulation.

It is reasonable to ask whether our simulations of the geometric are relevant if the circulation of Titan's atmosphere is very different than the wind field in our simulations of the geometric albedo. We believe that our simulations will be useful to understand or to explain the variations in the geometric albedo from a more accurate representation of the circulation. At 0.25, 0.47, and 0.55 μm. we are the most confident that our simulations of the reflectivity can be used to predict the effects on the geometric albedo from the circulation, because the geometric albedo was determined by one region in the wind field. At 0.35 and 0.888 μm, our simulations should be applied with caution, because the geometric albedos at these wavelengths are determined by several regions in the wind field, or because the single scattering albedo and the asymmetry factor produced opposing effects on the geometric albedo. In the IR, an application of our simulations may be unreliable, because our simulations did not include eddy diffusion. In the IR, the unity optical depths occur at altitudes where the wind speeds of the general circulation may be small with respect to atmospheric eddies. If eddy diffusion is comparable to advection at these altitudes, our simulations

of the haze variations may over estimate the transport of haze material by advection. Consequently, the potential variation of geometric albedo from the general circulation could be over evaluated in our simulations.

Chapter 5

Conclusions

INTRODUCTION

We have investigated two sources which could explain two brightness observations of the Titan; the hemispheric brightness contrast, and the variations of the geometric albedo in the visible. Both observations are explained by reflectivity variations which are over latitude and season. The haze layer of Titan's atmosphere is believed to produce the reflectivity variations, because it is optically thick in the visible and is global in extent. Both sources in our studies produce variations in the haze layer so they could affect the reflectivity. The first source was the seasonal variations in haze production, because the production of the haze is partially driven by the solar flux. The solar flux varies over latitude and season, because the spin axis has a tilt of 27° . We were then motivatived to determine the variations in the geometric albedo when the production rate of haze mass varied over season. The investigation of the production effect just determined the seasonal variations in the geometric albedo. The second source in our study was the seasonal

variations of circulation, because the distribution of the haze layer is influenced by the advection from circulation. There should be seasonal variations in the circulation effect on the haze layer, because the radiative and dynamic time constants of the stratosphere are small with respect to one year for Titan. Our investigation of the circulation effect was for the seasonal variations in the geometric albedo and for the seasonal and latitudinal variations in atmospheric reflectivity.

The investigation for production variation was conducted with an aerosol model which was one dimensional. The aerosol model for our study was previously used to determine the haze structure under steady state conditions. The existing model was adapted for our purposes by varying the production rate of the haze mass over time. The aerosol model had no other quantities that varied over time.

A two dimensional model was used to determine the effect on the reflectivity from circulation. We had to construct a two dimensional model for our purposes, because there were no existing two dimensional models of the haze layer. The first step of this construction was to expand the existing model from one to two dimensions. The dimensional expansion was accomplished by existing techniques, so new numerical methods did not have to be derived. The second step of construction was to obtain a circulation which would induce the variations of the haze. We derived a wind field to accomplished this step. Our wind field satisfied a simple understanding of the circulation which occurs in Titan's stratosphere.

The remainder of this chapter reviews the results and conclusions from the examinations. The following section will review the investigation of production. The third section will give the results from the investigation of circulation. The final section will conclude which source is most likely source

of the observations. Reservations in our investigations will also be discussed. Possible improvements are suggested for the further investigations of the better source of the observations. Additional uses of the two dimensional haze model are discussed.

PRODUCTION INVESTIGATION

Two versions of the Toon *et al.* (1992) haze model were used to determine the effects on the albedos from varying production. The versions were essentially different in the parameters for the haze microphysics. and the transport processes. The parameters in the conventional version were determined by previous studies of Titan's atmosphere. The parameters in the revised version were determined by fitting to the observations of the geometric albedo (Neff *et al.* 1984). The parameters between the two versions produced differences in the vertical distribution of particle densities and sizes. The particle sizes in the revised version were larger at higher altitudes, but the particle sizes were still smaller than in the conventional version. The distribution of haze density varied the opacity structure between the two versions of the model. In the revised version, haze densities reached maximum values at high altitudes and were more uniform over altitude than in the conventional version. Consequently, the unity optical depths were at higher altitudes in the revised version.

In our simulations, the variation in the production rate was assumed to be directly related to the solar flux, so production rate varied as the seasonal solar forcing. For the phase of the production variation over time, the variations of the production rate were assumed in phase with seasonal variations of solar forcing, so the production rate was maximum at spring equinox.

The column production rate of haze mass was the only aspect of production which varied over time. We did not change the vertical distribution of haze production or the size distribution of haze production with respect to the origin haze model (Toon *et al.* 1992). It should be noted that our simulation of production variation was somewhat arbitrary, because the seasonal variations in haze production are not well determined.

Seasonal variations of production failed to produce the observations in two ways. First, the simulations of the geometric albedo produced an amplitude of variation which was small with respect to the observations (Lockwood *et al.* 1986). Second, our simulations of the geometric albedo were out of temporal phase with respect to the observations of the geometric albedo. We attempted to solve these problem by increasing the variation of the production rate and by changing oscillation of the production rate over time. Both these attempts failed. Either the geometric albedo varied by an amplitude which was too small or the values of geometric albedo were inconsistent to the observations.

The time scales of the haze layer were seen as the source of the failure. The time scales were for the lifetimes of particles near the unity optical depths, because these particles determined the geometric albedo. The failure of production were explained by using an analogy to a driven and damped harmonic oscillator. When the frequency of the forcing is much higher than the resonance frequency, the oscillator has a smaller amplitude of response than expected for a constant forcing. For applying our analogy, the oscillator is the haze layer and has a resonance frequency which is the reciprocal of the lifetime of a haze particle at the unity optical depths. The response of the oscillator is the variation of the reflectivity in the visible. The production rate is the forcing on the oscillator. The forcing can also be considered from the

solar flux, because the production rate and solar flux were assumed directly related. The driving frequency in the forcing is inversely proportional to one year for Titan (29.5 years). Therefore, the variation of the geometric albedo was small because the period of the forcing was much smaller than the residence time of the haze particles which determine the geometric albedo in the visible. the particle lifetimes are much larger than the period of the forcing. Our analogy predicts that the response of the reflectivity is out phase with respect to the solar forcing. A delayed response or phase delay with respect to the solar forcing was produced in our simulations of the geometric albedo. The size of phase delay can match the observations. The success seemed unimportant because the amplitude of the observed variations was not produced by our simulations.

We attempted to increase the albedo variation in our simulations by changing the parameters of the aerosol model, because the parameters controlled the particle lifetimes. When the particle lifetimes were decreased, the variation of the geometric albedo should increase. if our analogy to a driven oscillator is correct. The amplitude of the observed variations was produced when the rainout of the haze was raised to 90 km. This improvement was considered unsatisfactory for two reasons. The temporal variation of the geometric albedo was still incorrect because of its phase. Second, the higher boundary of rainout was unrealistic, because the stratosphere of Titan would have rainout processes which have characteristics of tropospheric rainout.

The failure of the production source provoked a discussion of other sources for the observed variations. An alternative source was a different aspect of production. The changes in the haze composition could alter the geometric albedo because the absorption coefficient of haze material is determined by the composition. This alternative source was considered too

difficult to investigate, because photochemical models of Titan can not predict composition of the haze material. Another source was circulation and it influences the distribution of the haze layer. Seasonal variations of circulation were considered a likely source, by using two previous studies. The first study dealt with the atmospheric circulation and its variations over seasons. The second study dealt with the effects on the albedo from circulation. The conclusions in the two studies were used to construct a scenario which could explain the observations. A two dimensional model would have to verify our scenario and show that variations of circulation could produce the observations. We concluded that this was the source to examine.

CIRCULATION INVESTIGATION

Two components were in the model which evaluated the albedo effects from circulation. The first component was an aerosol model. This component included the microphysical and transport processes. The description of these processes was the same as the model which was used for the production investigation. Parameters in the aerosol model were similar to the revised version of the existing model. The parameters in the aerosol model did not vary over latitude. The second component was the circulation and varied the haze layer over latitude and season. A pole to pole cell was used to represent the circulation. The wind field of our circulation had a variable strength which was measured by the meridional wind at $\simeq$ 110 km. The wind field was made time varying by multiplying its wind vectors with a sine wave. The temporal variation of our wind field were one season (90° of phase) behind the variation in the solar forcing, so the seasonal variations of our circulation were consistent to theory. We believed that our representation was reliable enough for an initial estimation of the effects from the circulation on the reflectivity

and the geometric albedo, despite the simplifications in our representation of the circulation.

The variation of the geometric albedo was calculated for different strengths of our wind field. The amplitudes of variation matched the observations in the visible when the strength of the wind field was approximately 1 cm sec^{-1}. Such values of the meridional wind at $\simeq$ 110 km are consistent to theory. The variation of geometric albedo had the correct spectral dependence in the visible, because the amplitude of the variation was inversely related to the wavelength. The temporal variation of the geometric albedo in the visible was nearly correct with respect to the observations. The seasonal variation of our circulation should had been 70° behind the seasonal solar forcing for better agreement with the observations, because a significant amount of time occurred between the seasonal variations in the wind field and the haze variations. (Haze variations affected the reflectivity and the geometric albedo.) The observed phase delay of reflectivity to the solar forcing (Sromovsky *et al.* 1981) is then partitioned between the response times from the circulation and the haze layer.

Our representation of the circulation was tested by the variation of reflectivity over latitude. The test was the reproduction of the hemispheric brightness contrast which was observed during the Voyager fly-bys. The test was not passed, because the reflectivity in our simulations did not produce sharp change near equator as was observed. Our representation of the circulation was concluded to be inaccurate. A possible correction was to move the center of the wind field with the subsolar point. This correction was based where the reflectivity sharply changed in our simulations. This location was where haze material was upwelled or downwelled from our wind field. The implication is that vertical winds of the equatorial region are stronger than

in our wind field. If the center of the wind field is moved to the subsolar point, vertical wind would be stronger near the equator.

At the visible wavelengths, the source of the geometric albedo variation was in the polar regions. Reflectivity was altered at the poles by varying the single scattering albedo and was accomplished through the effective radius of the haze particles. Upwelling of haze material decreased reflectivity because larger particle were moved to the unity optical depths and the single scattering albedo decreased. Hemispheric brightening was produced. Downwelling moved smaller particles and lowered reflectivity. Hemispheric darkening was producing. The reflectivity then varied the most where rising or sinking motion was produced by the wind field. The polar regions had the strongest convergence or divergence so they exhibited the largest variations of reflectivity over season.

The geometric albedo was also calculated at four other wavelengths. This was to provide further tests of our haze simulations. Two wavelength were in the UV spectral region and were 0.2225 and 0.35 μm. In the UV, Rayleigh scattering was a significant source of opacity. Hence, the geometric albedo was more dependent on both sources of opacity than in the visible. Two wavelengths were in the IR and were 0.888 and 1.075 μm. At 0.888 μm, the methane dominates absorption over the haze particles, so scattering from the haze particles can counter absorption. At 1.075 μm, the haze layer is the only source of atmospheric opacity, and is also optically thin, so the surface albedo affects the geometric albedo and the reflectivities. These additional sources of opacity produced variations of reflectivity which were produced in the different regions of the atmosphere. For all four wavelength, the temporal variations of the geometric albedo was out of phase with respect to the visible by $\simeq 180°$.

Circulation produced the brightness variations at these four wavelengths by varying the mixing ratio of the haze material. The mixing ratio had the largest variations in the mid latitude regions, where the wind vectors were mostly meridional. Our wind field then varied the haze mixing ratios at a constant altitude and changed in the mid latitudes the fraction of an optical depth from the haze particles. In the UV, reflectivity was inversely related to changes of haze mixing ratio, because Rayleigh scattering countered the absorption from the haze particles. At 0.888 μm, the reflectivity had a direct relation to changes in the haze mixing ratios, because the haze particles reduced the amount of absorption from methane. A hemisphere brightening was simultaneous at the UV and 0.888 μm, because the unity optical depths were at different altitudes between the UV and 0.888 μm. At these different altitudes, the speeds in our wind field varied so that the movement of haze material decreased with altitude. In the UV, movement of haze material was interhemispheric. At 0.888 μm, the material movements were between the polar and lower latitudes of a hemisphere. At 1.075 μm, the albedo variation were caused when the total column density of the haze varied, because the total optical depth was smaller at 1.075 μm than at the other three wavelengths. The reflectivity of a hemisphere was varied when haze material was moved between the pole and the lower latitudes within the same hemisphere. Brightening occurred in the upwelling hemisphere when haze material was swepted up to the pole. At 0.888 and 1.075 μm, a hemisphere was simultaneously brightened, because the location of the unity optical depths varied between the two wavelengths. At 1.075 μm, the optical depths were in the lower branch of the wind field where the wind vectors were opposite with respect to the upper branch. The optical depths at 0.888 μm were in the upper branch.

Our conclusion may be altered by latitudinal variations in atmospheric

composition, because the atmospheric structure did not vary over latitude in our simulations. To alter the albedo predictions from our simulations, the latitudinal variations in atmospheric composition would be have to greater than 10% which seems unlikely. In the UV, this unlikelyhood is especially true, because Rayleigh scattering is the other source of opacity. Rayleigh scattering is directly proportional to atmospheric density. At 0.888 μm, our conclusion are slightly more dependent on the assumed composition, because the other opacity source is from methane. The latitudinal variation of methane should not alter our results, because the atmospheric lifetime of methane is longer than a season for Titan, 7.38 years. Our conclusions may be more dependent on our representation of circulation, especially if eddy diffusion is stronger than believed. The simulations in the IR are more susceptible to eddy diffusion because the wind speeds at the unity optical depths were slow. Eddy diffusion could then diminish the haze variations in our simulations. We do believe that our simualtions can be used to understand or to predict the effects on the geometric albedo for a more realistic or accurate representation of the circulation.

FINAL CONCLUSION AND RECOMMENDATIONS

The circulation is the better source of the observations of the geometric albedo and the hemispheric brightness. Both sources were able to produce some of the observation, if the model parameters were properly adjusted. The circulation source is preferable for two reasons. The production variations produced only the size of the observed variations. The circulation variations matched the size and temporal variation of the observations. The two dimensional model for the circulation source also produced a better agreement without the atmospheric conditions which may be considered unrealistic. In

the one dimensional model for the production source, the stratospheric rain-out of the haze particles was required to produce the size of the observed variation in the geometric albedo.

Our two dimensional model did have problems from our representation of the circulation. Problems were indicated, because our simulations of the hemispheric brightness contrast were poor. Our representation of the circulation also contained several assumptions which were probably incorrect. In the derivation of our wind field, the quasi-geostrophic approximation was assumed and is incorrect, because Titan is in the cyclostrophic approximation. Spherical effects on the circulation were neglected so our wind field may have been weak in the polar regions because the convergence at the poles was neglected. The spherical effects may be especially significant on the circulation of Titan. The solar forcing for our derived wind field is also a weakest, because it did not depend upon the atmospheric density which changes several orders of magnitude over the height of the stratosphere. Consequently, the winds had a vertical variation which was incorrect. The solar forcing in the derivation was time independent so our seasonal variation of the circulation may have not been realistic. For example, the center of the wind field is always located at the same point.

The main improvement to the two dimensional model is a wind field which is more accurate, and could be best accomplished by a numerical model of the circulation. This method of improvement is preferable to seeking analytical solution to the governing equations, because cyclostrophic circulation is extremely difficult to solve. The solution is difficult, because it is nonlinear. A new representation of the circulation should also come from a model which is three dimensional. The zonal circulation of Titan is strong enough that it can not be ignored in the meridional circulation. A three dimensional

model can also be used for values of the eddy diffusion coefficients. The haze variations from eddy diffusion can then be evaluated. When a new representation of the circulation is used, an implicit assumption is that the aerosol model uses spherical coordinates.

The two dimensional model can also be used for other uses. Other sources of observed variations in hemispheric brightness can be examined. Although temporal variation of haze production was determined an unlikely source, we should determine the reflectivity variations when haze production varies over latitude. The two dimensional model can also used for determining the effects from compositional variations of the haze material. Photochemical models are now developing a sophistication which could be used to determine the seasonal variations of the haze absorption coefficient. Other uses of the two dimensional model do not deal with simulating the albedos of Titan, but how latitudinal variations in the haze layer can effect the thermal structure, and circulation of the atmosphere. Heating rates can be estimated from our simulations of the haze distributions. These heating rates can be used to determine how radiative equilibrium varies over latitude and seasons. Heating rate can also be used in general circulation models.

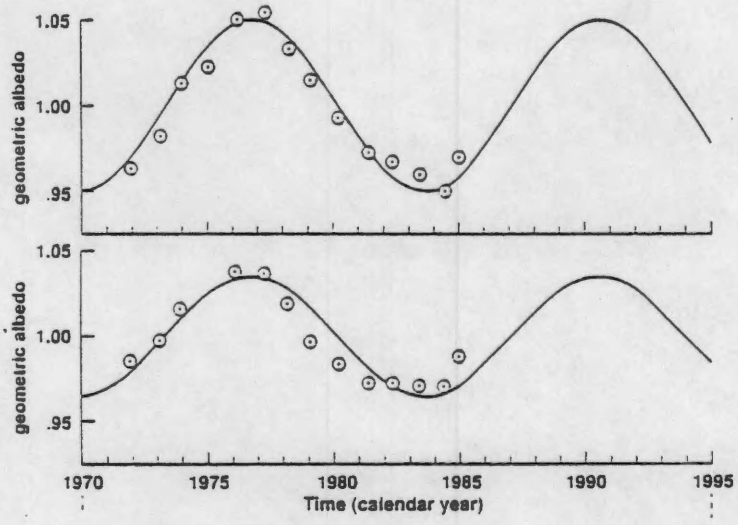
1.05
1.00
.95
geometric albedo
1.05
1.00
.95
geometric albedo
1970
1975
1980
1985
1990
1995
Time (calendar year)

Figure 1.1:

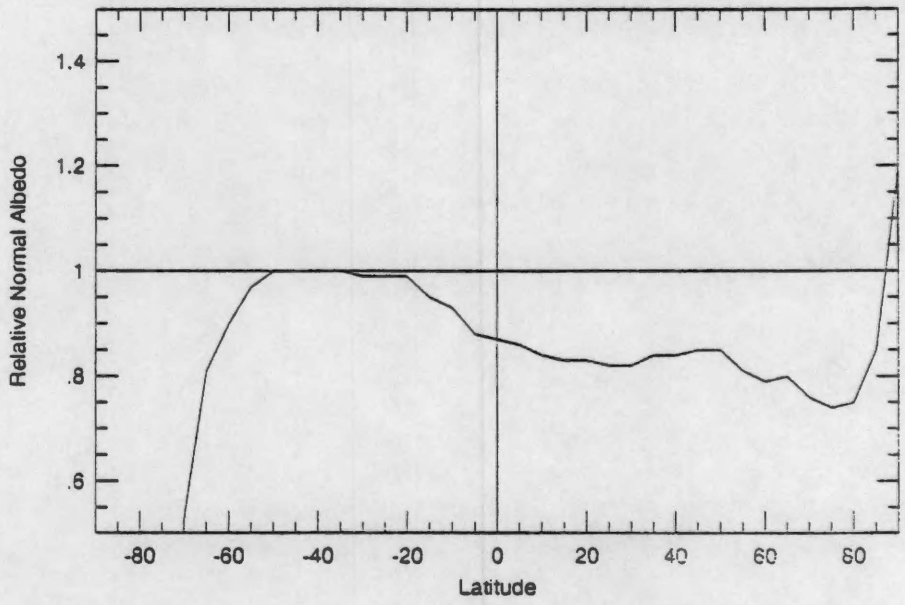
Relative Normal Albedo
1.4
1.2
1
.8
.6
-80
-60
-40
-20
0
20
40
60
80
Latitude

Figure 1.2:

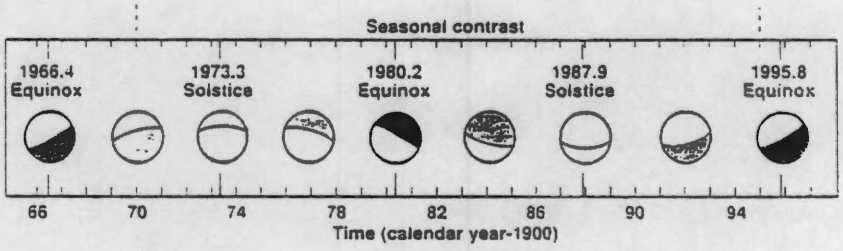
Seasonal contrast
1966.4
Equinox
1973.3
Solstice
1980.2
Equinox
1987.9
Solstice
1995.8
Equinox
66
70
74
78
82
86
90
94
Time (calendar year-1900)

Figure 1.3:

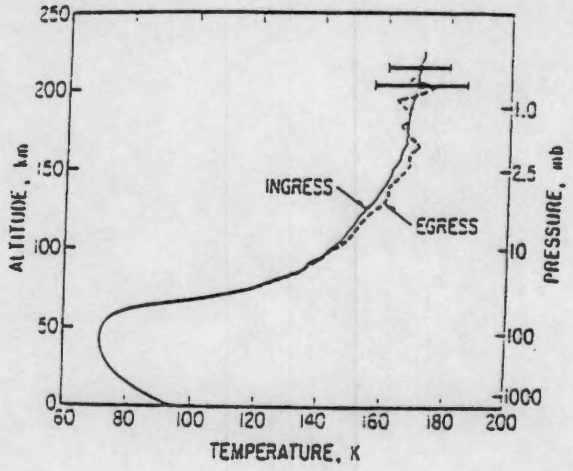
250
200
150
100
50
0
ALTITUDE, km
INGRESS
EGRESS
1.0
2.5
10
100
1000
PRESSURE, mb
60
80
100
120
140
160
180
200
TEMPERATURE, K

Figure 1.4:

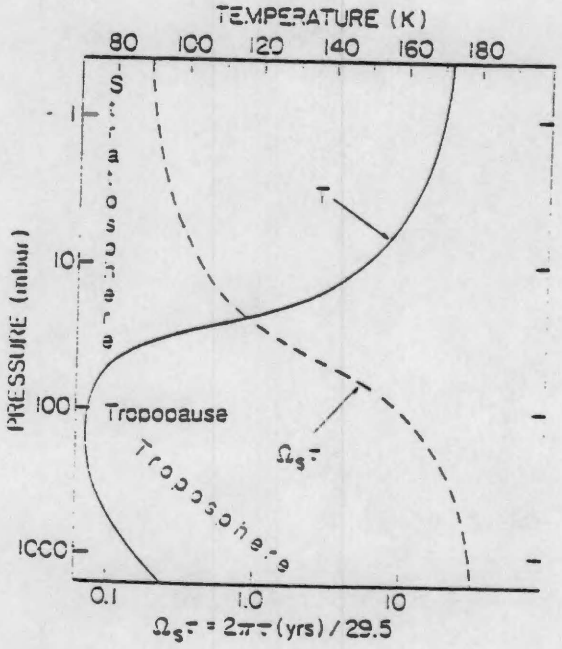
TEMPERATURE (K)
80
100
120
140
160
180
PRESSURE (mbar)
1
10
100
1000
Tropopause
Troposphere
0.1
1.0
10
$\Omega_s\tau = 2\pi\tau$ (yrs) / 29.5

Figure 1.5:

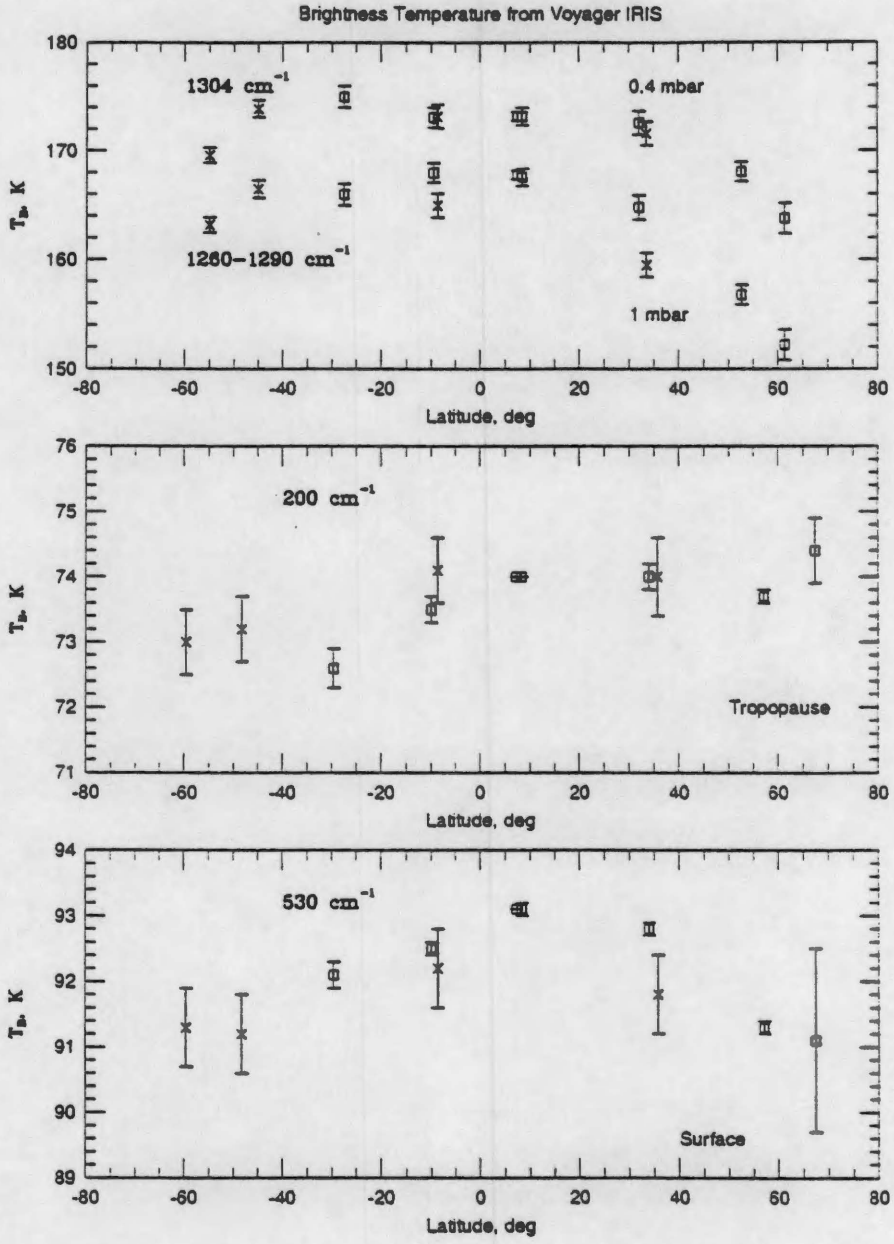
Brightness Temperature from Voyager IRIS
1304 cm^{-1}
0.4 mbar
1260–1290 cm^{-1}
1 mbar
T_b, K
Latitude, deg
200 cm^{-1}
Tropopause
530 cm^{-1}
Surface

Figure 1.6:

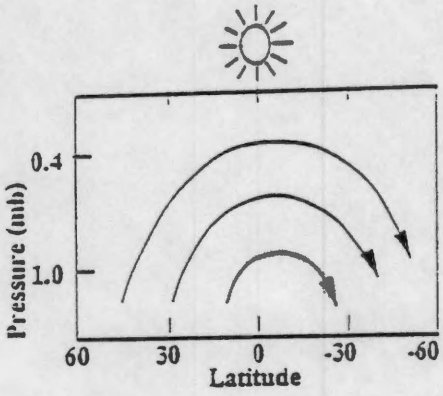

Figure 1.7:

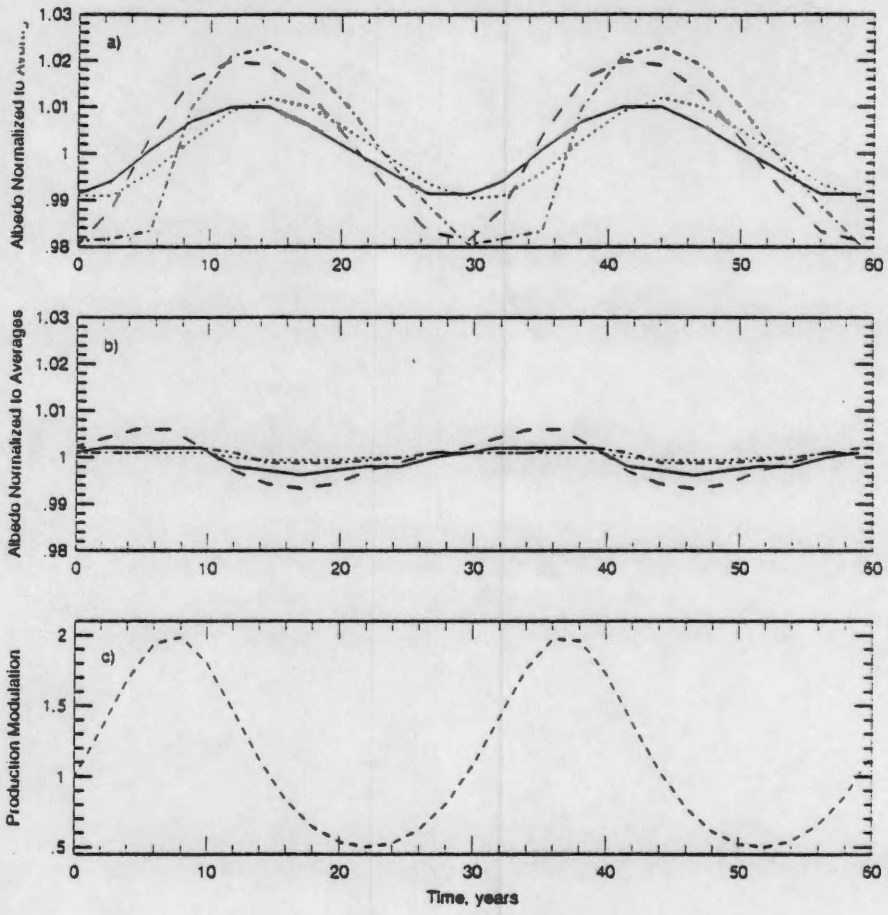
a)
b)
c)
Albedo Normalized to Averages
Production Modulation
Time, years
1.03
1.02
1.01
1
.99
.98
2
1.5
.5
0
10
20
30
40
50
60

Figure 2.2:

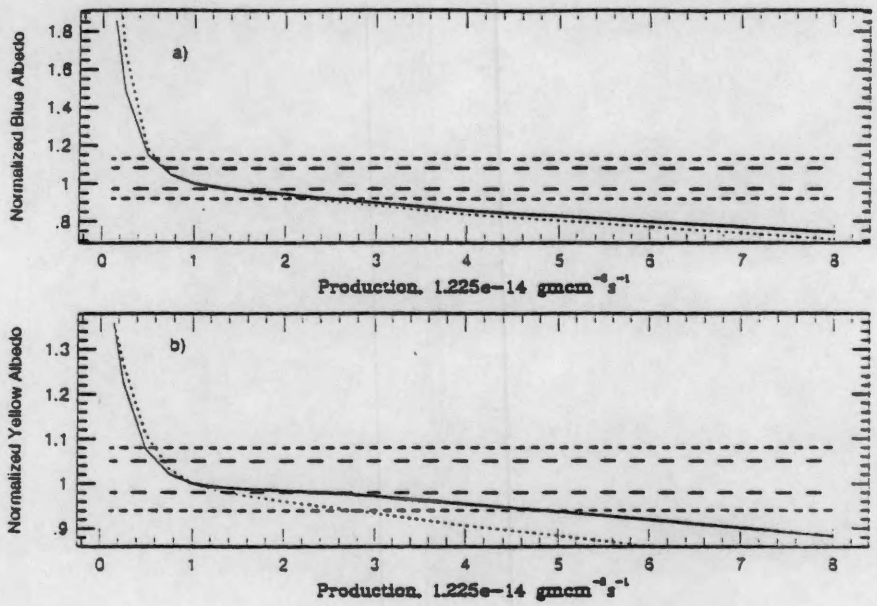
a)
Normalized Blue Albedo
1.8
1.6
1.4
1.2
1
.8
0
1
2
3
4
5
6
7
8
Production, 1.225e−14 gmcm^{-3}s^{-1}
b)
Normalized Yellow Albedo
1.3
1.2
1.1
1
.9
0
1
2
3
4
5
6
7
8
Production, 1.225e−14 gmcm^{-3}s^{-1}

Figure 2.1:

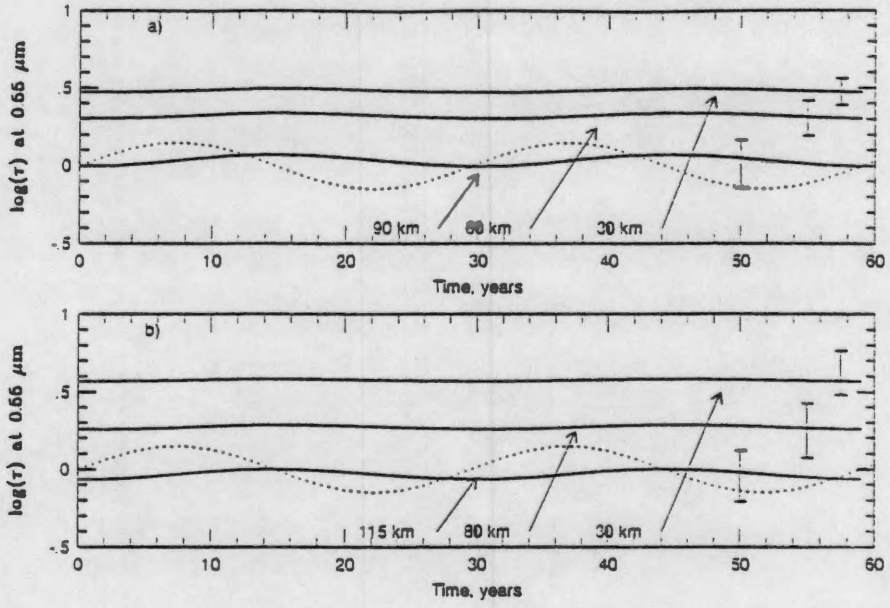
a)
log(τ) at 0.65 μm
1
.5
0
-.5
90 km
80 km
30 km
0
10
20
30
40
50
60
Time, years
b)
log(τ) at 0.66 μm
1
.5
0
-.5
115 km
80 km
30 km
0
10
20
30
40
50
60
Time, years

Figure 2.3:

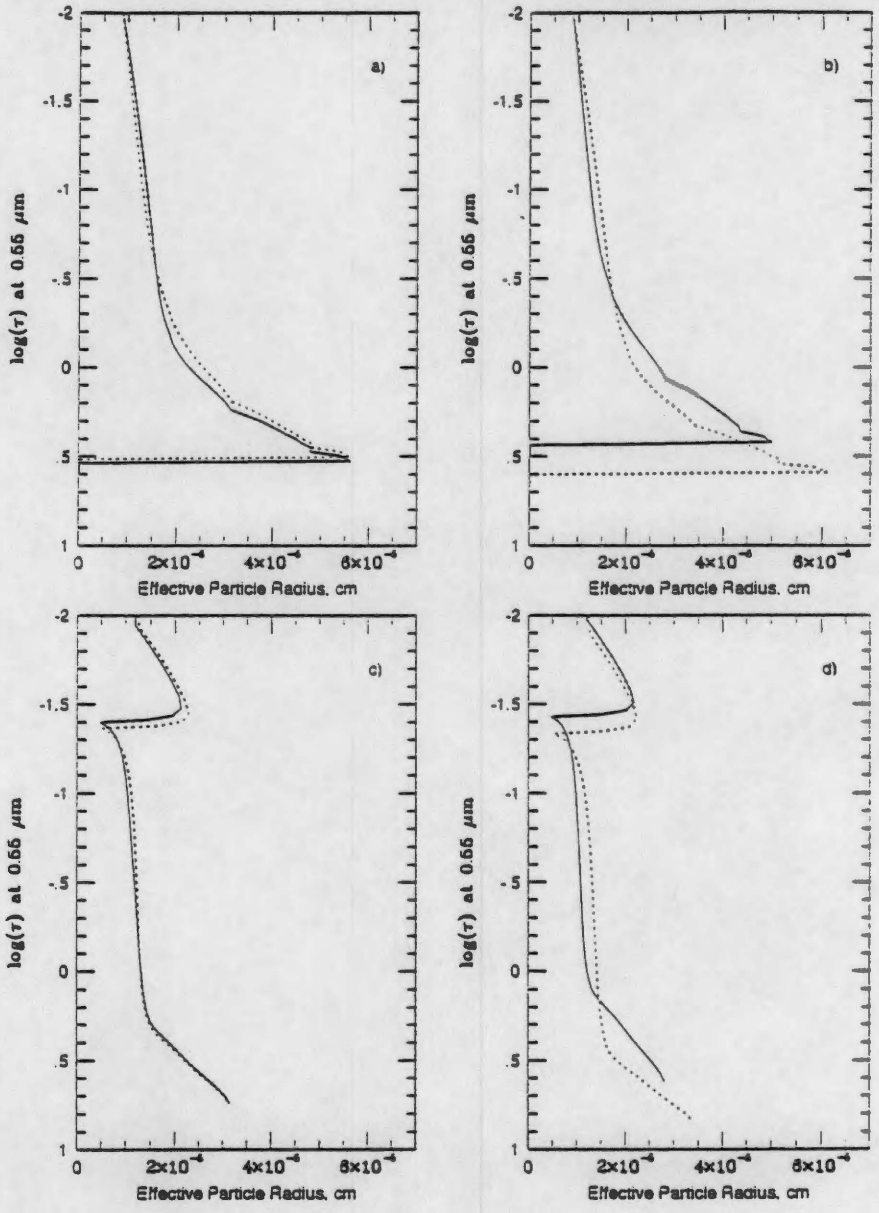
a)
b)
c)
d)
log(τ) at 0.55 μm
Effective Particle Radius, cm
-2
-1.5
-1
-.5
0
.5
1
0
2x10⁻⁶
4x10⁻⁶
6x10⁻⁶

Figure 2.6:

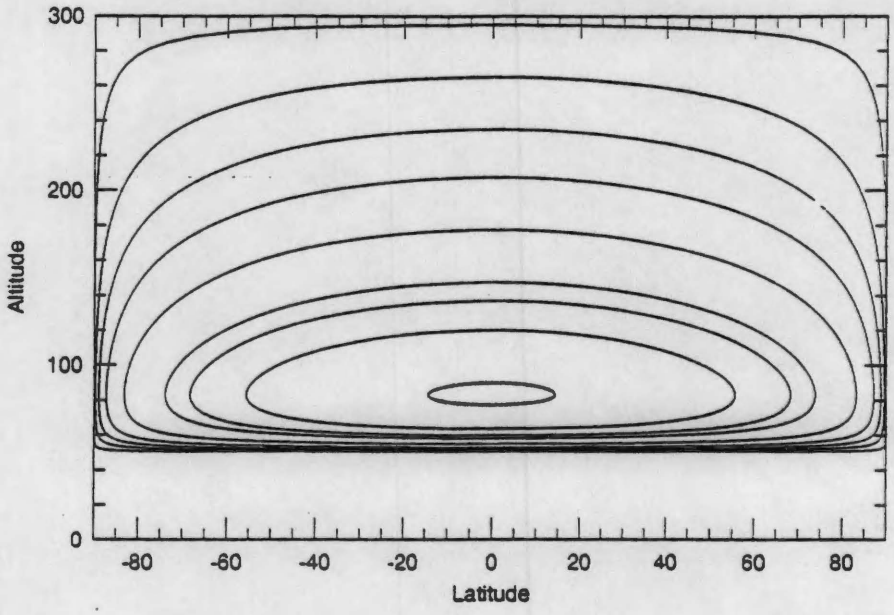

Figure 3.1:

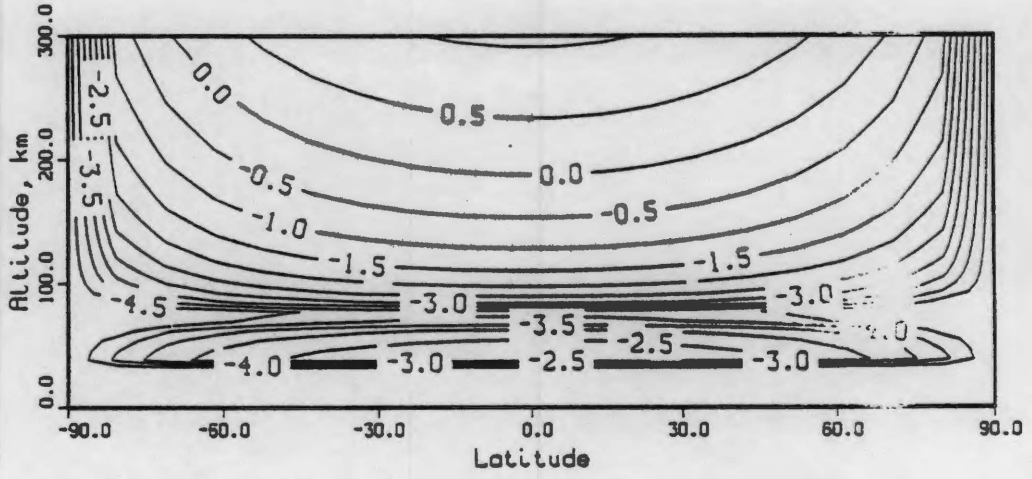
Altitude, km
300.0
200.0
100.0
0.0
-2.5
-3.5
0.0
0.5
-0.5
0.0
-1.0
-0.5
-1.5
-1.5
-4.5
-3.0
-3.0
-3.5
-2.5
-4.0
-3.0
-2.5
-3.0
-90.0
-60.0
-30.0
0.0
30.0
60.0
90.0
Latitude

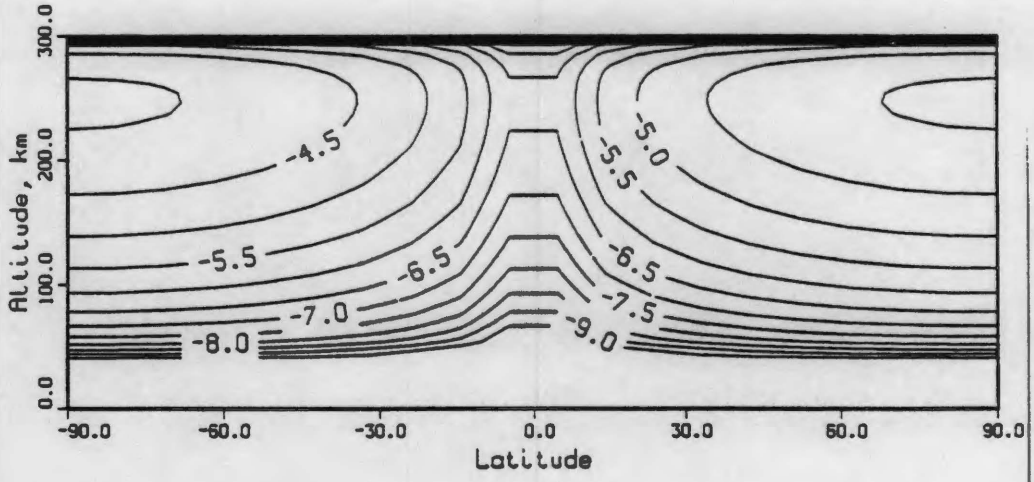
Altitude, km
300.0
200.0
100.0
0.0
-4.5
-5.0
-5.5
-5.5
-6.5
-6.5
-7.0
-7.5
-8.0
-9.0
-90.0
-60.0
-30.0
0.0
30.0
60.0
90.0
Latitude

Figure 3.2:

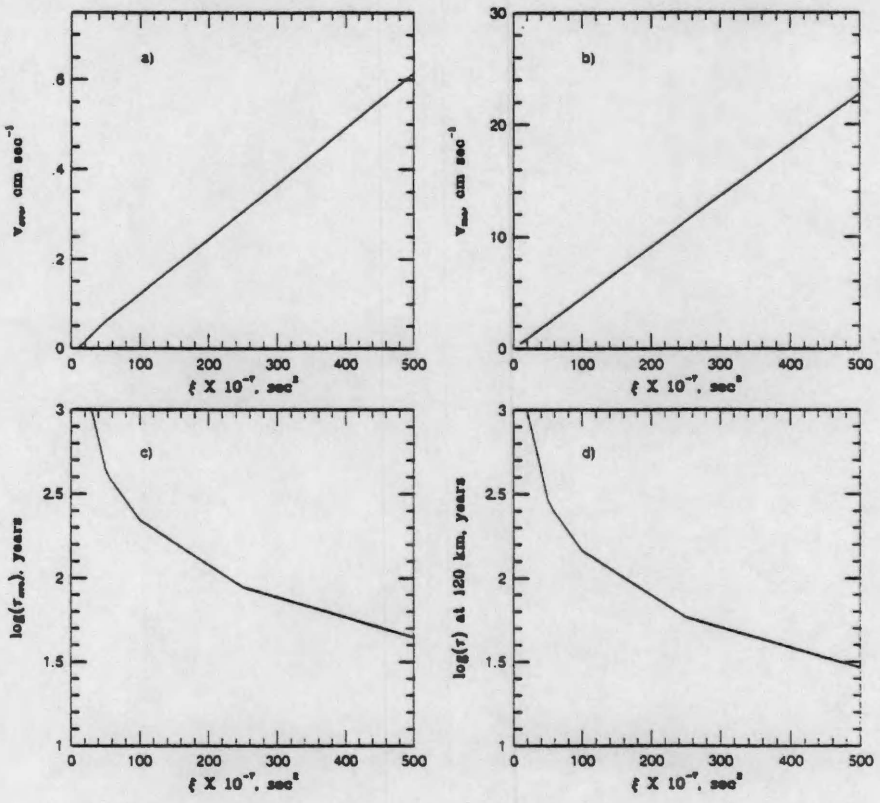
a)
b)
c)
d)
V_{max}, cm sec^{-1}
$\log(r_{max})$, years
$\log(r)$ at 120 km, years
ξ X 10^{-7}, sec^2
0
100
200
300
400
500
.2
.4
.6
10
20
30
1
1.5
2
2.5
3

Figure 3.3:

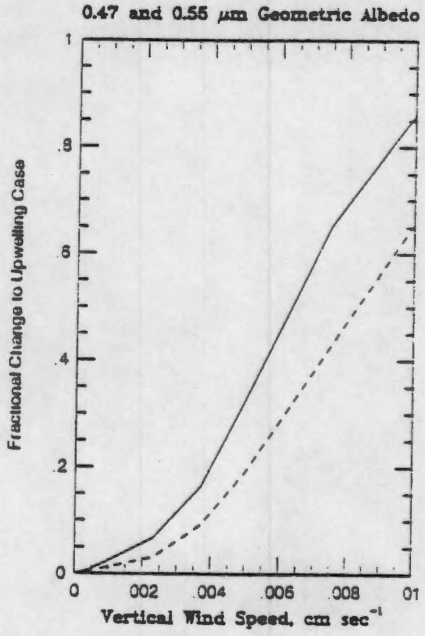
0.47 and 0.55 μm Geometric Albedo
Fractional Change to Upwelling Case
1
.8
.6
.4
.2
0
0
002
.004
.006
.008
01
Vertical Wind Speed, cm sec-1

Figure 4.1:

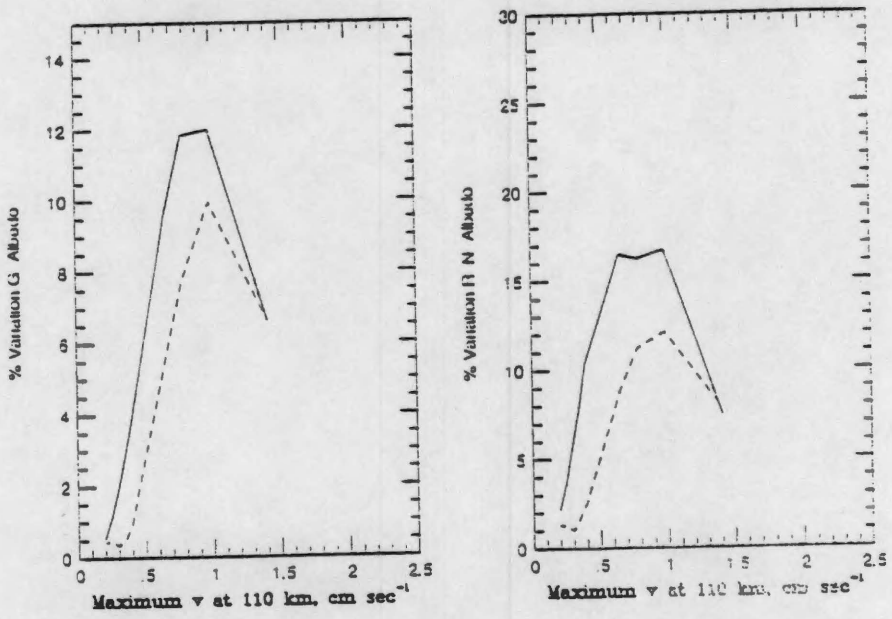
% Variation G Albedo
0
2
4
6
8
10
12
14
0
.5
1
1.5
2
2.5
Maximum v at 110 km, cm sec^{-1}
% Variation R N Albedo
0
5
10
15
20
25
30
0
.5
1
1.5
2
2.5
Maximum v at 110 km, cm sec^{-1}

Figure 4.2:

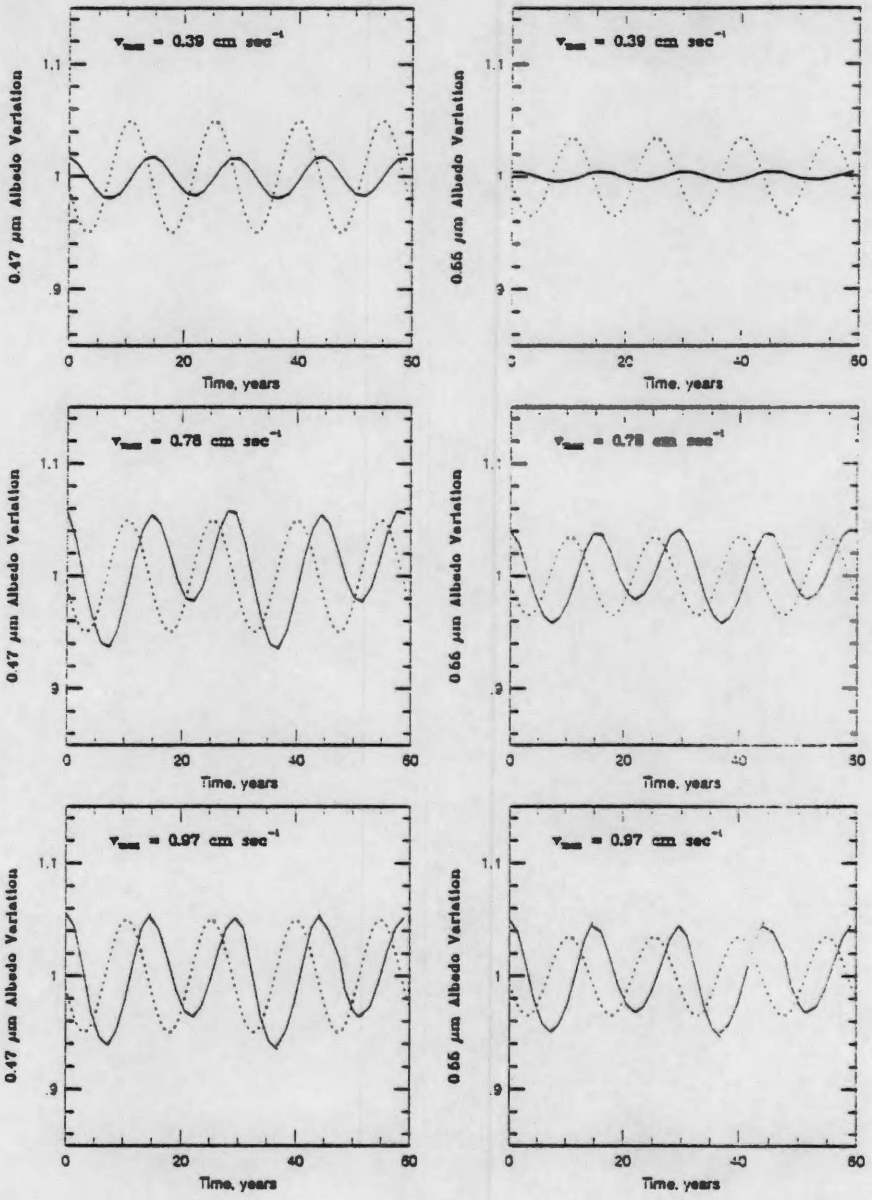
0.47 μm Albedo Variation
0.66 μm Albedo Variation
Time, years
1.1
1
.9
0
20
40
60

Figure 4.3:

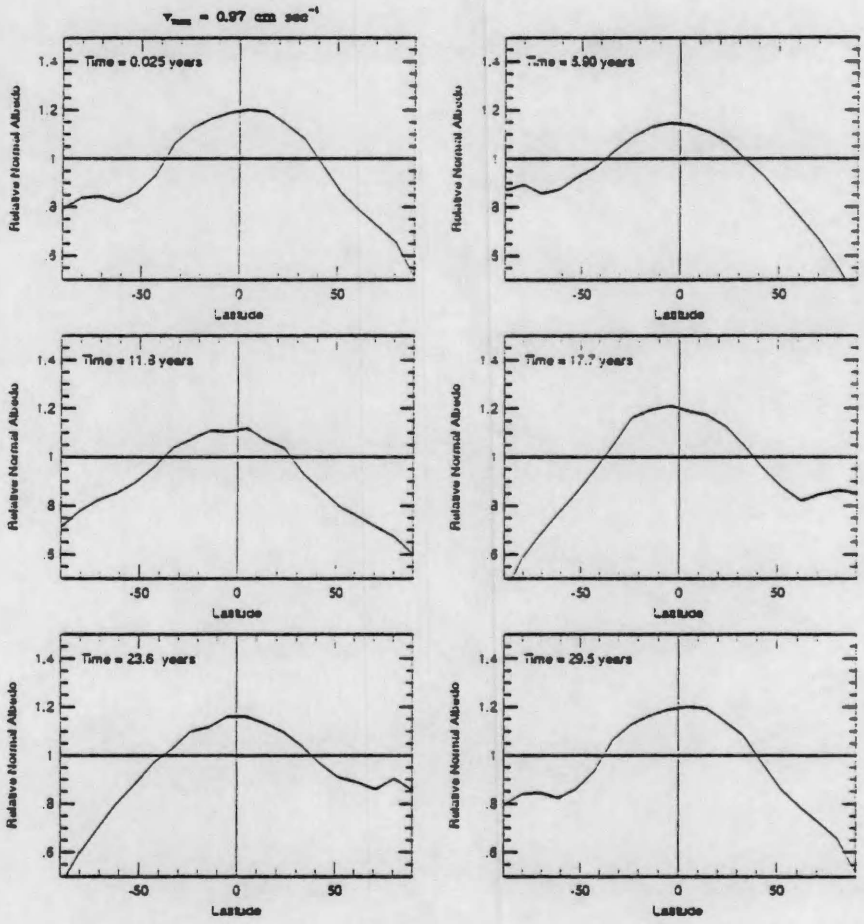
Time = 0.025 years
Time = 5.90 years
Time = 11.8 years
Time = 17.7 years
Time = 23.6 years
Time = 29.5 years
Relative Normal Albedo
Latitude
-50
0
50

Figure 4.4:

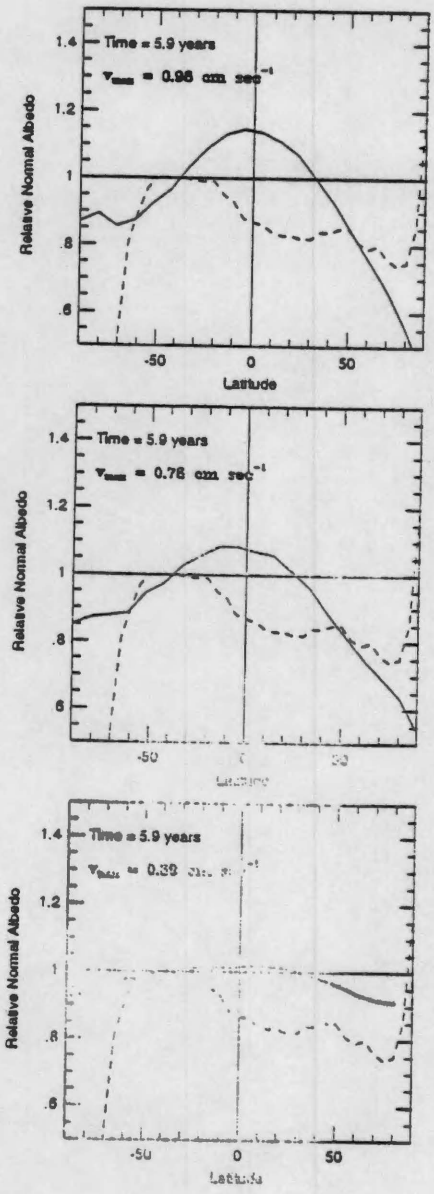
Time = 5.9 years
Relative Normal Albedo
1.4
1.2
1
.8
.6
-50
0
50
Latitude
Time = 5.9 years
Relative Normal Albedo
1.4
1.2
1
.8
.6
-50
Time = 5.9 years
Relative Normal Albedo
1.4
1.2
1
.8
.6
-50
0
50

Figure 4.5:

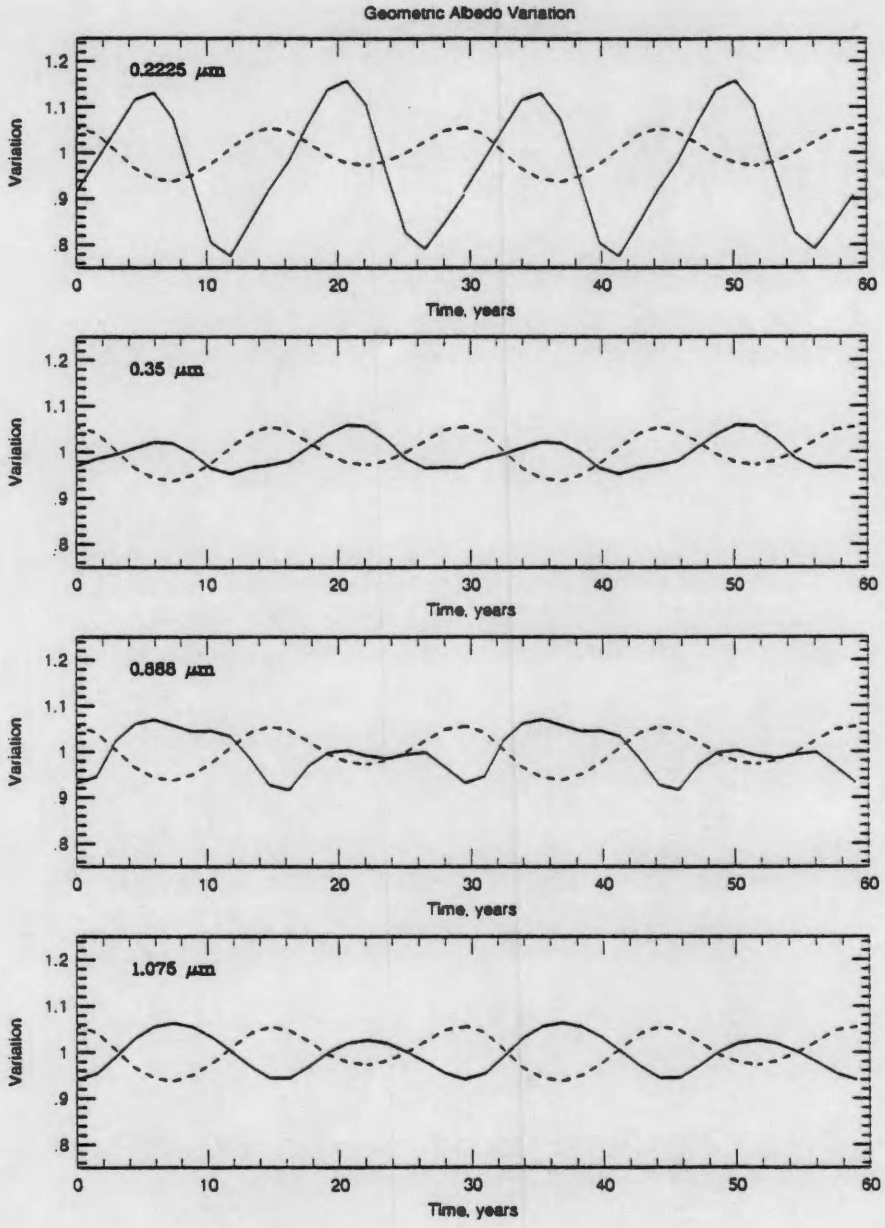
Geometric Albedo Variation
0.2225 μm
0.35 μm
0.888 μm
1.075 μm
Variation
Time, years
1.2
1.1
1
.9
.8
0
10
20
30
40
50
60

Figure 4.6:

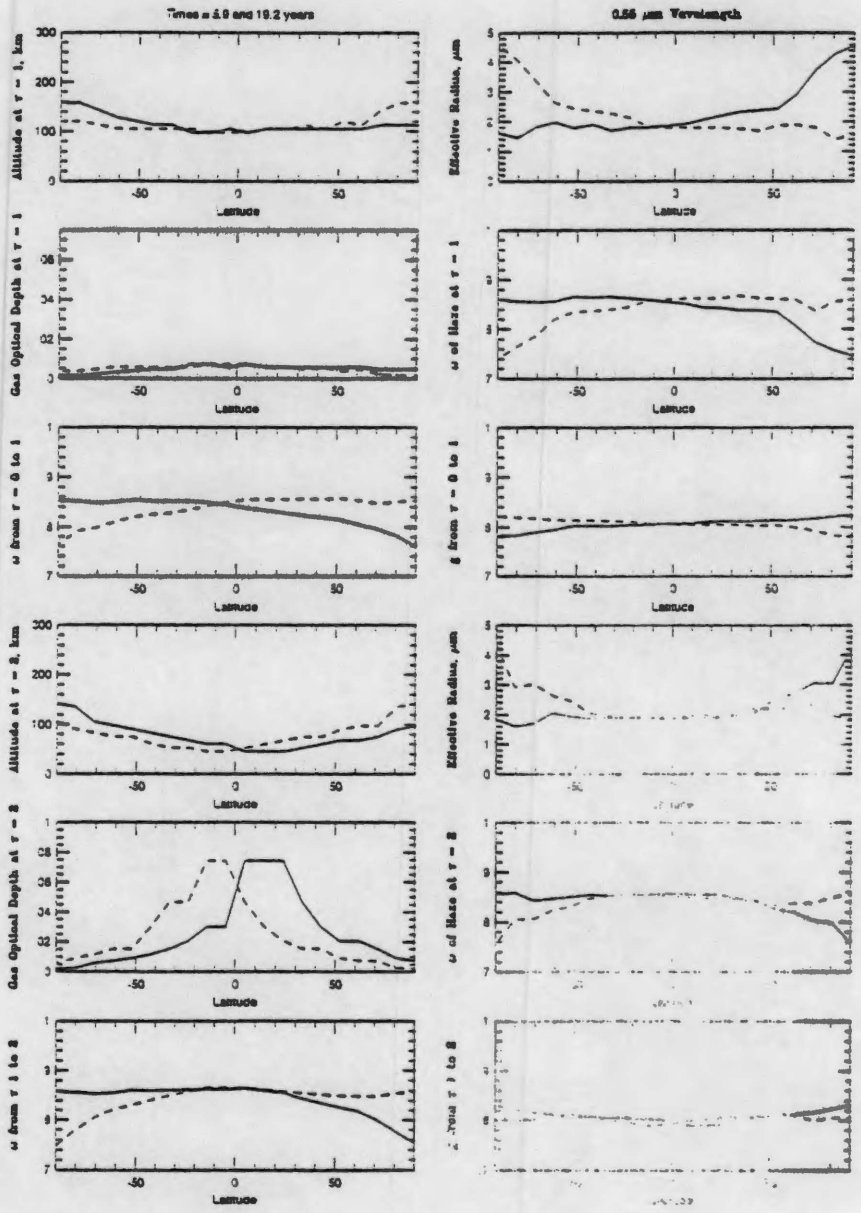
Times = 5.9 and 19.2 years
0.55 μm Wavelength
Altitude at τ = 1, km
Effective Radius, μm
Gas Optical Depth at τ = 1
ω of Haze at τ = 1
ω from τ = 0 to 1
δ from τ = 0 to 1
Altitude at τ = 2, km
Effective Radius, μm
Gas Optical Depth at τ = 2
ω of Haze at τ = 2
ω from τ = 1 to 2
Latitude

Figure 4.7:

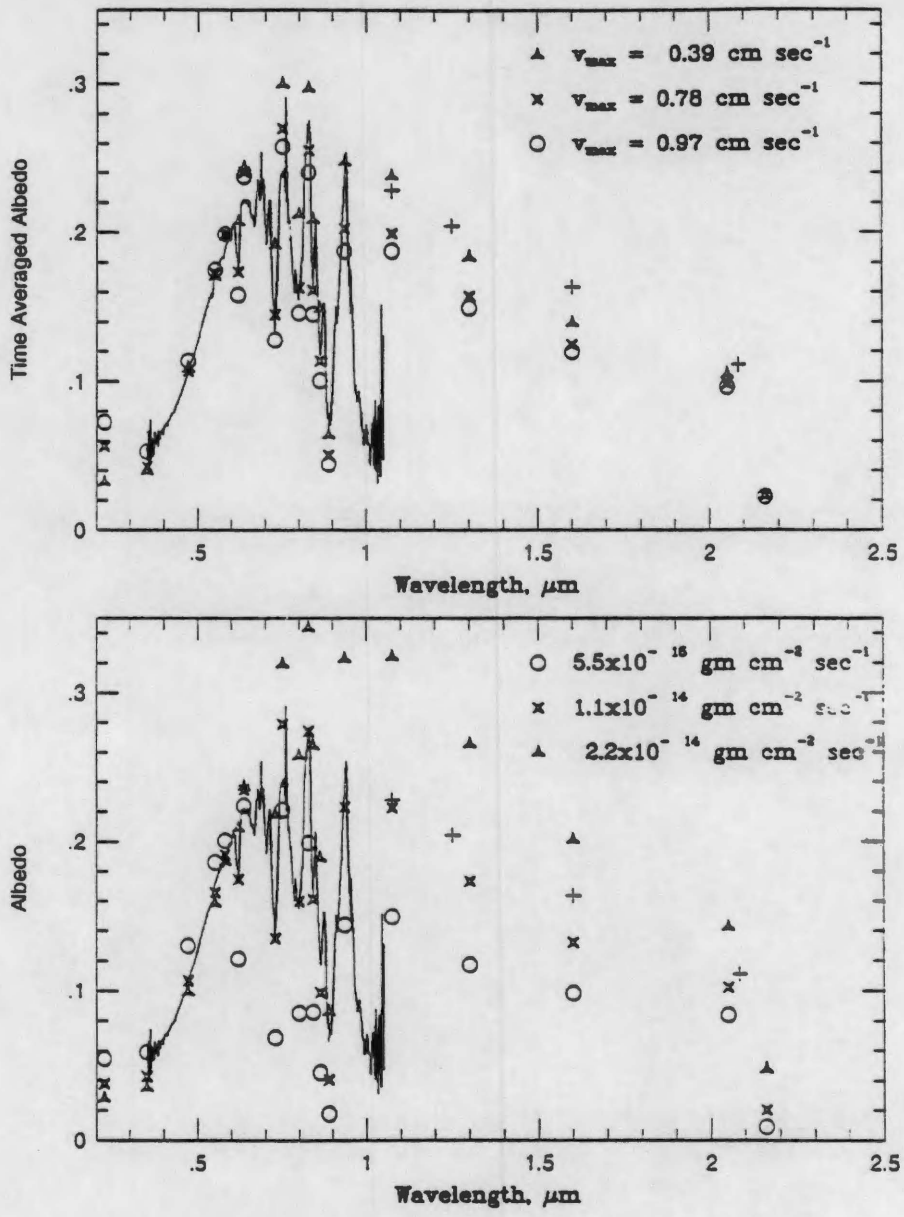
Time Averaged Albedo
v_{max} = 0.39 cm sec^{-1}
v_{max} = 0.78 cm sec^{-1}
v_{max} = 0.97 cm sec^{-1}
Wavelength, μm
Albedo
5.5x10^{-16} gm cm^{-2} sec^{-1}
1.1x10^{-14} gm cm^{-2}
2.2x10^{-14} gm cm^{-2}
Wavelength, μm

Figure 4.8:

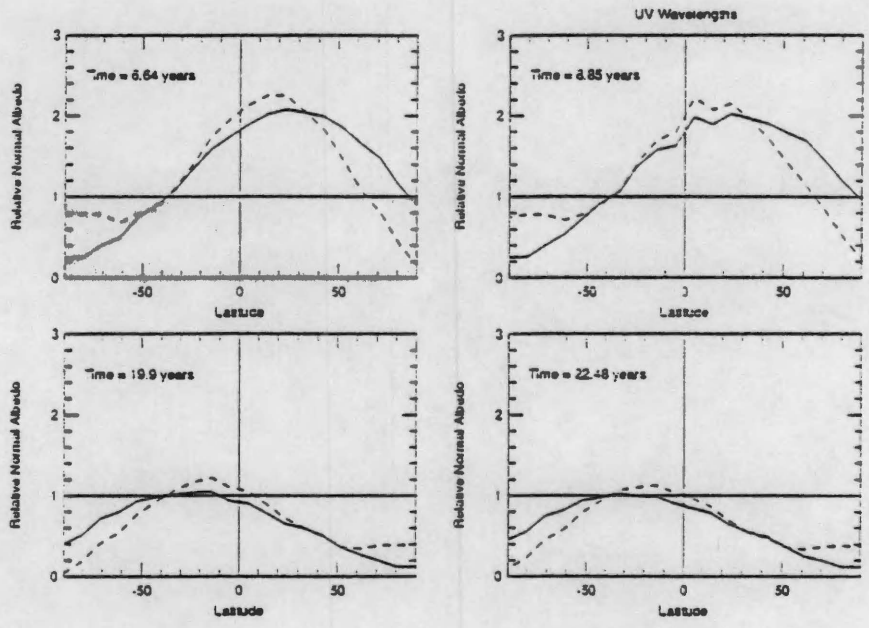
UV Wavelengths
Time = 8.64 years
Time = 8.85 years
Time = 19.9 years
Time = 22.48 years
Relative Normal Albedo
Latitude
-50
0
50
1
2
3

Figure 4.9:

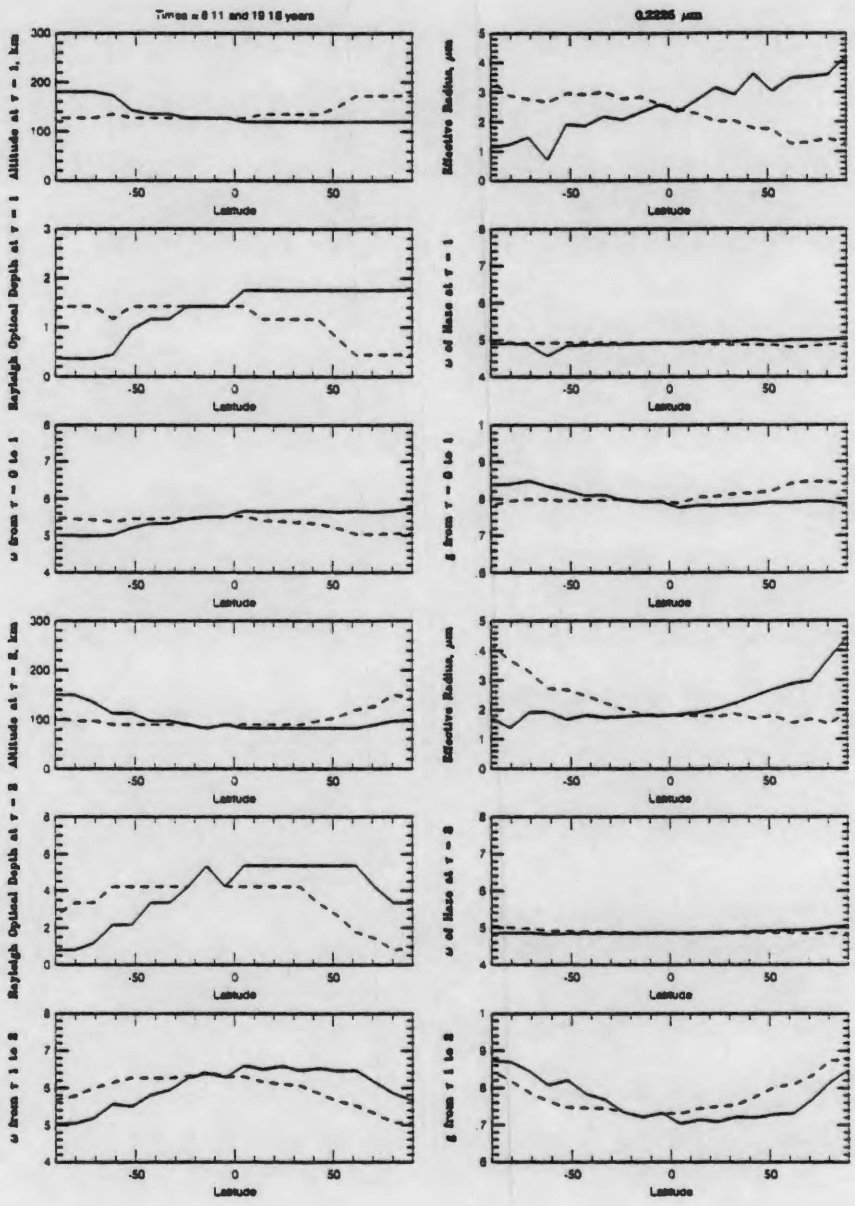

Figure 4.10:

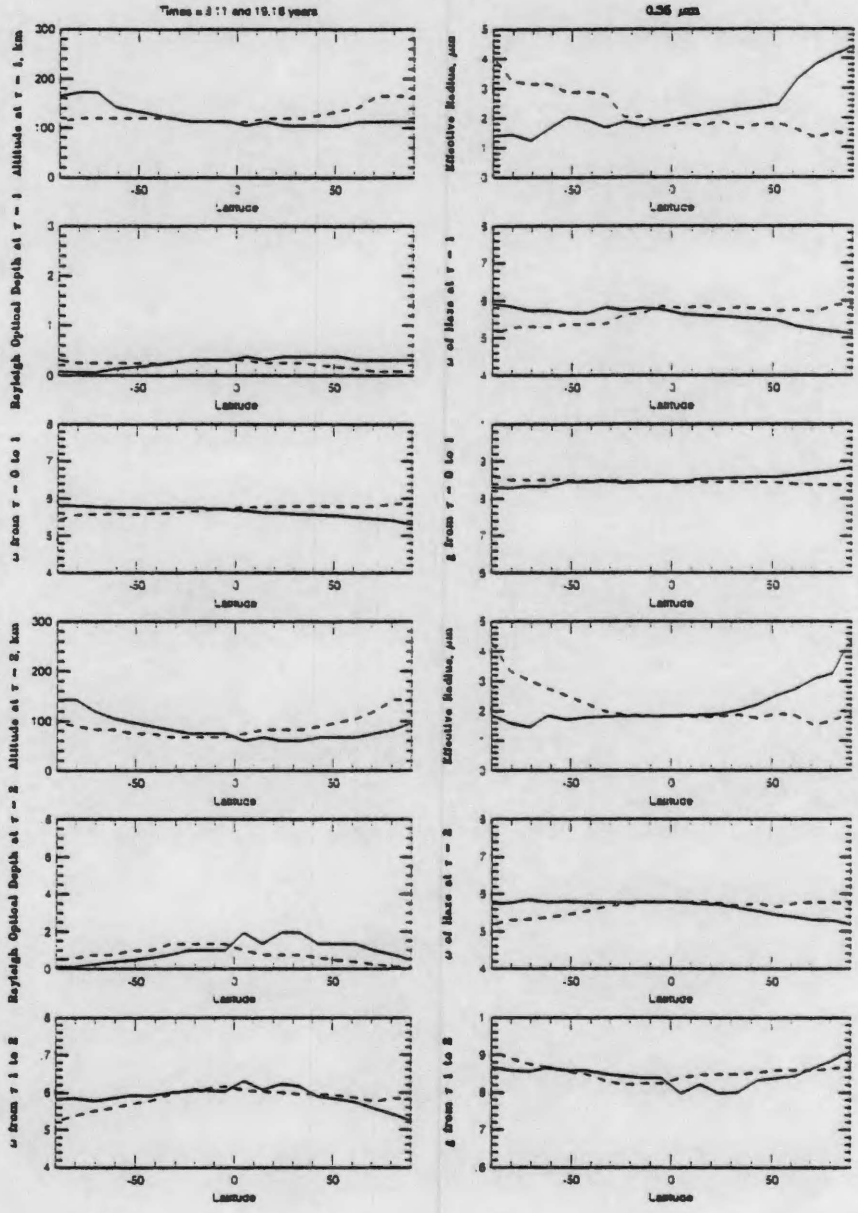

Figure 4.11:

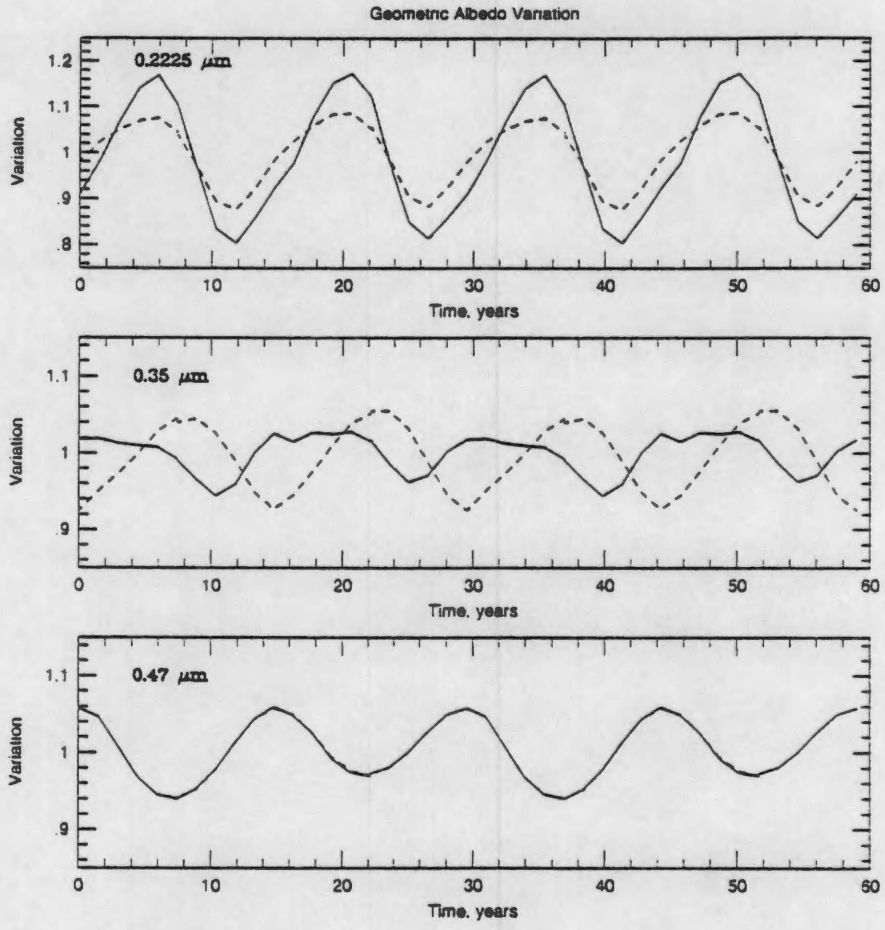
Geometric Albedo Variation
0.2225 μm
0.35 μm
0.47 μm
Variation
Time, years
1.2
1.1
1
.9
.8
0
10
20
30
40
50
60

Figure 4.12:

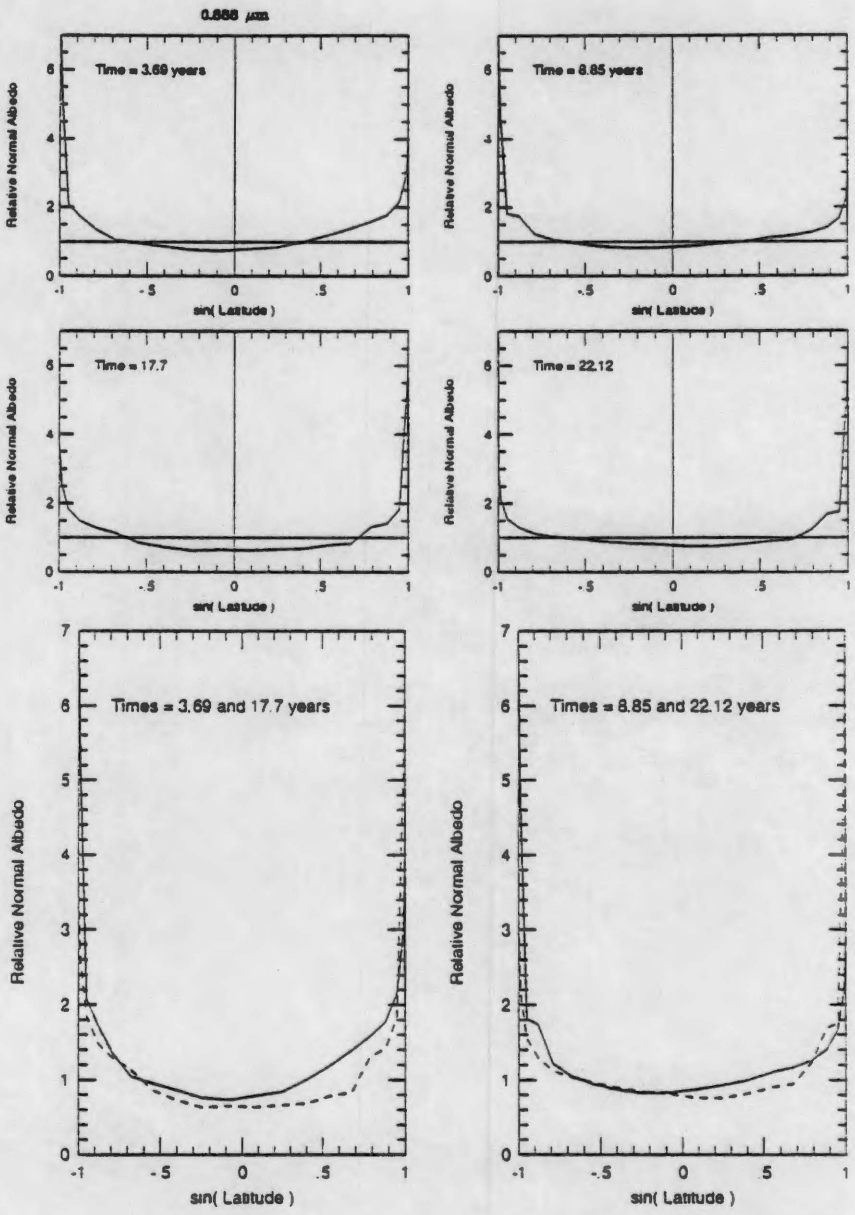
0.888 μm
Time = 3.69 years
Time = 8.85 years
Time = 17.7
Time = 22.12
Times = 3.69 and 17.7 years
Times = 8.85 and 22.12 years
Relative Normal Albedo
sin(Latitude)

Figure 4.13:

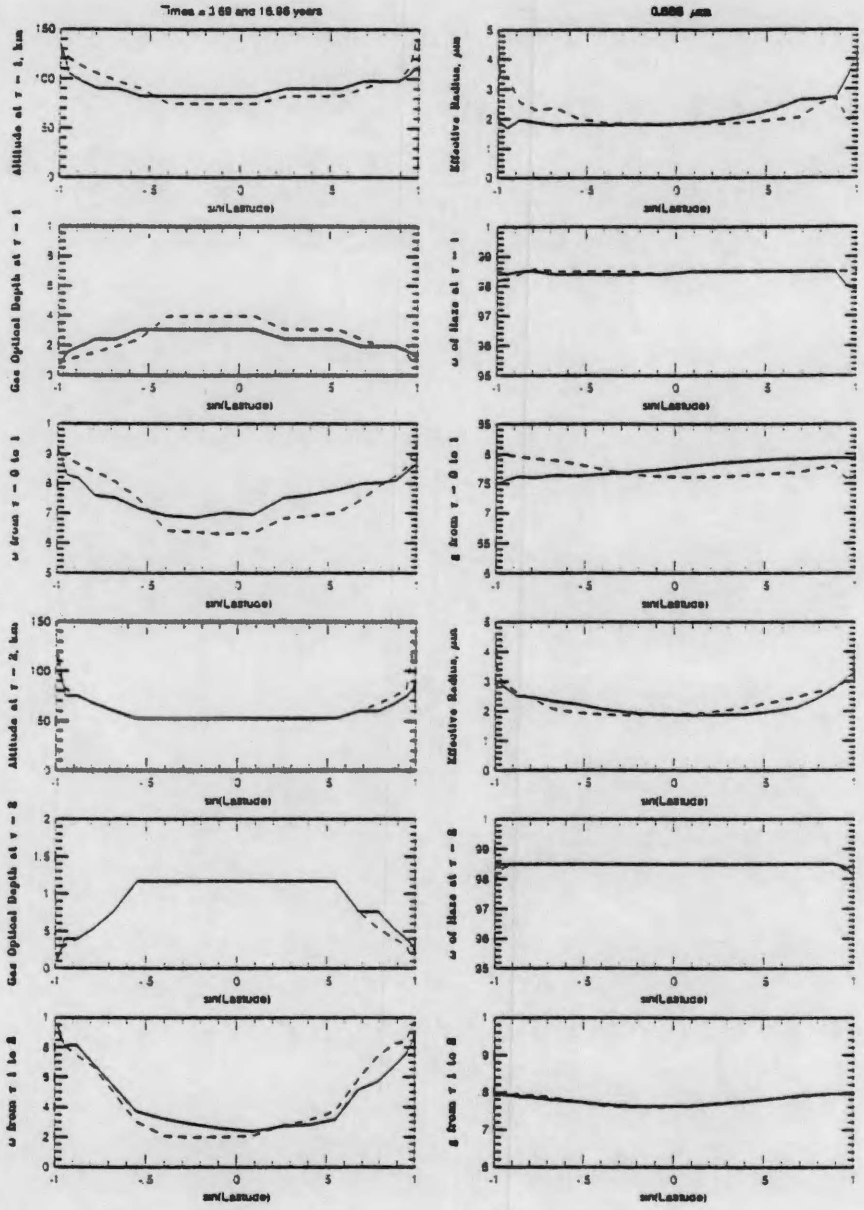

Figure 4.14:

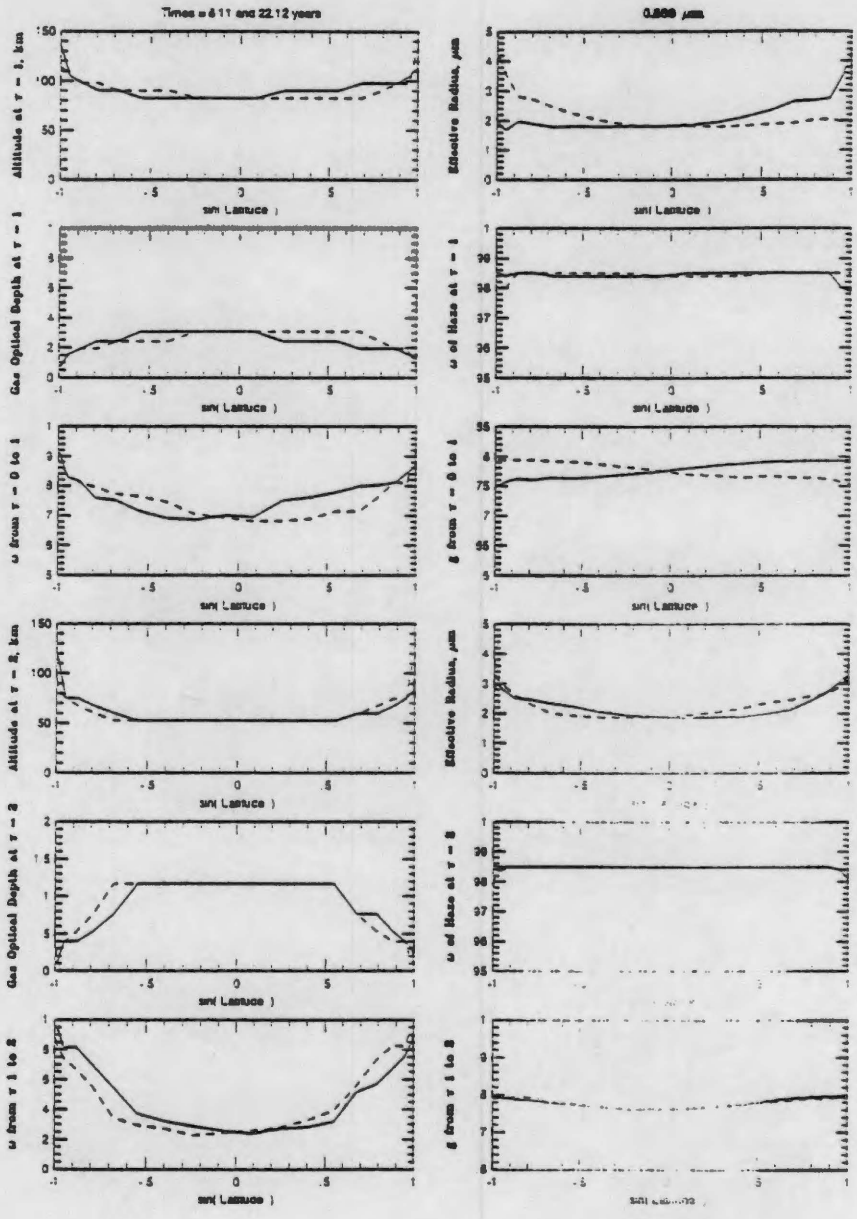

Figure 4.15:

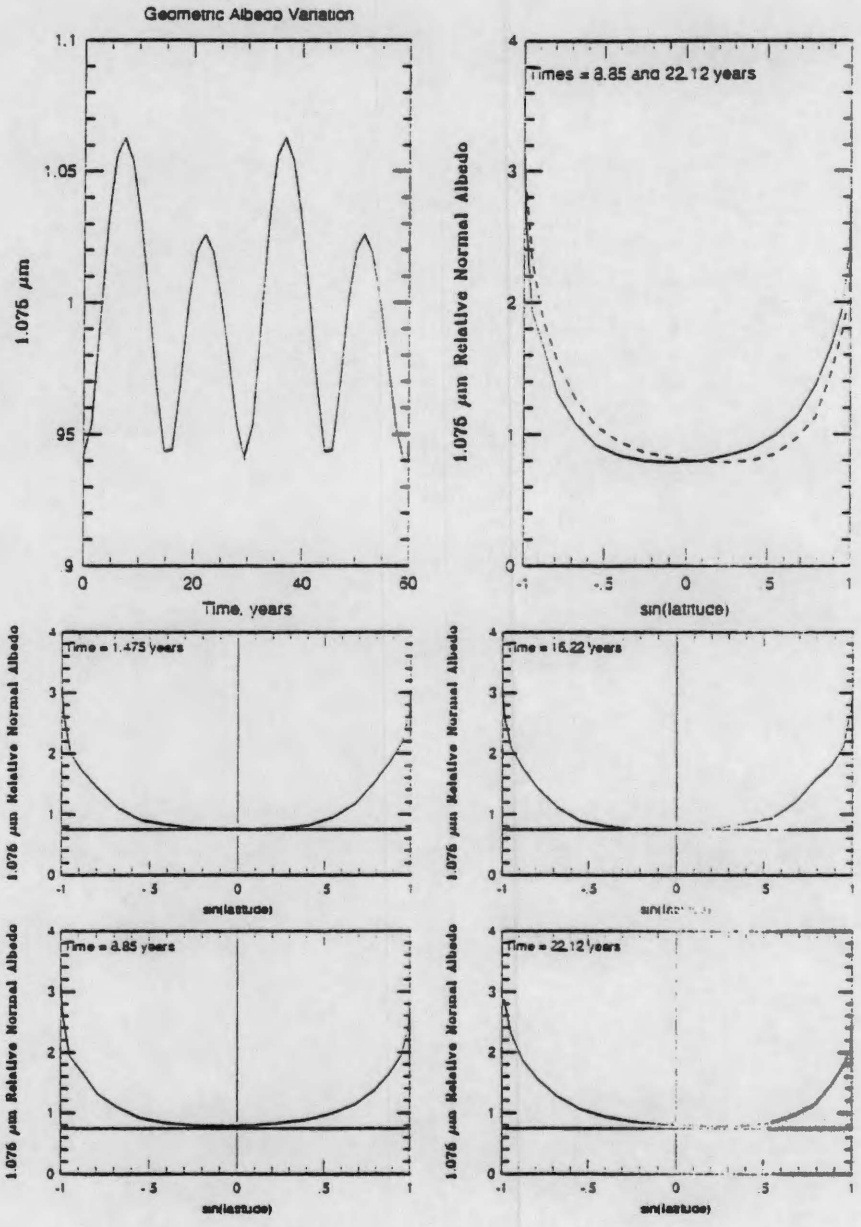
Geometric Albedo Variation
1.076 μm
Time, years
1.076 μm Relative Normal Albedo
Times = 8.85 and 22.12 years
sin(latitude)
Time = 1.475 years
Time = 8.85 years
Time = 15.22 years
Time = 22.12 years

Figure 4.16:

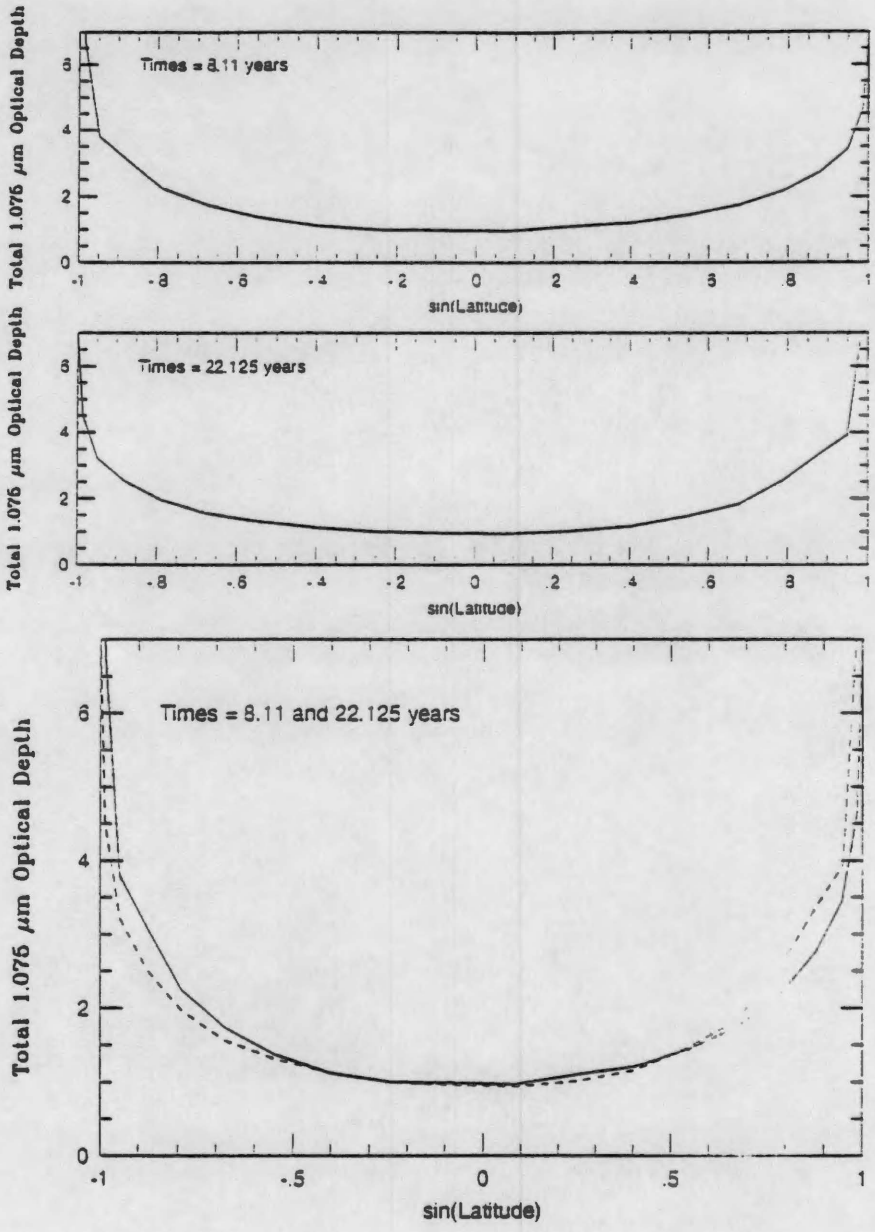
Total 1.076 μm Optical Depth
Times = 8.11 years
sin(Latitude)
Total 1.076 μm Optical Depth
Times = 22.125 years
sin(Latitude)
Total 1.076 μm Optical Depth
Times = 8.11 and 22.125 years
sin(Latitude)

Figure 4.17:

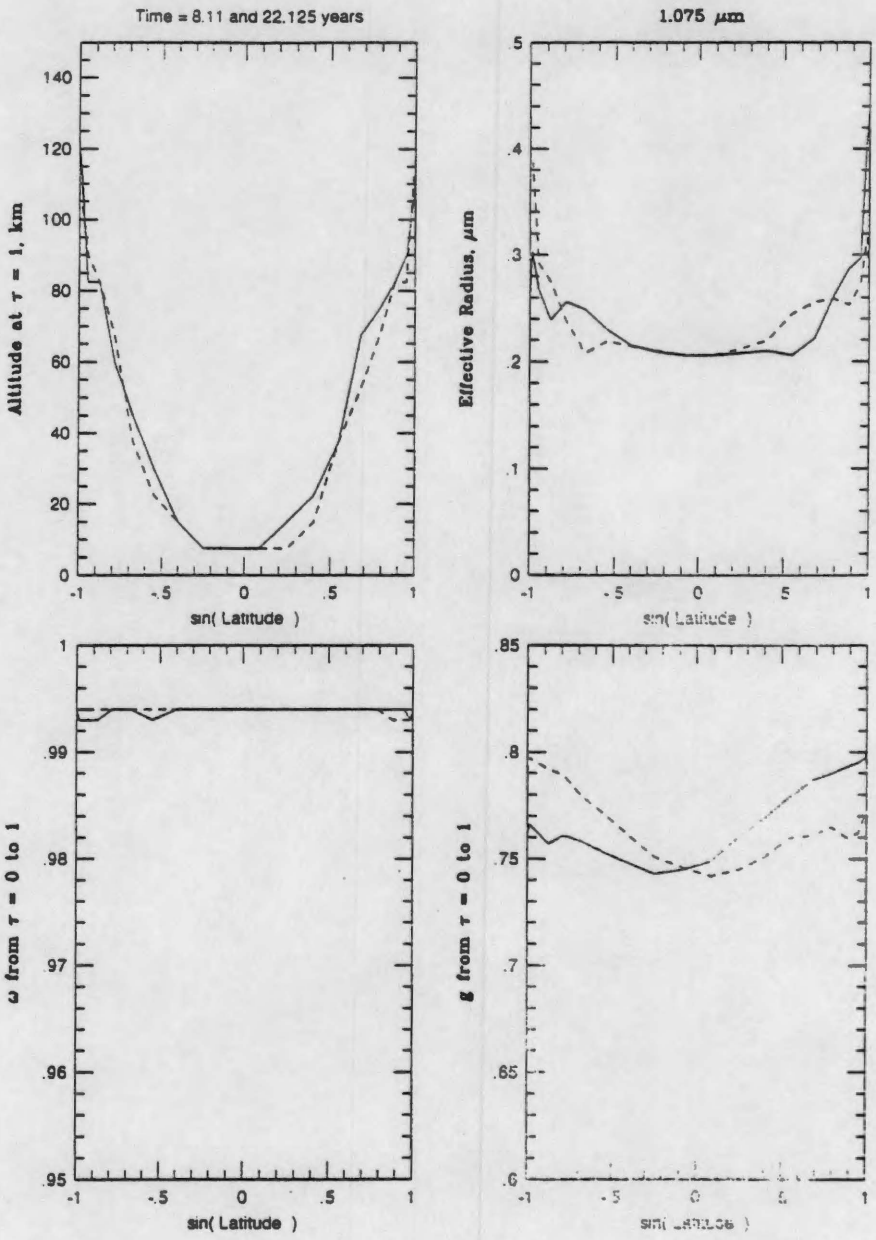
Time = 8.11 and 22.125 years
1.075 μm
Altitude at τ = 1, km
Effective Radius, μm
ω from τ = 0 to 1
g from τ = 0 to 1
sin(Latitude)
sin(Latitude)
sin(Latitude)

Figure 4.18:

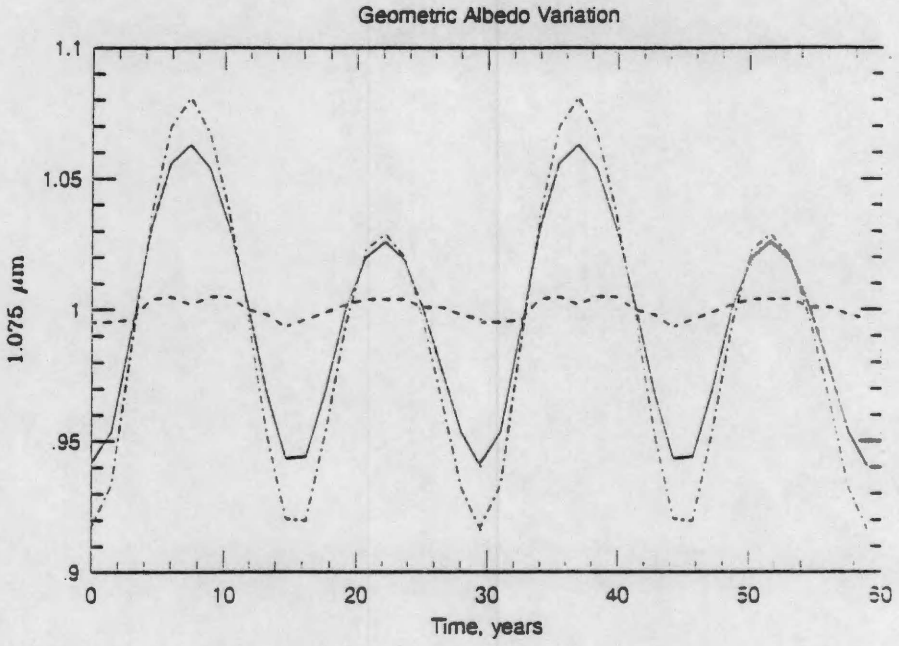
Geometric Albedo Variation
1.1
1.05
1
.95
.9
1.075 μm
0
10
20
30
40
50
60
Time, years

Figure 4.19:

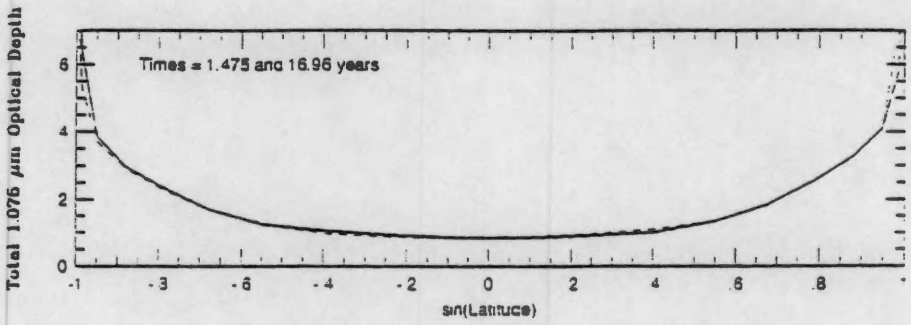
Total 1.076 μm Optical Depth
Times = 1.475 and 16.96 years
6
4
2
0
-1
-.8
-.6
-.4
-.2
0
.2
.4
.6
.8
sin(Latitude)

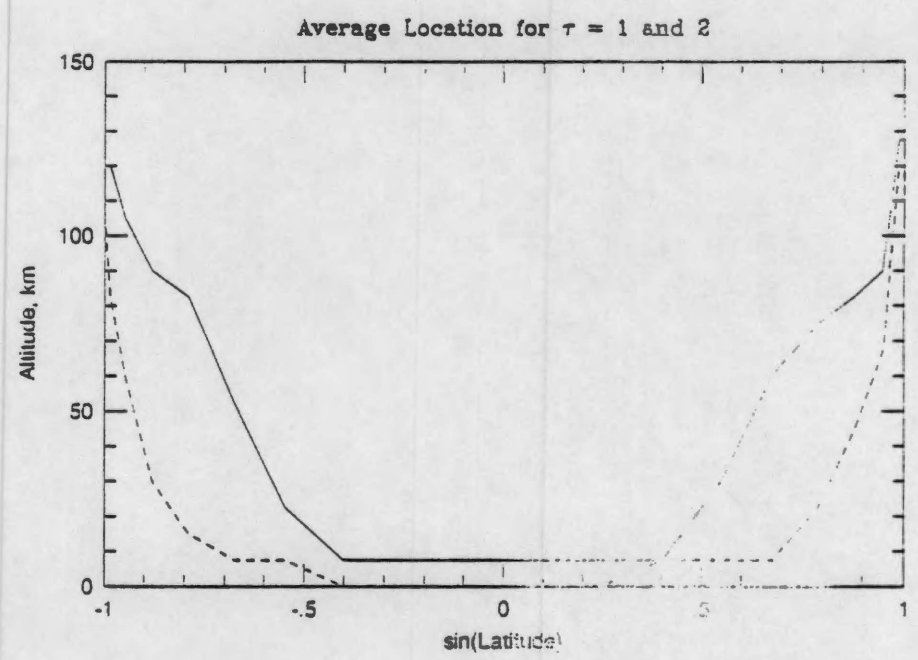
Average Location for τ = 1 and 2
150
100
50
0
Altitude, km
-1
-.5
0
1
sin(Latitude)

Figure 4.20:

Bibliography

[1] Allen, M., J. P. Pinto. and Y. L. Yung. Titan: Aerosol Photochemistry and Variations Related to the Sunspot Cycle. *The Astrophysical Journal.* 242:L125–L128. 1980.

[2] Borucki, W. J., Z. Levin, R. C. Whitten, R. G. Keesee, L. A. Capone. A. L. Summers, O. B. Toon. and J. Dubach. Predictions of the Electric Conductivity and Charging of the Aerosols in Titan's Atomsphere. *Icarus*, 72:604–622. 1987.

[3] Caldwell, J., C. C. Cunningham, D. Anthony, H. P. White, E. J. Groth. H. Hasan, K. Noll, P. H. Smith, M. G. Tomasko. and H. A. Weaver. Titan: Evidence for Seasonal Change-A Comparison of Hubble Space Telescope and Voyager Images. *Icarus*, 97:1–9, 1992.

[4] Chassefiere, E. and M. Cabane. Stratospheric Depletion of CO on Titan. *Geophys. Res. Lett.*, 18:467–470, 1991.

[5] Conrath, B. J. Thermal Structure and Meteorology of Titan. In *The Atmospheres of Saturn and Titan, ESA SP-241*, pages 89–94, Alpbach, Austria, 1985. European Space Agency.

[6] Courtin, R. Titan's UV Albedo and Modeling. In *Proceedings Symposium on Titan, ESA SP-338*, pages 59–67, Toulouse, France, 1991. European Space Agency.

[7] Courtin, R. R., R. Wagener, C. P. McKay, J. Cadwell, K. Fricke, F. Raulin, and P. Bruston. UV Spectroscopy of Titan's Atmophere, Planetary Organic Chemistry, and Prebiological Synthesis II: Interpertation of the New IUE Observations in the 220-235 nm Range. *Icarus*, 90:43–56, 1991.

[8] Cunningham, C. C., J. J. Cadwell, H. P. White, and D. M. Anthony. Evidence for Seasonal Changes on Titan. *Bull. Amer. Astr. Soc.*, 23:1187–1188, 1991.

[9] Del Genio, A. D., W. Zhou, and T. P. Eichler. Equatorial Superrotation in a Slowly Rotating GCM: Implications for Titan and Venus. *Icarus*, 101:1–17, 1993.

[10] Dlugach, J. M. and E. G. Yanoviskij. The Optical Properties of Venus and the Jovian Planets. Methods and Results of the Intensity of Radiation Diffusely Reflected from Semi-infinite Homogeneous Atmospheres. *Icarus*, 22:66–84, 1974.

[11] Dunkerton, T. J. Nonlinear Hadley Circulation Driven by Asymmetric Differential Heating. *J. Atmos. Sci.*, 46:956–974, 1988.

[12] Fink, U. and H. Larson. The Infrared Spectra of Uranus, Neptune, and Titan from 0.8 to 2.5 microns. *Astrophys. J.*, 233:693–698, 1979.

[13] Flasar, F. M. and B. J. Conrath. Titan's Stratospheric Temperatures: A Case for Dynamical Inertia. *Icarus*, 85:346–354, 1990.

[14] Flasar, F. M. and B. J. Conrath. The Meteorology of Titan. In *Proceedings Symposium on Titan, ESA SP-338*, pages 89–99, Toulouse, France, 1991. European Space Agency.

[15] Flasar, F. M., R. E. Samuelson, and B. J. Conrath. Titan's Atmosphere: Temperature and Dynamics. *Nature*, 292:693–698, 1981.

[16] Gautier, D. The Composition of the Titan. In *The Atmospheres of Saturn and Titan, ESA SP-241*, pages 75–81, Alpbach, Austria, 1985. European Space Agency.

[17] Golitsyn, G. S. Another Look at the Atmospheric Dynamics on Titan and Some of Its General Consequences. *Icarus*, pages 70–75, 1975.

[18] Griffith, C. A., T. Owen, R. Wagner, and C. Sagan. Investigation of Titan's Tropopause and Surface with Ground- Based, Near-Infrared Observations. *Icarus*, 94:57–73, 1992.

[19] Haberman, R. *Elementary Applied Partial Differential Equations with Fourier Series and Boundary Value Problems.* Prentice Hall, 1983.

[20] Hassen, J. E. and L. A. Travis. Light Scattering in Planetary Atmosphere. *Space Science Reviews*, 16:527–610, 1974.

[21] Held, I. M. and A. Y. Hou. Nonlinear Axially Symmetric Circulation in a Nearly Inviscid Atmosphere. *JAS*, 37:515–533, 1979.

[22] Held, I. M. and A. Y. Hou. Nonlinear Axially Symmetric Circulation in a Nearly Inviscid Atmosphere. *J. Atmo. Sci*, 37:515–533, 1980.

[23] Houghton, J. T. *The Physics of Atmospheres.* Cambridge University Press, second edition, 1986.

[24] Hourdin, F., O. Le Van, O.Talagrand, R.Courtin, D. Gautier, and C. P. McKay. Numerical Simulation of the Circulation of the Atmosphere of Titan. In *Proceedings Symposium on Titan, ESA SP-338*, pages 101–106, Toulouse, France, 1991. European Space Agency.

[25] Hubbard, W. B. and et al. The Occulation of Sgr 28 by Titan. *Astronomy and Astrophysics*, 269:541–563, 1993.

[26] Hubbard, W. B.. D. M. Hunten, H. J. Reitsema, N. Brosch, Y. Nevoa, E. Carreira. F. Rossi, and L. H. Wasserman. Results for Titan's Atmosphere from Its Occulation of 28 Sagittarii. *Nature*. 343:353–355, 1990.

[27] Hunten, D. M. *Saturn*, chapter Titan, pages 671–759. University of Arizona Press, 1985.

[28] Hutzell, W. T., W. L. Chameides, and C. P. McKay. Seasonal Variations in Titan's Stratospheric Haze and Albedo. *Bull. Amer. Astr. Soc.*. 23:1185, 1991.

[29] Hutzell, W. T., C. P. McKay, and O. B. Toon. Effects of a Time Varying Production Rate on Titan's Geometric Albedo. *Bull. Amer. Astr. Soc.*. 24:947, 1992.

[30] Hutzell. W. T., C. P. McKay, and O. B. Toon. Effects of Time-Varying Haze Production on Titan's Geometric Albedo. *Icarus*, 105:162–174, 1993.

[31] Hutzell, W. T., C. P. McKay, and O. B. Toon. Two Dimensional Modeling of Titan's Stratospheric Haze. *Bull. Amer. Astr. Soc.*, 25:1109. 1993.

[32] Khare, B. N., C. Sagan, E. T. Arakawa, F. Suits, T. A. Callcott, and M. W. Williams. Optical Constants of Organic Tholins Produced in a

Simulated Titanian Atmoshpere: From Soft X-ray to Microwave Frequencies. *Icarus*, 60:127–137, 1984.

[33] Lellouch,E. A., A. Coutenis, F. Raulin, N. Duboule, and C. Frere. Titan's Atmosphere and Hypothesized Ocean: A Reanalysis of Voyager 1 Radio-Occultation and IRIS 7.7 micron Data. *Icarus*, 79:328–349, 1989.

[34] Leovy, C. Simple Model of Thermally Driven Mesospheric Circulation. *J. Atmos. Sci.*, 21:327–341, 1964.

[35] Leovy, C. B. and J. B. Pollack. A First Look at the Dynamics and Temperature Variations on Titan. *Icarus*, 19:195–201, 1973.

[36] Lockwood, G. W. Secular Brightness Increase of Titan. Uranus, and Neptune, 1972-1976. *Icarus*, 32:413–430, 1977.

[37] Lockwood, G. W., B. L. Lutz, D. T. Thompson, and E. S. Bus. The Albedo of Titan. *Astrophys. J.*, 303:511–520, 1986.

[38] Lockwood, G. W. and D. T. Thompson. A Relationship Between Solar Activity and Planetary Albedos. *Nature*, 280:43–45, 1979.

[39] Lunine, J. I., J. Steveson, and Y. L. Yung. Ethane Ocean on Titan. *Science*, 222:1229–1230, 1983.

[40] McKay, C. P., J. B. Pollack, and R. Courtin. The Thermal Structure of Titan's Atmosphere. *Icarus*, 80:23–53, 1989.

[41] McKay, C. P., J. B. Pollack, R. Courtin, and J. L. Lunine. The Atmospheric Temperature Structure of Titan. In *Proceedings Symposium on Titan, ESA SP-338*, pages 77–80, Toulouse, France, 1991. European Space Agency.

[42] McKay, C. P., J. B. Pollack, R. Courtin, and J.L. Lunine. The Greenhouse and Antigreenhouse Effects on Titan. *Science*, 253:1118–1121, 1991.

[43] Mordaunt, D. H., I. R. Lambert, G. P. Morley, M. N. R. Ashford, R. N. Dixon, and C. M. Western. Primary product channels in the photodissociation of methane at 121.6 nm. *J. Chem. Phys.*, 98:2054–2065, 1993.

[44] Neff, J. S., D. C. Humm, J. T. Bergstralh, A. L. Cochran, E. S. Barker, and R. G. Tull. Absolute Spectophotometry of Titan, Uranus, and Neptune. *Icarus*, 60:221–235, 1984.

[45] Pollack, J. B., K. Rages, O. B. Toon, and Y. L. Yung. On the Relationship between Secular Brightness Changes of Titan and Solar Variability. *Geophys. Res. Let.*, 7:829–832, 1980.

[46] Rages, K. and J. B. Pollack. Titan Aerosols: Optical Properties and Verticle Distirbution. *Icarus*, 55:50–62, 1983.

[47] Samuelson, R. E. Radiative Equilibrium Model of Titan's Atmosphere. *Icarus*, 53:364–387, 1983.

[48] Scattergood, T. W. and et al. Titan's Organic Haze over the Last Four Billion Years. *Bull. Amer. Astron. Soc.*, 20:842, 1988.

[49] Smith, B. A., L. Soderblom, R. Beebe, J. Boyce, G. Briggs, A. Bunker, S. A. Collins, C. J. Hansen, T. V. Johnson, J. L. Mitchell, R. J. Terrile, M. Carr, A. F. Cook II, J. Cuzzi, J. B. Pollack, G. E. Danielson, A. Ingersoll, N. E. Davies, G. E. Hunt, H. Masursky, E. Shoemaker, D. Morrison, T. Owen, C. Sagan, J. Veverka, R. Strom, and V. E. Suomi. Encounter with Saturn: Voyager 1 Imaging Science Results. *Science*, 212:163–190, 1981.

[50] Sromovsky, L. A. and P. M. Fry. The Phase Variation of Titan's Brightness Contrast: Implied Constraints on the Properties of the Haze Particles. *Bull. Amer. Astron. Soc.*, 20:842, 1989.

[51] Sromovsky, L. A., V. E. Suomi, J. B. Pollack, R. J. Krauss, S. S. Limaye, T. Owen, H. E. Revercomb. and C. Sagan. Implications of Titan's North-South Brightness Asymmetry. *Nature*, 292:698–702, 1981.

[52] Strobel, D. F., M. E. Summers, and X. Zhu. Titan's Upper Atmosphere: Structure and Ultravoilet Emissions. *Icarus*, 103:512–526, 1992.

[53] Thompson, W. R., T. J. Henry, J. M. Schwartz. B. N. Khare, and C. Sagan. Plasma Discharge in N_2+CH_4 at Low Pressures: Experimental Results and Applicatrions to Titan. *Icarus*, 93:57–73. 1991.

[54] Toon, O. B., C. P. McKay. R. Courtin, and T. P. Ackermen. Methane Rain on Titan. *Icarus*, 75:255–284, 1988.

[55] Toon, O. B., C. P. McKay. C. A. Griffith, and R. P. Turco. A Physical Model of Titan's Aerosol. *Icarus*, 95:24–53, 1992.

[56] Toon, O. B., R. P. Turco, and J. B. Pollack. A Physical Model of Titan's Cloud. *Icarus*, 43:260–282. 1980.

[57] Toon, O. B., R. P. Turco, D. Westphal, R. Malone, and M. S. Liu. A Multidimensional Model for Aerosols: Description of Computational Analogs. *J. Atmos. Sci.*, 45:2123–2143, 1988.

[58] Toublanc, D., J. P. Parisot, J. Brillet, D. Gautier, F. Raulin, and C. P. McKay. Photochemical Modeling of Titan's Atmosphere. *Icarus*, Submitted:x–xx, 1994.

[59] Yung, Y. L. An Update of Nitrile Photochemistry on Titan. *Icarus*, 72:468–472, 1987.

[60] Yung, Y. L., M. Allen. and J. P. Pinto. Photochemistry of the Atmosphere of Titan: Comparison between Model and Observations. *Astropys. J. Supp. Ser.*, 55:465–506, 1984.

ICARUS 105, 162–174 (1993)

APPENDIX I

Effects of Time-Varying Haze Production on Titan's Geometric Albedo

WILLIAM T. HUTZELL[1]

School of Earth and Atmospheric Sciences, Georgia Institute of Technology, Atlanta, Georgia 30332-0340

AND

CHRISTOPHER P. MCKAY AND OWEN B. TOON

NASA Ames Research Center, Mail Stop 245-3, Moffett Field, California 94035-1000

Received September 14, 1992; revised June 18, 1993

Two versions of the Toon *et al.* (1992, *Icarus* 95, 24–53) Titan haze model were used to simulate the observed blue and yellow geometric albedo variations using a time-dependent haze production. Steady-state calculations were used to suggest that the range of production rate changes necessary to explain the observations was a factor of between 2 and 4. However, the blue and yellow geometric albedo variations were about 10 times smaller than the observations, when computed with a time-varying production rate with this same range. Long haze residence times were the cause of this decreased response. This result was insensitive to the details of the functional representation of the production. In addition to the amplitude of the geometric albedo, we found that the phase between albedo response and the production forcing is a critical discriminate when comparing model results to the observations. Long haze time scales also produced a phase delay in the albedo response to seasonal solar forcing which can agree with the observations (Sromovsky *et al.* 1981, *Nature* 292, 698–702). Unfortunately, the size of the phase delay was dependent on model parameters. We found that raising the level of rainout well into the stratosphere (90 km) decreased the residence time of the haze and allowed us to fit the magnitude of the albedo variation. However, the resulting phase delay (−60°) was not in agreement with observations (+90°) and such a high altitude for rainout is probably unphysical. Our results suggest that a time-varying mass production cannot explain Titan's geometric albedo variations.

INTRODUCTION

Over the past 2 decades, the geometric albedo of Titan has undergone small variations. The maximum to minimum variation was 10 ± 1.3 and 7 ± 1.3% for blue (0.47 μm) and yellow (0.55 μm), respectively (Lockwood 1977, Lockwood and Thompson 1979, Lockwood *et al.* 1986). Although part of Titan's geometric albedo variations may be explained by the solar UV cycle (Pollack *et al.* 1980), most of the variations are explained by invoking sinusoidal time variations of the observed northern–southern hemispheric brightness contrast (Sromovsky *et al.* 1981). The northern–southern hemispheric brightness contrast was first observed during the Voyager I flyby, when the contrast was probably at a maximum based on Earth-based observations. The size of the hemispheric brightness contrast is approximately double the geometric albedo variations reported by Lockwood *et al.* (1986), because Earth-based viewing of Titan is an integrated combination of northern and southern hemispheres. The integration depends on the orientation of Titan with respect to the Earth (Fig. 1) and reduces possible geometric albedo variations. The resultant geometric albedo also has a different time dependence than either hemispheres' brightness. An analytical model for the time variation of the geometric albedo, $P(t)$, which accounts for 50 to 70% of the observations (Fig. 1) and is given by

$$P(t) = P_1(1 + a_1\sin(\omega_p t)), \quad (1)$$

where P_1 is the average albedo, a_1 is the amplitude of oscillation, and ω_p is the angular frequency ($2\pi/13.8$ year^{-1}) (Smith *et al.* 1981). The value of a_1 is a multiple of the observed contrast and a weighting factor which is determined by hemispheric viewing. The value of ω_p does not correspond to one-half of Saturn's period (14.75 years) because of the eccentricity of Saturn's orbit (Smith *et al.* 1981, Sromovsky *et al.* 1981). Zero time corresponds to 1973.3 which is determined by the albedo maximum in

[1] Presently on fellowship at NASA Ames Research Center.

0019-1035/93 $5.00

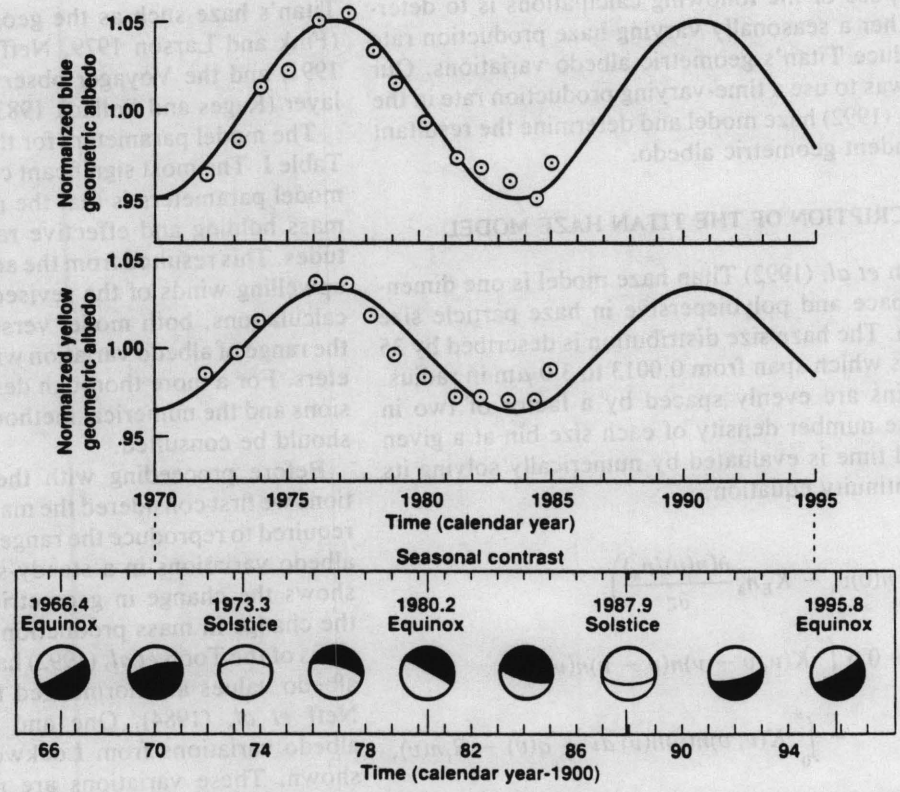

FIG. 1. The observed (Lockwood *et al.* 1986) points, and predicted (solid line) geometric albedo variations plotted with respect to time. The lowest panel (from Sromovsky *et al.* 1981) illustrates the seasonal model of the northern–southern hemispheric brightness contrast.

1976. The value of a_1 is one-half the albedo variation reported by Lockwood *et al.* (1986).

The component of the geometric albedo variations driven by hemispheric brightness contrast is forced by seasonal effects which result from Saturn's obliquity (=27°). For the seasonal component of the brightness variations, a 90° phase delay is required between hemispheric response and the seasonal solar forcing, because the maximum contrast was observed during northern spring equinox. The hemispheric brightness contrast has been observed by the Hubble Space Telescope and is consistent with the predictions of the seasonal model; 120° after the Voyager flybys (Caldwell *et al.* 1992).

Seasonal variations in Titan's stratospheric haze are believed to be the source of Titan's hemispheric brightness variations because the haze has sufficient opacity to control the visible geometric albedo (Sromovsky *et al.* 1981). Titan's stratospheric haze is produced by the condensation and coagulation of photochemical products which are generated by the dissociation of CH_4 and N_2 by solar radiation and energetic electrons. Hemispheric asymmetries of haze distribution are suggested by recent occultation observations of Titan (Hubbard *et al.* 1990, 1993), but their exact nature and cause remain uncertain.

Pollack *et al.* (1980) proposed that the time variations in the geometric albedo were produced by changes in the global haze production driven by the solar UV cycle. In the Pollack *et al.* (1980) model, the geometric albedo changes were produced by changing the altitude of optical depth unity. Increasing the haze production rate raised this altitude and puts particles of smaller sizes at optical depth unity. The smaller particles decreased the geometric albedo because of their decreased backscattering. Decreasing the haze production rate produced the reverse effect. (It is important to note that these changes were from changes of optical depth profile and not from changes in particle size at a given altitude.) A haze production variation by a factor of two was determined to be sufficient to explain the visible geometric albedo variations. The haze model used by Pollack *et al.* (1980) requires updating because it was based on pre-Voyager atmospheric composition, temperature, and pressure profiles (Toon *et al.* 1980). In addition, the calculations of Pollack *et al.* (1980) were based on a steady-state model and did not take into consideration time-dependent effects. An accurate version of this Titan haze model was used in Toon *et al.* (1992), but the new model has not been previously used to reevaluate the Pollack *et al.* (1980) conclusions.

The purpose of the following calculations is to determine whether a seasonally varying haze production rate can reproduce Titan's geometric albedo variations. Our approach was to use a time-varying production rate in the Toon *et al.* (1992) haze model and determine the resultant time-dependent geometric albedo.

DESCRIPTION OF THE TITAN HAZE MODEL

The Toon *et al.* (1992) Titan haze model is one dimensional in space and polydispersive in haze particle size distribution. The haze size distribution is described by 35 volume bins which span from 0.0013 to 3.0 μm in radius. The size bins are evenly spaced by a factor of two in volume. The number density of each size bin at a given altitude and time is evaluated by numerically solving its number continuity equation,

$$\frac{\partial n(v)}{\partial t} = \frac{\partial}{\partial z}\left(n(v)v_s - K_E n_a \frac{\partial(n(v)/n_a)}{\partial z}\right) + 0.5\int_0^v K(\nu, v-\nu)n(v-\nu)n(\nu)\,d\nu - \int_0^\infty K(\nu, v)n(v)n(\nu)\,d\nu + q(v) - R_r n(v),$$

where $n(v)$ is the number density of volume v particles, v_s is the particle sedimentation velocity, K_E is the vertical eddy diffusion coefficient, n_a is the atmospheric number density, K is the Brownian coagulation coefficient, $q(v)$ is the mass production rate, and R_r is the rainout constant. There are 35 coupled equations, which determine the haze structure.

The haze model attempts to simulate an aerosol layer which is produced at high altitudes from photochemistry. For the steady-state calculations, the haze production profile and column production rate are constant with respect to time. Haze material is generated only in the smallest size bin and then coagulates into larger particles and sediments. For the microphysical processes, the haze particles are assumed to be spherical. The Brownian coagulation coefficient includes an electrostatic repulsion from particle charging (Borucki *et al.* 1987). Haze transport also includes eddy diffusion. The haze particles can be removed by rainout which simulates the condensation at the tropopause of methane and photochemical products onto the haze particles. Two versions of the haze model are used and are referred to as the conventional and the revised models in Toon *et al.* (1992). The conventional model simulates Titan's haze by using model parameters which were determined by previous simulations of Titan's atmosphere. The revised model adjusted the model parameters to better fit observations which are related to Titan's haze such as the geometric albedo observations (Fink and Larson 1979, Neff *et al.* 1984, Courtin *et al.* 1991) and the Voyager observations of a detached haze layer (Rages and Pollack 1983).

The model parameters for the two versions are listed in Table I. The most significant consequence of the differing model parameters is that the revised version had greater mass holding and effective radius values at higher altitudes. This resulted from the aerosol charging scheme and upwelling winds of the revised version. In the following calculations, both model versions were used to explore the range of albedo variation with respect to model parameters. For a more thorough description of the model versions and the numerical methods, Toon *et al.* (1988, 1992) should be consulted.

Before proceeding with the time-dependent calculations we first considered the mass production rate changes required to reproduce the range of the observed geometric albedo variations in a steady-state calculation. Figure 2 shows the change in geometric albedo as a function of the change in mass production rate for steady-state versions of the Toon *et al.* (1992) haze models. The geometric albedo values are normalized to the values reported by Neff *et al.* (1984). One and two times the observed albedo variations from Lockwood *et al.* (1986) are also shown. These variations are not centered about unity because the Neff *et al.* (1984) data were taken at $\approx$1981.38 and are not the average values of the time-varying albedo. We considered effects twice that reported by Lockwood *et al.* (1986) because the model calculations refer to observing the northern or southern hemisphere separately. The ratio of maximum to minimum production rates, γ, required to explain the observations was found to be approximately 2 to 4. The upper limit of γ was less well defined, because of the differing albedo curves at high production rates. For this range of γ values, the spectral dependence of the computed albedo variation approximately agreed with the observations (Table II).

Haze production variations cannot be directly evaluated by present photochemical models (Yung *et al.* 1984, Yung 1987), because the heavier organics were not included. A possible guide to haze production variations is the seasonal variation of solar flux. From geometric considerations, the ratio of the hemispheric average daily solar flux between summer and winter hemispheres is approximately four. Allen *et al.* (1980) predicted a haze production variation of a factor of four with a factor of four variation in the UV photon flux from sunspot activity. However, their model did not include nitrogen compounds and they were modeling production changes from globally averaged solar UV flux, while the seasonal changes of solar flux are over all wavelengths and depends on latitude. Nevertheless, a factor of 2 to 4 seems to be

TABLE I
Toon *et al.* (1992) Titan Haze Model Parameters

Parameter	Haze model versions from Toon *et al.* (1992)		Parameter variation in time-dependent calculations for each version
	Conventional model	Revised model	
T, P profile	Lellouch *et al.* (1989)	Lellouch *et al.* (1989)	—
Mass production profile	66% Above 300 km	3% Above 300 km	—
Column mass production, rate (g cm^{-2} sec^{-1})	1.225×10^{-14}	1.225×10^{-14}	5.5×10^{-15} to 4.4×10^{-14}
Maximum to minimum production ratio			
Eddy diffusion (cm^2 sec^{-1})	1	1	2 to 1000
Multiple of Toon *et al.* (1992)	1	1	0 to 100
Structure of profile	Toon *et al.* (1992) Profiles		Toon *et al.* (1992) Profiles to constant 1×10^8
Vertical air velocity (cm sec^{-1})	0	1.0 Between 320 and 430 km	—
Particle density (g cm^{-3})	1	1	1 to 4
Coagulation efficiency by aerosol charging	Borucki *et al.* (1987) charging	No charge above 300 km 3 × Borucki *et al.* (1987) below 300 km	0 to 10 × Borucki *et al.* (1987) above 300 km 0 to 10 × Borucki *et al.* (1987) below 300 km
Rainout time (years)	1	0	0 to 1
Upper rainout boundary (km)	30	0	0 to 90

within the range of attainable seasonal haze production variations.

It is not possible to infer the phase behavior of a time-dependent model from the steady-state results. In the steady-state calculations, an inverse relationship exists between the albedo and a constant production rate, but a time-dependent model can skew the above relationship due to slow response time (Sromovsky *et al.* 1981, Hutzell *et al.* 1991).

TIME-VARYING CALCULATIONS

Method. To perform time-dependent calculations we have imposed a time-varying production rate in the model. The functional form of the time-varying production rate was arbitrary. Our only constraints were the phase and period of production. The production was chosen to instantaneously follow the seasonal solar forcing which varies at the angular frequency of Saturn's orbit ($2\pi/29.5$ $years^{-1}$). An amplitude given by an exponential of a sine function (see Fig. 3) was selected for two reasons; production smoothly varies over time, and the selected value of γ can be greater than one.

The time-dependent haze structure was computed until cyclic over a 29.5-year period, ≈750 years of time integration. To better determine the resultant haze structure variations the model was changed in two ways from Toon *et al.* (1992). First, the time step of the numerical solution was decreased from 1.0 to 0.5 years. Second, the vertical grid spacing was decreased below 120 km altitude from 10 km to 5 km. The resulting time variations in the blue and yellow geometric albedo are shown in Fig. 3 for γ set to two and four.

In our calculations, the computed geometric albedo varied at the angular frequency of Saturn which was analogous to observing the variations of a single hemisphere. The observed geometric albedo actually varies at approximately twice the angular frequency of Saturn, because it is produced by viewing a combination of both hemispheres which are 180° out of phase. To compare the model results to the observations (Fig. 1) it is necessary to fold in this geometrical effect of ≈2.

The amplitude of the albedo variation. Table II gives the computed albedo variation (as percentage difference between the maximum and minimum) for the time-dependent model for γ values of 2 and 4, as well as the results from the steady-state calculations.

There are significant differences between these two results. The obvious change is the large reduction of the albedo variation in time-dependent modeling with respect to the steady-state prediction. The amplitude of the albedo variation with respect to the two versions of the models also disagrees. In steady-state calculations, the revised model predicted larger albedo variation than the conventional model for a given γ value, but in the time-dependent modeling, the revised model actually gave smaller albedo

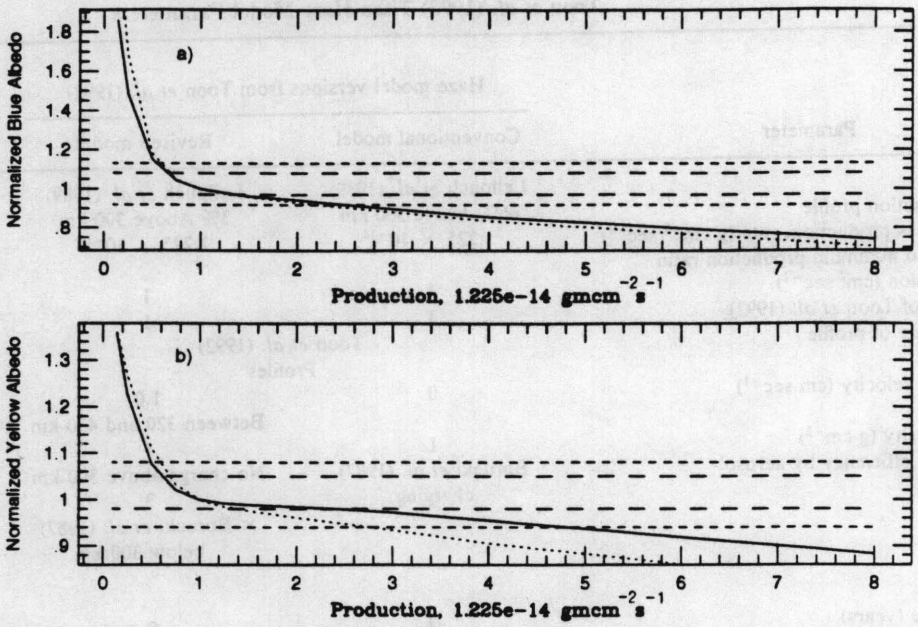

FIG. 2. The (a) blue (0.47 μm) and (b) yellow (0.55 μm) geometric albedos for the conventional model (solid line) and the revised model (dotted line) versus haze column production rate. The albedo curve is normalized to the blue albedo when the column production rate is 1.22×10^{-14} g cm^{-2} sec^{-1} (the production rate used in Toon *et al.* 1992). Each pair of horizontal lines shows one times (long dashed) to two times (short dashed) the observed range of albedo variations.

variations than the conventional model. There are also differences in the relative results of the conventional and revised models. In addition, the spectral dependence, which in the steady-state case agreed with the observations, is different when time dependence is included (see Table II).

Changing the time-dependent production rate was unsuccessful at increasing the size of the albedo variation. We considered a range of γ values from 2 to 1000 (see Table I) as well as alternate forms for the time dependence of the production variation. The alternative form was a step function with a variable step size, and allowed production to vary discontinuously over time. Neither of these changes produced large enough albedo variations or time-averaged geometric albedos which were consistent with the observations.

TABLE II
Maximum to Minimum Geometric Albedo Variation, Δ%

Color	Lockwood *et al.* (1986) observation (%)	γ	Steady-state prediction (%)	Time-dependent result (%)
		Conventional model		
Blue	10 ± 1.3	2.0	10.7	1.80
		4.0	20.2	3.84
Yellow	7 ± 1.3	2.0	4.65	2.03
		4.0	9.99	4.13
		Revised model		
Blue	10 ± 1.3	2.0	11.5	0.577
		4.0	30.9	1.30
Yellow	7 ± 1.3	2.0	7.74	0.133
		4.0	17.3	0.350

We also attempted to increase the albedo variations by changing the parameters of haze model. The range of model parameters explored are shown in Table I. The changing of no single model parameter was able to increase the size of the albedo variation and also to produce the observed time-averaged albedo, but a combination of production and transport parameters was able to accomplish this. The transport parameter which was the most successful at increasing the size of the albedo variations was raising the upper boundary where rainout occurs. The haze column production rate and the value of γ had to be simultaneously increased to agree with the observations. The revised model was the most successful for a 90-km upper rainout boundary, a haze column production rate of 2.2×10^{-14} g cm^{-2} sec^{-1}, and a γ value of 16. The physical reality of these parameter values is uncertain primarily because it would imply tropospheric-like rain processes high in the stratosphere.

Time dependence of the albedo variation. Another important aspect of the simulations is the time behavior

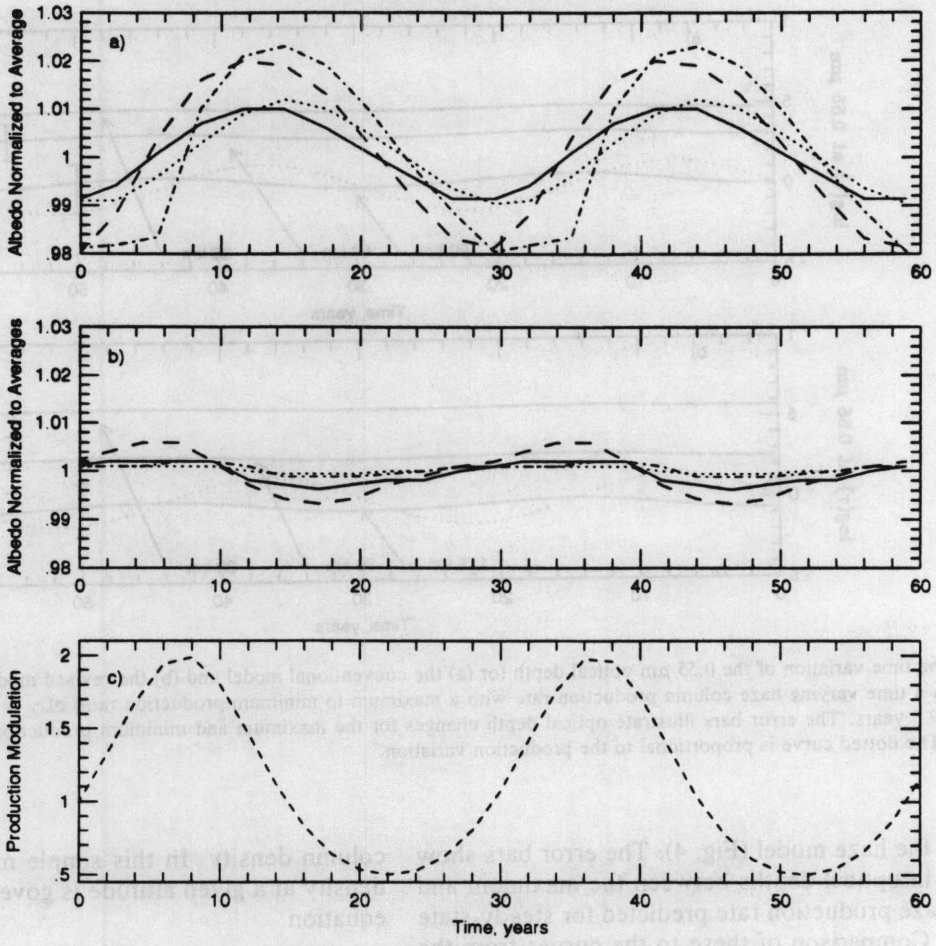

FIG. 3. The variation of blue and yellow geometric albedos versus time for (a) the time-dependent conventional model and (b) the time-dependent revised model. The time-dependent haze column production rate has a maximum to minimum production ratio of 2 or 4 and a period of 29.5 years. For $\gamma = 2$, the blue and yellow albedos are the solid and dotted lines, respectively. For $\gamma = 4$, the blue and yellow albedos are the long dashed and dash–dot lines, respectively. All albedo values are normalized to their time averages. In (c), the short dashed line shows the modulation of the production rate for $\gamma = 4$.

of the geometric albedo. The seasonal model of the hemispheric brightness contrast requires that a $+90°$ phase delay exist between the albedo and seasonal solar forcing, because we have assumed production to be in phase with the solar forcing. The conventional model's albedo variations did exhibit a $+90°$ phase delay, in agreement with the seasonal model. In the revised model, the albedo variation had a $-60°$ phase delay (or 300° behind) with respect to seasonal solar forcing in conflict with the seasonal model.

Attempts to improve the phase behavior and simultaneously the size of the computed albedo variation were unsuccessful. For the model parameter settings which produced the observed size of the albedo variation (raising the upper rainout boundary), neither model was able to produce the correct phase delay. For the revised model, there was no change in the phase delay. For the conventional model, the parameter settings changed the phase delay to a value near $-60°$. Attempts to maintain the original phase delay of the conventional model and to obtain the correct size of the computed albedo variation were unsuccessful. Therefore, a time varying production does not seem to be able to adequately explain Titan's observed albedo variation.

DISCUSSION

The reduced albedo variation. To determine why the visible albedo variation from a time-dependent production was much smaller than expected from steady-state results and why a phase delay existed between the albedo and production rate, we have plotted the time behavior of the 0.55-μm optical depth at various altitudes for both

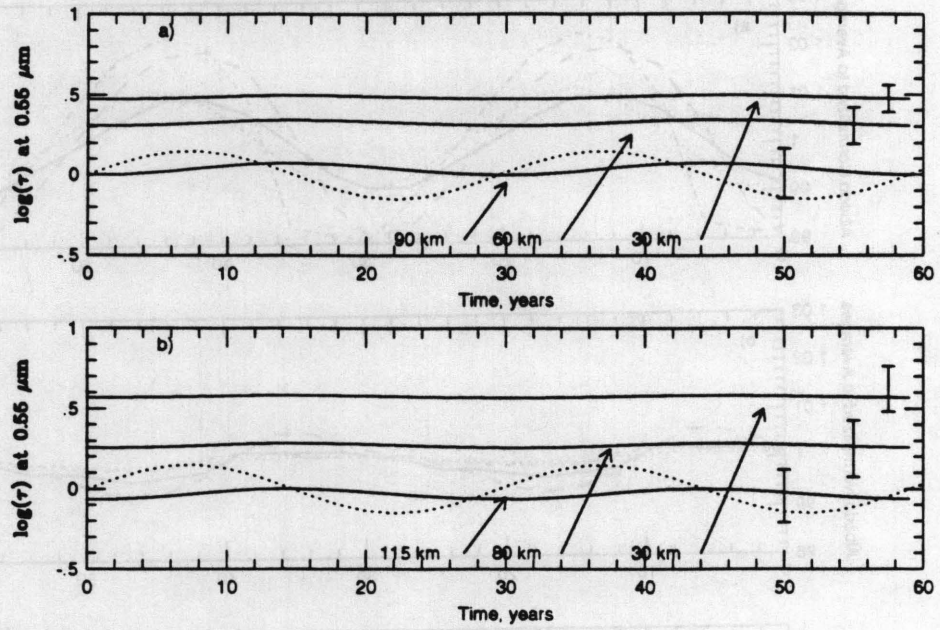

FIG. 4. The time variation of the 0.55 μm optical depth for (a) the conventional model and (b) the revised model, at selected optical depths resulting from a time varying haze column production rate with a maximum to minimum production ratio of $\gamma = 2$. The period of production variation is 29.5 years. The error bars illustrate optical depth changes for the maximum and minimum production rates from the steady-state calculations. The dotted curve is proportional to the production variation.

versions of the haze model (Fig. 4). The error bars show the change in optical depths between the maximum and minimum haze production rate predicted for steady-state conditions. Comparison of these to the curves from the time-dependent models illustrates the most probable reason for the reduced albedo variation. In the steady-state case the variations of the optical depths with respect to production variations were much greater than in the time-dependent calculations at the optical depths which primarily determine the albedo.

In the steady-state calculations, the change of optical depth at lower altitudes for the maximum and minimum albedo, was greater in the revised model (Fig. 4b) than in the conventional model (Fig. 4a). Consequently, the geometric albedo variations of the revised model were more reduced than the conventional model (as seen in Table II).

Analytical model. A simple analytical model illustrates why the optical depth at those altitudes behaves in this manner. To construct the analytical model, we assumed that the optical depth at an altitude, z, is dependent on the haze mass column density at z, $m(z)$,

$$m(z) = \int_z^\infty \rho_h(z)\, dz, \tag{1}$$

where $\rho_h(z)$ is the haze mass holding at z. Therefore, the optical depth changes with time in proportion to the column density. In this simple model, the haze column density at a given altitude is governed by the differential equation

$$\frac{dm(z)}{dt} = -\frac{m(z)}{\phi} + A(1 + a\sin(\omega t)), \tag{2}$$

where ϕ is the haze material residence time above z. The value of ϕ is approximately the time averaged haze column density at z divided by the sedimentation flux at z. The second term on the right-hand side is the time varying haze column production rate with an amplitude, A, and an amplitude of variation, a. The above equation's particular solution is

$$m(z) = A\phi + \frac{Aa\sin(\omega t - \delta)}{\sqrt{\omega^2 + (1/\phi)^2}}, \tag{3}$$

where δ is the phase delay,

$$\delta = \arctan(\omega\phi). \tag{4}$$

Because the residence time for a majority of Titan's haze material is greater than several decades and ω is the angular frequency of Saturn, the $m(z)$ and optical depth values, which mostly determine the geometric albedo,

reduce to the limit of $\omega \gg 1/\phi$. Hence, $m(z)$ and optical depth converge to the expression

$$m(z) = A\left(\phi - \frac{a\cos(\omega t)}{\omega}\right). \quad (5)$$

There are two consequences at these limits: (1) the phase of $m(z)$ (and optical depth) is 90° behind the forcing column production rate; and (2) the amplitude of variation is inversely related to forcing frequency. Most significant optical depths in both time-dependent haze models behaved approximately in this manner (i.e., $\omega \gg 1/\phi$ for $\tau \gtrsim 1$). Therefore, long residence times prevented the predicted albedo changes, because the predicted optical depth changes implied by the steady-state calculations cannot occur with a realistic time-varying production rate.

If the above analytical models and numerical haze models are consistent with the predictions for the steady-state case, the time variation of the optical depth profile and the geometric albedo will go to the time independent modeling predictions in the limit of $\omega \ll 1/\phi$. The actual cause of the haze production time variations cannot have such long periods, because the only possible forcing periods are 29.5 years or less which correspond to the seasonal or solar cycles. In the limit $\omega \ll 1/\phi$, the analytical model is approximated by

$$m(z) = A\phi(1 + a\sin(\omega t)). \quad (6)$$

Equation (7) converges to the steady-state predictions because the time variation's amplitude is determined by ϕ and the variation is in phase with the forcing. The equivalent of Fig. 4 with a 1000-year forcing period (Fig. 5) shows that the time behavior of the optical depth is much closer to the steady-state case which also agrees with the analytical model. The variations of the blue and yellow albedo versus forcing period (Fig. 6) show convergence to the steady-state calculations with increasing forcing period.

Phase delay. Turning to the time dependence of the visible albedo, the revised model's visible albedo time behavior can be explained by considering time independent modeling at different production rates which showed an inverse relationship between production and the visible albedo. (Pollack *et al.* 1980, Toon *et al.* 1980, 1992, McKay *et al.* 1989). (Higher haze production rates lowered the albedo by burying the bright Rayleigh scattering gas beneath the dark haze material and by changing the particle size at optical depth unity toward smaller radii which have lower backscattering cross sections. Both of these effects were consequences of higher haze mass column densities which were produced by higher production rates.) In the context of our simple analytic model, the visible albedo variations will then have a phase delay of $\delta - 180°$ and will be between $-180°$ and $-90°$. Large haze time scales will cause a phase delay between the albedo and production variations near $-90°$. A larger delay than predicted by the simple analytic model can arise for two reasons: (1) nonuniform responses to production though the haze and (2) the time variation of other albedo-determining quantities such as the effective particle radius. For the time-dependent revised model, the visible albedo delay was $-60°$ (close to the predicted range) but the time-dependent conventional model had a visible albedo phase delay near $+90°$ which is not close to $\delta - 180°$. Clearly, the phase delay of the conventional model is not in line with the analytical model.

The difference of the phase response between the revised and conventional models can be understood in terms of the size variations of the haze particle which were close to optical depth unity. In the conventional model, the haze particles near this region were relatively small and had short formation time scales relative to the period of production variations. While for the revised model, the particle sizes near this region were large and had long formation time scales relative to the period of production variations. Consequently for the conventional model, the particle size variations near optical depth unity were larger and more rapidly responded to production changes, in contrast to the revised model (Fig. 7). These particle variations turned out to have a significant effect on the opacity structure and the geometric albedo. (The significant particle size variations also caused the different spectral dependence of the albedo between the time-dependent and steady-state conventional model (see Table II).) Hence, the analytical model is too simple to properly represent the conventional model's phase delay, because two of the assumptions of the analytical model break down: (1) $\omega \gg 1/\phi$ at all significant optical depths; and (2) the particle size variations were negligible.

For the time-dependent conventional model, the phase relationship between albedo and production variations was in agreement with observations (Sromovsky *et al.* 1981), if production is in phase with seasonal solar forcing. The spring hemispheric albedo (haze production is increasing from the average value) was lower than the fall hemispheric albedo. Unfortunately, the albedo variation was smaller than observed, because the seasonal changes of the model's optical depth profile and haze particle sizes were smaller than found in the steady-state calculations.

As with the amplitude of the albedo response, the phase response for both models went to the values determined in the steady-state case at long forcing periods ($-180°$).

Effects of changing model parameters. The change of model parameters which increased the size of the albedo variation can be roughly understood in terms of our simple analytical model. The amplitude of the albedo variation

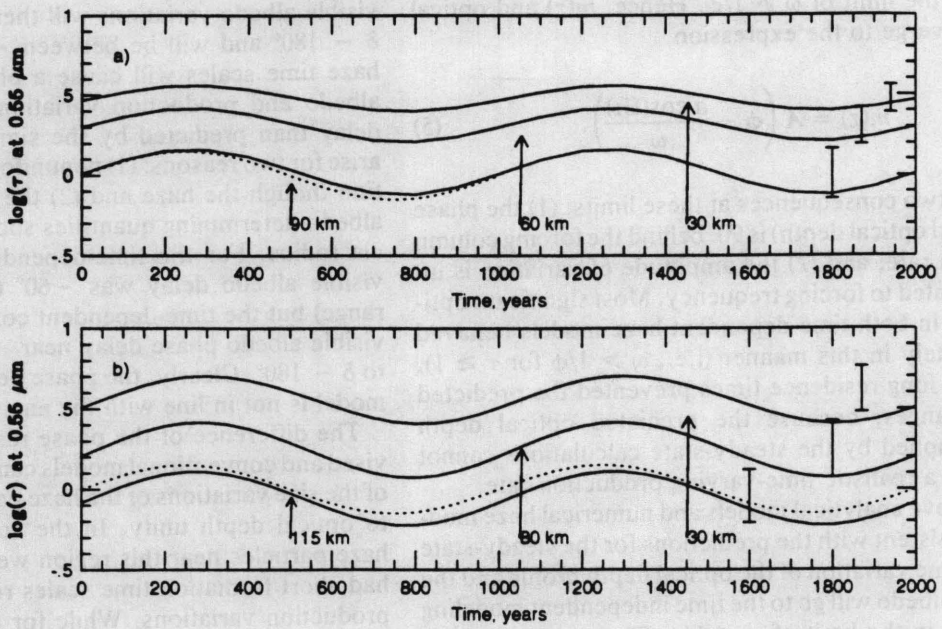

FIG. 5. Same as Fig. 4 but the period of production variation set at 1000 years. Note, the response is similar to the steady-state predictions and is in phase with the production, in contrast to Fig. 4.

can be increased by decreasing the haze material residence time scales. Increasing haze material removal processes is a method of accomplishing this. The three removal processes of our haze model are sedimentation, rainout, and diffusion. To remain consistent with the observations, sedimentation and rainout are the best potential candidates, because diffusion tends to mix haze material uniformly over the entire spatial extent of the haze layer. Sedimentation can also be eliminated, because the sedimentation parameter, the particle density, is required to be at physically unrealistic values ($\geqslant 4$ g cm^{-3}). Rainout is therefore the only plausible candidate. Raising the rainout boundary increased the size of the computed albedo variation and reduced the spatial extent of the haze material. The net haze material residence time was thereby reduced by concentrating a majority of the haze material to an atmospheric region with a higher sedimentation velocity. To maintain the same average visible albedo it was necessary to increase the production rate (4×). To match the albedo near 1 μm the surface albedo had to be increased to 0.2 from its nominal value of 0.1.

The haze still responded sluggishly to the production variations, because a large phase delay continued to exist ($-60°$) and a higher amplitude of production variation with respect to the steady-state calculations was needed ($\gamma = 16$). The continued sluggishness was a result from increasing the column production rate to compensate for the higher rainout boundary.

With the raised rainout boundary and increased production rate the conventional model exhibited a phase delay more consistent with the revised model ($-60°$). This was a result of the reduction of the spatial extent of the haze and a decrease in the ability of haze material near optical depth unity to significantly vary over time, because the residence time of this section of the haze was increased.

Alternative causes. Because of the inability of time variations in the haze production rate to account for the albedo variations, the time variations of other factors which determine the haze structure should be investigated. When attempting to use another factor, it is important to consider the time dependence of the induced geometric albedo variations.

One group of other factors are associated with haze production. Besides the column production rate, this group includes the composition which affects the absorption coefficient of the haze (Sromovsky *et al.* 1989). The seasonal haze compositional variations are difficult to evaluate, because of the inability of photochemical models to simulate haze production. Some work on the problem has attempted to link latitudinal variations of brightness and observed gaseous species which are believed precursors of haze material (Courtin 1991). The implication is that the variations in gaseous species induce haze absorption variations. A negative correlation between the latitudinal variation of the HCN to C_2H_4 ratio on Titan and brightness is shown to exist (i.e., absorption increases with the HCN to C_2H_4 ratio). However, Courtin (1991) points out that the correlation conflicts with an earlier

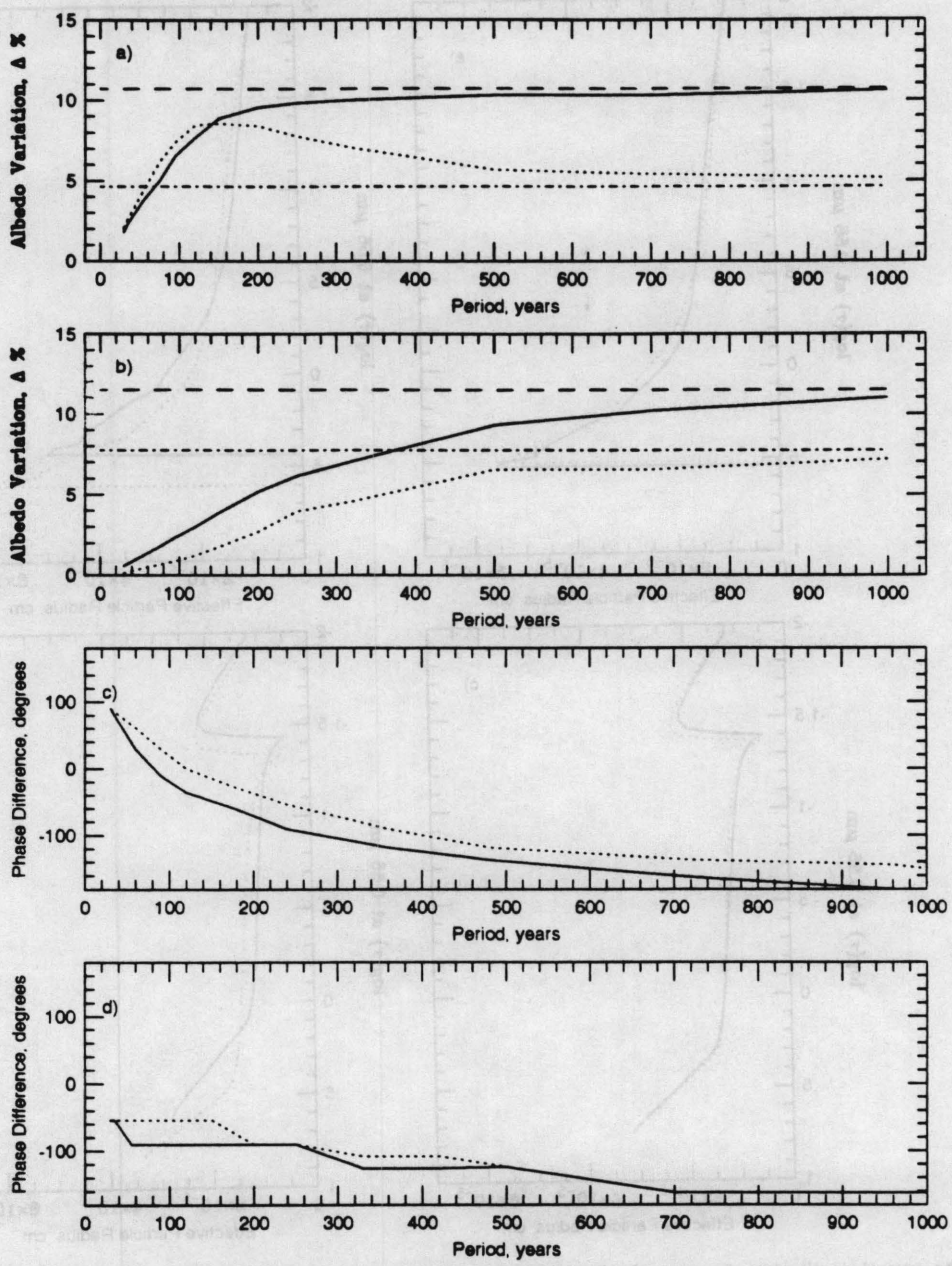

FIG. 6. The maximum to minimum geometric albedo variation (expressed as a percentage difference) for blue (solid line) and yellow (dotted line) plotted against the period of production variation for $\gamma = 2$ of (a) the conventional model and (b) the revised model. For the conventional model, the blue variations steadily converge to the $\gamma = 2$ steady-state prediction (the dashed line), but the yellow albedo variation overshoots the steady-state prediction (the dot–dashed line) and then converges. The phase delay versus production period is shown for (c) the conventional model and (d) the revised model. The step-like appearance of the curves in (d) is a sampling effect.

reported relationship between laboratory haze absorption and its N to C ratio (Scattergood *et al.* 1988). This conflict illustrates the difficulties of determining the seasonal variations of haze absorption.

Another group of factors which are involved in determining the haze structure are atmospheric properties such as circulation. Atmospheric circulation variations affect haze distribution and the optical depth profile through haze transport. Evidence for the role of circulation in producing the hemispheric brightness asymmetry and the geometric albedo variations was the sharp edge of the contrast at the equator (Smith *et al.* 1981). Although

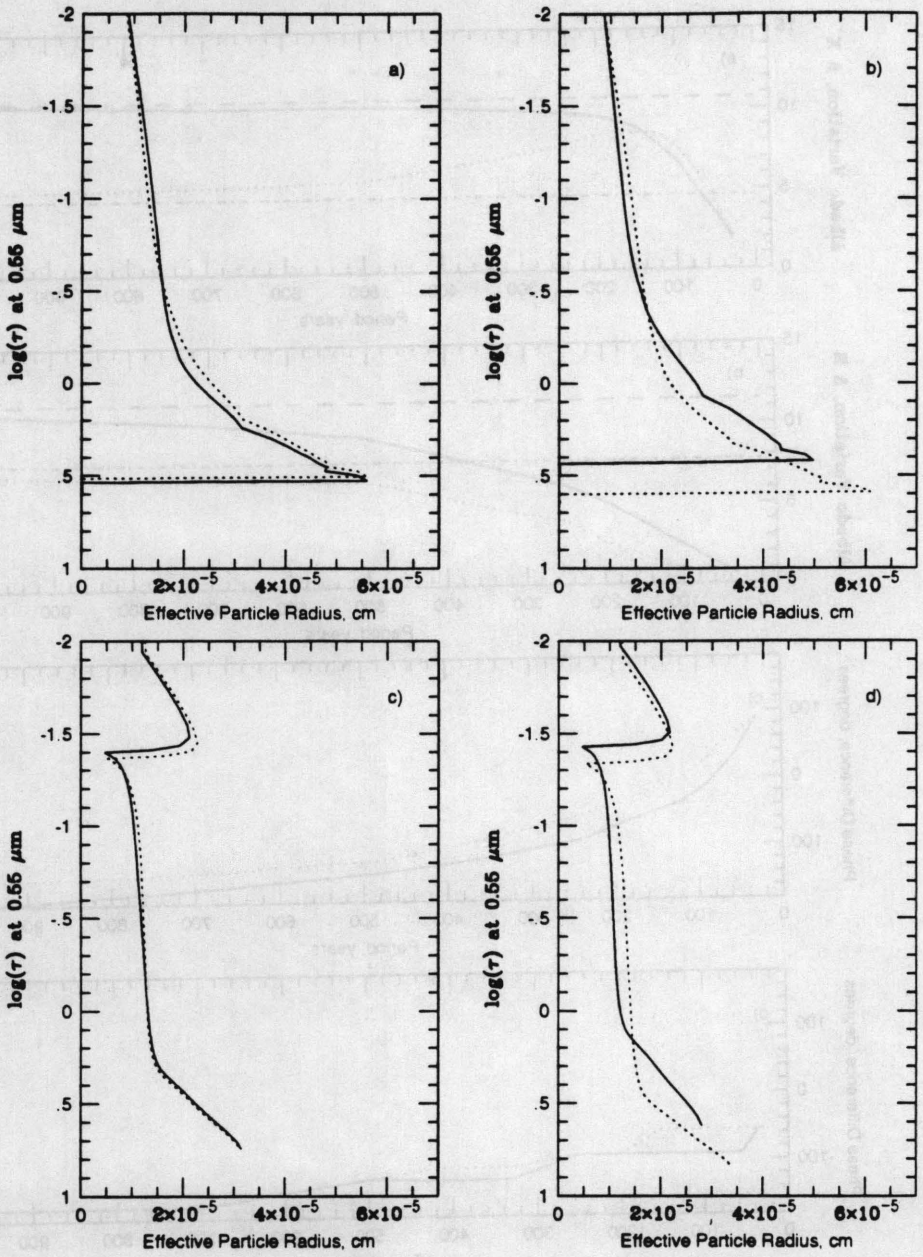

FIG. 7. The optical depth plotted against the haze particle effective radius for (a) the time-dependent conventional, (b) the steady-state conventional, (c) the time-dependent revised models, and (d) the steady-state revised models are shown for the maximum (solid) and minimum (dotted) yellow geometric albedo. In the time-dependent models, the particle size variations near optical depth unity were larger for the conventional model.

detailed modeling of the seasonal haze variations from atmospheric circulation has yet to be accomplished, there has been some work on the potential role of circulation. Flasar and Conrath (1990) suggested that seasonal variations of stratospheric circulation exhibit a phase delay of approximately +90°, if atmospheric properties are determined by a combination of radiative equilibrium and cyclostrophic dynamics. Their argument was based on observations of latitudinal variations of the atmospheric temperature structure (Flasar *et al.* 1981, and Flasar and Conrath 1990). The albedo effects of vertical advection from an upwelling wind were investigated in the revised model by Toon *et al.* (1992). Their results predict a decrease of the visible albedo with upwelling. Interestingly, upwelling in the darker spring hemisphere is consistent with the Voyager observations, and the +90° out of phase

thermally indirect pole to pole cell in Flasar and Conrath (1990).

Time variation of the circulation can also effect the atmospheric thermal structure. Thermal structure variation might affect the haze and geometric albedo by altering haze microphysical processes and haze material composition. The former source of albedo variation is believed to be negligible. The latter is uncertain, because of the difficulties associated with determining haze composition.

Determining factors which control the geometric albedo will have to await more sophisticated modeling, laboratory research, and observations. To determine possible variation of haze composition, the construction of more complicated photochemical models is needed. The new photochemical models should include heavier organic compounds and the temporal variation of solar flux. An alternative method for exploring haze compositional variations is laboratory study. Such research has the potential to reveal aspects of haze composition which may be unattainable by photochemical models (Courtin *et al.* 1991). For evaluating the possible role of circulation, the present one-dimensional modeling is insufficient, because of the difficulties dealing with transport from atmospheric circulation (Toon *et al.* 1992). A two-dimensional haze model with dynamics is part of the solution to these difficulties which we will pursue in future work.

CONCLUSIONS

We have attempted to simulate amplitude and phase of the observed blue and yellow geometric albedo variations of Titan by using the conventional and revised versions of the Titan haze model from Toon *et al.* (1992). We draw the following conclusions from our calculations.

1. Steady-state calculations suggest a variation of the haze production rate between a factor of two and four is enough to cause the observed geometric albedo variations. However, our Titan haze model with a smoothly varying haze production rate produces a much smaller magnitude of albedo variations with the same variation in production rate This reduction in response is because the average haze time scale is much longer than the seasonal periodicity and prevents the required changes in the haze mass column density and particle sizes.

2. Alternate functional forms for the production which invoked discontinuous production changes and larger production rate variations did not improve the fit to observations. Changing model parameters did increase the size of the computed albedo variations, but the correct phase response of the albedo was not simultaneously produced. The increased albedo variation was accomplished by raising the upper rainout boundary, increasing the haze mass column production rate, and increasing the size of the production variations. These changes may be unphysical because they imply that rainout is occurring well into the stratosphere.

3. A consequence of the long haze time scales is a phase lag between the time variation of the albedo and production. The value of the produced phase difference can agree with observations (Sromovsky *et al.* 1981), but it is sensitive to model parameters. The model parameter values that produced the best agreement with the size and spectral dependence of the geometric albedo variations did not yield the correct phase delay. Hence, models which only use variations of mass production rate to explain the albedo variations appear not to work.

Other time-varying factors such as haze composition and atmospheric circulation could be used to explain the observed geometric albedo variations. The difficulty remains to evaluate the time variations of these other factors and what are the induced geometric albedo variations. The determination of a possible $+90°$ phase delay between seasonal forcing and atmospheric circulation variations (Flasar and Conrath 1990) and the possible effect of vertical advection on the visible geometric albedo (Toon *et al.* 1992) are motivations to explore the effects of atmospheric circulation on the haze and the geometric albedo. To accomplish such a study, more sophisticated models of Titan's atmospheric circulation and haze are being constructed.

ACKNOWLEDGMENTS

This work was supported by the NASA Planetary Atmospheres Program. We thank the reviewers for their extensive suggestions which greatly improved and sharpened the focus of this paper. William T. Hutzell was supported by the NASA Graduate Researcher's Program.

REFERENCES

ALLEN, M., J. P. PINTO, AND Y. L. YUNG 1980. Titan: Aerosol photochemistry and variations related to the sunspot cycle. *Astrophys. J.* **242,** L125–L128.

BORUCKI, W. J., Z. LEVIN, R. C. WHITTEN, R. G. KEESEE, L. A. CAPONE, A. L. SUMMERS, O. B. TOON, AND J. DUBACH 1987. Predictions of the electric conductivity and charging of the aerosols in Titan's atmosphere. *Icarus* **72,** 604–622.

CALDWELL, J., C. C. CUNNINGHAM, D. ANTHONY, H. P. WHITE, E. J. GROTH, H. HASAN, K. NOLL, P. H. SMITH, M. G. TOMASKO, AND H. A. WEAVER 1992. Titan: Evidence for seasonal change—a comparison of Hubble Space Telescope and Voyager images. *Icarus* **97,** 1–9.

COURTIN, R. 1991. Titan's UV albedo and modeling. In *Proceedings Symposium on Titan, ESA SP-338,* pp. 59–67. European Space Agency, Toulouse, France.

COURTIN, R. R., R. WAGENER, C. P. MCKAY, J. CADWELL, K. FRICKE, F. RAULIN, AND P. BRUSTON 1991. UV spectroscopy of Titan's atmosphere, planetary organic chemistry, and prebiological synthesis. II. Interpretation of the new IUE observations in the 220–235-nm range. *Icarus* **90,** 43–56.

CUNNINGHAM, C. C., J. J. CADWELL, H. P. WHITE, AND D. M. AN-

THONY 1991. Evidence for seasonal changes on Titan. *Bull. Am. Astron. Soc.* **23,** 1187–1188.

FINK, U., AND H. LARSON 1979. The infrared spectra of Uranus, Neptune, and Titan from 0.8 to 2.5 microns. *Astrophys. J.* **233,** 693–698.

FLASAR, F. M., AND B. J. CONRATH 1990. Titan's stratospheric temperatures: A case for dynamical inertia. *Icarus* **85,** 346–354.

FLASAR, F. M., R. E. SAMUELSON, AND B. J. CONRATH 1981. Titan's atmosphere: Temperature and dynamics. *Nature* **292,** 693–698.

HUBBARD, W. B., *et al.* 1993. The occulation of Sgr 28 by Titan. *Astron. Astrophys.* **269,** 541–563.

HUBBARD, W. B., D. M. HUNTEN, H. J. REITSEMA, N. BROSCH, Y. NEVOA, E. CARREIRA, F. ROSSI, AND L. H. WASSERMAN 1990. Results for Titan's atmosphere from its occulation of 28 Sagittarii. *Nature* **343,** 353–355.

HUTZELL, W. T., W. L. CHAMEIDES, AND C. P. MCKAY 1991. Seasonal Variations in Titan's Stratospheric Haze and Albedo. *Bull. Am. Astron. Soc.* **23,** 1185.

KHARE, B. N., C. SAGAN, E. T. ARAKAWA, F. SUITS, T. A. CALLCOTT, AND M. W. WILLIAMS 1984. Optical constants of organic tholins produced in a simulated Titanian atmosphere: From soft x-ray to microwave frequencies. *Icarus* **60,** 127–137.

LELLOUCH, E. A., A. COUTENIS, F. RAULIN, N. DUBOULE, AND C. FRERE 1989. Titan's atmosphere and hypothesized ocean: A reanalysis of Voyager 1 radio-occultation and IRIS 7.7 micron data. *Icarus* **79,** 328–349.

LOCKWOOD, G. W. 1977. Secular brightness increase of Titan, Uranus, and Neptune, 1972–1976. *Icarus* **32,** 413–430.

LOCKWOOD, G. W., B. L. LUTZ, D. T. THOMPSON, AND E. S. BUS 1986. The albedo of Titan. *Astrophys. J.* **303,** 511–520.

LOCKWOOD, G. W., AND D. T. THOMPSON 1979. A relationship between solar activity and planetary albedos. *Nature* **280,** 43–45.

MCKAY, C. P., J. B. POLLACK, AND R. COURTIN 1989. The thermal structure of Titan's atmosphere. *Icarus* **80,** 23–53.

NEFF, J. S., D. C. HUMM, J. T. BERGSTRALH, A. L. COCHRAN, E. S. BARKER, AND R. G. TULL 1984. Absolute spectrophotometry of Titan, Uranus, and Neptune. *Icarus* **60,** 221–235.

POLLACK, J. B., K. RAGES, O. B. TOON, AND Y. L. YUNG 1980. On the relationship between secular brightness changes of Titan and solar variability. *Geophys. Res. Lett.* **7,** 829–832.

RAGES, K., AND J. B. POLLACK 1983. Titan aerosols: Optical properties and verticle distribution. *Icarus* **55,** 50–62.

SCATTERGOOD, T. W., AND *et al.* 1988. Titan's organic haze over the last four billion years. *Bull. Am. Astron. Soc.* **20,** 842.

SMITH, B. A., L. SODERBLOM, R. BEEBE, J. BOYCE, G. BRIGGS, A. BUNKER, S. A. COLLINS, C. J. HANSEN, T. V. JOHNSON, J. L. MITCHELL, R. J. TERRILE, M. CARR, A. F. C. II, J. CUZZI, J. B. POLLACK, G. E. DANIELSON, A. INGERSOLL, N. E. DAVIES, G. E. HUNT, H. MASURSKY, E. SHOEMAKER, D. MORRISON, T. OWEN, C. SAGAN, J. VEVERKA, R. STROM, AND V. E. SUOMI 1981. Encounter with Saturn: Voyager 1 imaging science results. *Science* **212,** 163–190.

SROMOVSKY, L. A., AND P. M. FRY 1989. The phase variation of Titan's brightness contrast: Implied constraints on the properties of the haze particles. *Bull. Am. Astron. Soc.* **20,** 842.

SROMOVSKY, L. A., V. E. SUOMI, J. B. POLLACK, R. J. KRAUSS, S. S. LIMAYE, T. OWEN, H. E. REVERCOMB, AND C. SAGAN 1981. Implications of Titan's north–south brightness asymmetry. *Nature* **292,** 698–702.

TOON, O. B., C. P. MCKAY, C. A. GRIFFITH, AND R. P. TURCO 1992. A physical model of Titan's aerosol. *Icarus* **95,** 24–53.

TOON, O. B., R. P. TURCO, AND J. B. POLLACK 1980. A physical model of Titan's cloud. *Icarus* **43,** 260–282.

TOON, O. B., R. P. TURCO, D. WESTPHAL, R. MALONE, AND M. S. LIU 1988. A multidimensional model for aerosols: Description of computational analogs. *J. Atmos. Sci.* **45,** 2123–2143.

YUNG, Y. L. 1987. An update of nitrile photochemistry on Titan. *Icarus* **72,** 468–472.

YUNG, Y. L., M. ALLEN, AND J. P. PINTO 1984. Photochemistry of the atmosphere of Titan: Comparison between model and observations. *Astrophys. J. Suppl. Ser.* **55,** 465–506.

APPENDIX II

Variations in the Geometric Albedo of Titan

William T. Hutzell

150 Pages

Directed by Dr. William L. Chameides

At 0.47 μm and 0.55 μm, the geometric albedo of Titan has been observed to vary over the past two decades (Lockwood 1977 and Lockwood *et al.* 1986). Variations in atmospheric reflectance are used to explain these observations, and are postulated to be determined by the haze layer in the atmosphere (Sromovsky *et al.* 1981), because the haze layer has a global extent and is optically thick in the visible (Pollack *et al.* 1980). Therefore, variations in the haze layer are believed to cause the observed variations in the geometric albedo.

Two controls on the haze layer are examined for the source of the observed variations. Each examination consists of two parts: time simulations of the haze layer, and comparisons between the predicted reflectances and the observations. The first part simulates the haze layer by using an aerosol model. The comparison test is accomplished by radiative transfer calculations of the results from haze simulations (Toon *et al.* 1989). Production of the haze layer is one control on the haze layer and is examined with an aerosol model which has been applied to Titan (Toon *et al.* 1992). The circulation of the atmosphere is the second control which produces the haze variations. The control from the circulation is examined by an aerosol model which is two dimensional. A two dimensional model is constructed to accomplish the

second examination, because the existing model is inadequate. A wind field is derived to represent the circulation in the atmosphere and induces variation in the haze layer.

The circulation of the atmosphere is determined to be a better source of the observations of the geometric albedo and the hemispheric brightness for two reasons. The variations in the production rate produced only the size of the observed variations. The variations in the circulation matched the size and the temporal variations of the observations. The circulation source was also considered the better source of the observed variation, because the observations were not reproduced by using model parameters which may be physically implausible.

The conclusion on the source for the observations does have reservations. Problems were indicated, because our simulations of the hemispheric brightness contrast were poor. The representation of the circulation is most likely the cause of this failure. Our representation of the circulation was an extreme simplification of the actual circulation, because derived wind field was one large cell for the entire stratosphere and did not include small scale processes (Flasar *et al.* 1981 and Flasar and Conrath 1990). The wind field for the haze model also derived with several assumptions which are probably not true for Titan.